UNIVERSIDAD DE CANTABRIA

PROGRAMA INTERUNIVERSITARIO DE DOCTORADO EN TECNOLOGÍAS DE LA INFORMACIÓN Y COMUNICACIÓN EN REDES MÓVILES POR LAS UNIVERSIDADES DE A CORUÑA, OVIEDO, CANTABRIA, PAÍS VASCO y ZARAGOZA

TESIS DOCTORAL

ESTRUCTURAS DIMINUTAS INSCRITAS MEDIANTE LÁSERES DE FEMTOSEGUNDO PARA SENSORES ÓPTICOS

AUTOR: DAVID PALLARÉS ALDEITURRIAGA
DIRECTORES: JOSÉ MIGUEL LÓPEZ HIGUERA
LUIS RODRÍGUEZ COBO

ESCUELA DE DOCTORADO DE LA UNIVERSIDAD DE CANTABRIA
SANTANDER 2019

UNIVERSIDAD DE CANTABRIA

PROGRAMA INTERUNIVERSITARIO DE DOCTORADO EN TECNOLOGÍAS DE LA INFORMACIÓN Y COMUNICACIÓN EN REDES MÓVILES POR LAS UNIVERSIDADES DE A CORUÑA, OVIEDO, CANTABRIA, PAÍS VASCO y ZARAGOZA

PH.D. THESIS

TINY STRUCTURES INSCRIBED BY FEMTOSECOND LASERS FOR OPTICAL SENSING

AUTHOR: DAVID PALLARÉS ALDEITURRIAGA
SUPERVISORS: JOSÉ MIGUEL LÓPEZ HIGUERA
LUIS RODRÍGUEZ COBO

SANTANDER 2019

If it bleeds, we can kill it.

— Arnold Schwarzenegger

To all the special people in my life

ACKNOWLEDGEMENTS

The following projects and grants supported the research performed in this PhD:

- Optical Fiber Sensors for Safety and Protection (TEC2013-47264-C2-1-R), Ministerio de Economía y Competitividad.
- Sensores fotónicos para la seguridad y protección (SENSA) (TEC2016-076021-C2-2-R), AEI/FEDER, UE.
- BES-2014-069736, Ministerio de Economía y Competitividad.
- EEBB-I-17-12409, Ministerio de Economía y Competitividad.

From the participation on these projects, authors would like to acknowledge the contributions of the whole Photonics Engineering Group, especially Mauro Lomer and Pablo Varona Roldán. Jesús Mirapeix Serrano, Arturo Pardo Franco, Olga Mª Conde Portilla and Antonio Quintela Incera have also supported this work by thoughtful manuscript revisions or printing and binding management.

This dissertation was improved by the fruitful collaborations with the group led by Prof. Manuel López Amo, particularly Rosa Ana Pérez Herrera performed measurements and montages that supported the results obtained in this work. Besides, authors would like to acknowledge the invaluable contributions that Bertrand Poumellec and Matthieu Lancry from the *Institut de Chimie Moléculaire et des Matériaux d'Orsay* have performed to this work.

RESUMEN

En el presente trabajo, se ha estudiado el potencial de procesado de los láseres de femtosegundo en las fibras ópticas con el fin de desarrollar nuevos sensores ópticos. Para ello, se ha empleado un montaje de inscripción transversal clásico para irradiar la fibra óptica y un sistema híbrido (longitudinal y transversal) para procesar la zona de la punta de la fibra. Además, se han utilizado diversos métodos de caracterización. Esto último es de vital importancia para determinar las propiedades ópticas de las inscripciones producidas, que a su vez son esenciales para el posterior diseño e implementación de estas en estructuras fotónicas tales como sensores de fibra óptica. Por este motivo, se han presentado y analizado cuatro técnicas de caracterización para el estudio de las muestras procesadas. La perfilometría de campo cercano refractado (RNF) para medir precisos perfiles del índice de refracción de las fibras ópticas y cualquier guía inscrita. La microscopía de fase (QPm) que a través de una serie de imágenes de intensidad permite reconstruir una imagen de fase (proporcional al índice de refracción). Esta última técnica junto a la de compensación de Sénarmont (microscopía que permite medir el retardo de un material birrefringente), se han empleado para caracterizar una serie de inscripciones en NdY: SrF2. Estas técnicas han confirmado cambios de índice de refracción a dos tasas de repetición distintas (siendo la repetición baja la que proporciona cambios más suaves y la alta la más adecuada para la inscripción de guías de onda) con un retardo que sugiere birrefringencia inducida por el estrés causado por la expansión permanente del volumen focal. La micro espectroscopía Raman puede medir los cambios estructurales de un material. Como prueba de su utilidad, se ha empleado en el estudio de procesos surgidos en la regeneración de redes de Bragg en fibra (FBGs). Los perfiles de las muestras con/sin regeneración revelan varios indicadores de expansión que sugieren que la estructura precursora al recocerse imprime un cambio en el historial térmico (temperatura ficticia) de la fibra que actúa como red regenerada de Bragg en fibra (rFBG).

Estas técnicas se han empleado en el estudio de la inscripción producida a lo largo de la fibra y en la punta de la misma. En el primer caso, se ha analizado la inscripción de guías de onda en dos configuraciones distintas. La primera configuración consiste simplemente en la inscripción mediante la exposición directa del haz focalizado en la fibra mientras que en el segundo caso, ésta se encuentra sumergida en líquido adaptador de índice, dispuesta entre un portaobjetos y una lámina cubreobjetos para reducir así las aberraciones causadas por la geometría cilíndrica de la fibra. El método de exposición directa produjo estructuras de tipo II con una región de filamentación que presentaba fuertes cambios de índice de refracción positivo. Esta región fue empleada para concebir una nueva configuración de interferómetros de Mach-Zehnder (MZI) que se han empleado como sensores de temperatura, curvatura (mostrando una sensibilidad y rango dinámico significativos para las dimensiones del sensor) y cambio de índice. La segunda configuración, empleando óptica adaptativa, se utilizó para generar redes de difracción, tanto de Bragg, como de periodo aleatorio. Estas últimas se han escrito en diversas fibras estrechadas y se han empleado como espejo selector en un láser de fibra de cavidad lineal. Este láser supone el primer intento de generar láseres de cavidad lineal empleando conjuntamente fibras estrechadas y redes aleatorias. El láser resultante tiene una potencia de salida de 15.4 dBms.

En la punta de la fibra se han escrito varias redes de difracción, estudiando su comportamiento dependiendo del tipo de fibra (monomodo, multimodo, de varios núcleos o de plástico), la zona de inscripción (superficie o en su interior), su inclinación, etc. Algunas de estas configuraciones se han empleado para desarrollar sensores tanto extrínsecos como intrínsecos. Como sensores extrínsecos se ha estudiado el desplazamiento e inclinación, mostrando resultados inmunes a la fluctuación de potencia. Para sensores intrínsecos, se ha caracterizado la temperatura y curvatura de la fibra. Este último parámetro ha sido medido gracias al patrón interferométrico de las fibras de múltiples núcleos, mejorado gracias a la inscripción de la red de difracción. Estos sensores proponen unas bases para consolidar estructuras transductoras más complejas.

Resumiendo, durante la tesis se han estudiado las propiedades de las interacciones de haces láser de femtosegundo en diversos tipos de fibras ópticas para posteriormente, inscribir estructuras ópticas (tanto en la superficie como en su interior) de un interés para el desarrollo de nuevas estructuras transductoras. Con ellas, se han demostrado sensores intrínsecos basados en interferómetros Mach-Zhender así como basados en estructuras grabadas en la superficie de las fibras (sobretodo em un extremo de las mismas).

Futuras líneas de investigación deberían girar en torno a la inscripción de guías de onda y FBG de mayor calidad e inscripciones en punta más complejas, como por ejemplo vórtices ópticos y hologramas binarios.

Este trabajo ha sido validado por la comunidad científica internacional con la publicación de 4 artículos en revistas internacionales de primer cuartil, 6 comunicaciones a congresos internacionales y 3 nacionales reconocidos todos ellos en las actas o proceedings de los mismos que cuentan todos con ISSN y/o ISBN. Además, se encuentran en revisión dos artículos de revista y varios en preparación para su remisión.

ABSTRACT

In this work, the processing potential of Femtosecond (fs) lasers in optical fibers have been studied, focusing on in-fiber and end-fiber inscription. In the first scenario, attention has been drawn towards waveguide inscription in two different configurations. The first one involves direct exposition of the focused pulse while the other involves adaptive optics. This later configuration consisted in sandwiching the optical fiber between a microscope slide and a coverslip to reduce aberrations caused by the cylindrical geometry of the fiber. The direct exposition configuration produced a type II structure with a filament region with high positive Refractive Index Change (RIC). This region was used to manufacture a Mach-Zehnder Interferometer (MZI) that has been used as a temperature, bending and Refractive Index (RI)sensor. The adaptive optics configuration was employed for grating inscription, manufacturing Fiber Bragg Gratings (FBGs), and Random Fiber Gratings (RFGs). These later were inscribed in Tapered Optical Fibers (TOFs) and used as a mirror in a single cavity laser.

Several diffraction gratings were inscribed at the fiber end face. Attention was drawn towards their inscription at different types of optical fiber (Single Mode Fibers (SMFs), Multi Mode Fibers (MMFs), Multicore Fibers (MCFs) and Polymer Optical Fibers (POFs)), zones (surface, bellow surface) tilts and dimensions. Some of the studied configurations were applied for both extrinsic and intrinsic sensing. Displacement and tilt sensing were demonstrated with immunity to power fluctuations. Temperature and bending were also demonstrated. The bending sensitivity was achieved thanks to a MCF interferometric Far Field Pattern (FFP) enhanced by the inscribed diffractive element.

The present structures were modeled and characterized by several tools whose relevance in fs processing is discussed.

CONTENTS

ACRONYMS

BPM Beam Propagation Method

CMT Coupled Mode Theory

CPA Chirped Pulse Amplification

CVD Chemical Vapor Deposition

CW Continuous Wave

EDF Erbium Doped Fiber

EDM Electrical Discharge Machining

FBG Fiber Bragg Grating

FDTD Finite Difference Time Domain

FEG-SEM Field-Emission Gun Scanning Electron Microscope

FFP Far Field Pattern

FIB Focused Ion Beam

FLCPA Fiber Laser Chriped Pulse Amplifier

FPI Fabry-Perot Interferometer

fs Femtosecond

FSR Free Spectral Range

FTL Faster Than Light

IR Infrared

KET Key Enabling Technology

KKr Kramers-Konig relations

LAVD Laser Assisted Vapor Deposition

LIRIC Laser Induced Refractive Index Change

MCF Multicore Fiber

MI Michelson Interferometer

MMF Multi Mode Fiber

MPA Multiphoton Absorption

MZI Mach-Zehnder Interferometer

NBOHC nonbridging oxygen hole center

NA Numerical Aperture

OA Optical Axis

OFS Optical Fiber Sensor

OPA Optical Parametric Amplification

OPD Optical Path Difference

OSA Optical Spectrum Analyzer

PbP Point-by-Point

PLD Pulsed Laser Deposition

POF Polymer Optical Fiber

PRR Pulse Repetition Rate

QPm Quantitative Phase microscopy

RE Rare Earth

rFBG regenerated Fiber Bragg Grating

RFG Random Fiber Grating

RI Refractive Index

RIC Refractive Index Change

RNF Refracted Near Field

SFDI Spatial Frequency Domain Imaging

SHG Second Harmonic Generation

SI Sagnac Interferometer

SMF Single Mode Fiber

STE Self-Traped Exciton

TOF Tapered Optical Fiber

WD Working Distance

ws writing speed

UV Ultraviolet

Part I

PRELIMINARY

1

INTRODUCTION

The experimental demonstration of the laser (1960) was the success that enabled the conception of the new field of knowledge known as Photonics. It is one of the six Key Enabling Technologys (KETs) that the European Union Commission regards as essential to its sustained economic growth. It is also highly valued in the European Commission's programme Horizon 2020 being implicitly or explicitly featured in the work programme of each of the programme's priorities. Several of their topics have been identified as clear opportunities by independent institutions [1]. Its potential stems from its broad versatility that allows its application in different sectors such as biomedicine, industry, metrology, telecom, and sensing [2, 3].

In the bio sector, photonics has proven to be an indispensable technology for its development and continuous modernization. The advances achieved in surgery [4, 5, 6] detection [7, 8] and even manipulation [9] revolutionized the entire field. In the conventional industry, their contributions not only consisted of the improvement of the current drilling, welding and cutting techniques [10] but also introduced new forms of noninvasive structural study [11].

The application of photonics to metrology caused a revolution in high precision non-contact measurements. Several significant improvements in metrology stem from optical interferometry [12], allowing reliable profilometers and distance or velocity sensors.

The field of telecom is one of the most enriched by this technology. The optical communications exhibit enormous bandwidth[1], good isolation, immunity to interference, crosstalk, and exhibit really low transmission loss. This is thanks to the development of optical fibers that allow light to be guided and act as a very low loss transmission media [13].

The state of the art of sensing techniques is highly influenced by optical devices. Various optical effects can be exploited to measure several parameters [2]. Pockel's effect can be employed to measure alternate current voltage [14], Faraday's effect can also be used for magnetic field sensing [15], acusto-optic effect can be used for turbulent media measurement [16]. Interference effect is not limited to metrology; it can sense any parameter that can produce a phase change[2] and diffraction effect can also measure several changes such as temperature, strain, RI,...

All of these effects are relatively easy to produce; this led to Elias Snitzer to study the behavior of an optical fiber as a cavity equivalent to a Fabry-Perot Interferometer (FPI) [17]. After that, the optical fiber was no longer regarded as a simple pipe of light but also as a reliable transducer. This potential led to the development of Optical Fiber Sensors (OFSs). There are several ways that an optical fiber can act as a sensor, several of them will be

1 The optical carrier frequency for Infrared (IR) is around 10^5 GHz which is an outstanding improvement respect to metallic cable systems with a bandwidth around 500MHz [13].

2 Which is a considerable number.

reviewed (and developed) in the later chapter. The current trend looks for more compact sensitive and multi-sensing devices[3]. For that reason, there is an increased effort in the development of new OFSs designs.

As mentioned, the key device that photonics has offered in the later century is, of course, the laser. Among the massive amount of applications the laser technology can provide, material processing supposes a massive step in the micro and nano world where other conventional methods are just outdated. The ultrafast pulsed lasers or Femtosecond (fs) lasers exhibit superior properties for laser micromachining and microprocessing compared with other devices. This superiority makes them very interesting for processing applications where microscale resolution is required. This is the case of OFS where transducer structures can be inscribed in regions of $\approx 100\mu m$ [19].

There are several works addressing fs laser inscription in optical fibers, becoming a very active research field. These studies revealed the potential of these lasers for manufacturing OFSs shorter than 1mm [20]. An example of mature technology enhanced by fs lasers are the fs inscribed FBGs that exhibit higher intensity than conventional Ultraviolet (UV) FBG. However, there are still several challenges that must be faced.

Particularly, optical sensors usually employ optical structures that decouple/couple modes and change their propagation direction. However, there is little work employing fs laser inscribed waveguides in the optical fiber. Waveguides are a critical step towards complex OFS with several sensing elements in the same region [21]. Thus, new ways of fiber inscription and implementation should be studied. Thus, the inscription of waveguides (with optimized optical properties) inside optical fibers are of paramount importance to conceive and develop new advanced and microscaled sensing structures [22].

Interferometric, grating and other advanced laser inscribed structures will be considered in this work to generate new knowledge and technique able to contribute to state of the art.

Finally, the FFP of an optical fiber addresses several data about the fiber end-face properties. The inscription of patterns at the end-face can highlight some internal parameters of the fiber or the screen surface. The most straightforward pattern that can be inscribed into a fiber end-face is a diffraction grating. Works addressing diffraction gratings at the fiber end-face surface usually employ thin film layer, which increases its manufacturing cost and complexity [23]. In contrast, fs lasers can inscribe diffraction gratings with good control and tunability, inscribing chirp, apodization or more complex structures. However, the amount of manufactured diffraction grating based sensors inscribed with fs lasers is quite modest.

The present doctoral dissertation tries to contribute to the photonic sub areas mentioned above. These contributions will produce a solid background for new developments in the field of Optical Fiber Sensors (OFSs).

The dissertation will be divided into the following sections:

CHAPTER 2 will introduce several basic aspects of optical material processing with emphasis on the fs laser processing of optical fiber and a quick state of the art of OFSs. The chapter is thought to contain all the relevant theory of the following chapters.

CHAPTER 3 will state the main goals of this PhD given the current state of the art.

3 Examples of this need are the lab-on-chips systems designed for several functionalities implementation in a single substrate for the measurement of small biological samples [18].

CHAPTER 4 will review the setup, tools and techniques employed in the following chapters. The most relevant techniques will be applied in actual cases to show their performance and utility.

CHAPTER 5 will focus on the transversal inscription in the fiber. Here, two inscription ways will be studied and employed in manufacturing OFSs and other elements.

CHAPTER 6 will focus on the fiber end-face inscription. Diffraction gratings will be studied and employed in several scenarios. This characterization will lead to the design of several FFP based OFSs.

CHAPTER 7 will briefly summarize all the work performed and all the relevant results highlighted.

CHAPTER 8 will propose future lines for the continuation of the work performed in the dissertation.

2

PROCESSING OF OPTICAL MATERIALS

Material processing covers the series of operations that transforms industrial materials from a raw-material state into finished parts or products. It accounts for a wide amount of processes that may be distinguished mainly between forming the material into the desired shape and altering the material's properties (due to changes in the microscopic structure of the material). A clear example of the first group is machining, which encloses any process in which material is removed gradually from a workpiece [24]. This can be performed by cutting, abrasive or another *non traditional process*. This late group covers the *recently* emerged techniques such as Chemical machining, Electrical-discharge machining, Laser-beam machining, etc... Examples of altering material's properties processes are the thermal treatment or vapor deposition.

Post-processing accounts for any operation performed to an already processed product in order to change or enhance its functionality. As in any other industry field, processing of optical materials is vital not only to sustain and improve its own field but also to positively impact various economic sectors thanks to technology diversification. This makes improvement of processing techniques essential to the impact and development in optics and photonics related technology.

This chapter aims to introduce to the fs laser processing of optical fiber. This topic could easily fill several books like [18], being each of the elements subjects of extensive study and research. Thus, this introduction will review each of their parts, namely; Dielectric materials (and optical fiber), processing of materials and fs lasers, separately. The purpose is not an in-depth revision of the topics and state of the art but a review of the key concepts required to understand the big picture. These concepts will be applied in the later chapters to produce scientific work.

The chapter will be divided as follows:

SECTION 2.1 Will briefly review the properties of optical materials and how they can be modified by laser processing in comparison with other techniques.

SECTION2.2 Will address different ways in which Refractive Index (RI) can be modified.

SECTION 2.3 Will review the state of the art of the fs laser from a historical and physical perspective. The modifications performed to dielectric materials will be highlighted.

SECTION2.4 Focuses on the processing of optical fibers and how they can be turned into a sensor.

SECTION2.5 Will close the chapter putting all the pieces together.

2.1 MATERIALS AND TECHNIQUES

Optical materials are the core and principal components of photonic devices and optical setups. Light can be efficiently guided and modified by them allowing precise control of several optical phenomena that may be employed in communications, sensors, radiation, research, etc...

In this section, both optical materials and laser processing techniques will be briefly introduced. The material review will be focused mainly on the intrinsic optical properties that make them suitable for optical manipulation. Other processing techniques will be also introduced as a reference.

2.1.1 OPTICAL PROPERTIES

2.1.1.1 *Refractive Index*

Refractive Index (RI) is one of the most important parameters that can define a material from an optical perspective. In its simplest definition, it is the rate of light velocity in the material and the vacuum. As light is an electromagnetic wave and hence, governed by Maxwell's laws, its velocity can be related to the medium permittivity ϵ and permeability μ by $v = (\mu\epsilon)^{-1/2}$. RI can be therefore expressed in the so-called Maxwell relation

$$n = \frac{c}{v} = \sqrt{\frac{\epsilon\mu}{\epsilon_0\mu_0}} \sim \sqrt{\epsilon_r}, \tag{1}$$

here, $\epsilon_r = \frac{\epsilon}{\epsilon_0}$ is the dielectric constant, permeability has been neglected as μ is very close to μ_0 for most materials. From this definition, it is clear that light will propagate at a different speed, having an influence on the phase of electromagnetic waves. Two light rays with the same initial phase traveling equal distances in different RI will exhibit phase difference. This is crucial for interference theory. However, the effect of a material RI over light properties is not limited to phase. When light reaches the intersection of two media with different n, it will split into a transmitted wave propagating with a different direction in the second medium and a reflected wave propagating the incidence medium. Both transmitted wave directions and coupling rate between the incident wave and reflected/transmitted wave will depend on RI following Snell's law and Fresnel's equations:

$$\sin\phi = n\sin\phi'' \quad (2)$$

$$t_{\parallel} = \frac{2\cos\phi}{n\cos\phi + \cos\phi''} \quad (3) \qquad r_{\parallel} = \frac{n\cos\phi - \cos\phi''}{n\cos\phi + \cos\phi''} \quad (5)$$

$$t_{\perp} = \frac{2\cos\phi}{\cos\phi + n\cos\phi''} \quad (4) \qquad r_{\perp} = -\frac{n\cos\phi'' - \cos\phi}{\cos\phi + n\cos\phi''} \quad (6)$$

In Eqs. 2-6, ϕ, ϕ'' are the incident and refracted angle respectively. $r_{\perp}$, $r_{\parallel}$, $t_{\perp}$ and $t_{\parallel}$ are the perpendicular and parallel reflection and transmission amplitude coefficients, finally, n is the quotient of RI of refracted medium over incident ($n = n_2/n_1$). These formulas are a direct result of electromagnetic boundary conditions. Materials with proper RI can change light phase, split beams with desired coupling ratio and deviate beam trajectory. All of this has been assumed for $\epsilon_r = cte$ which is true for homogeneous and isotropic media. Permittivity can change depending on the position, direction and even the frequency of electric field that is irradiating the media

$$\epsilon(r,\omega) = \begin{pmatrix} \epsilon_{x'x'}(r,\omega) & \epsilon_{x'y'}(r,\omega) & \epsilon_{x'z'}(r,\omega) \\ \epsilon_{y'x'}(r,\omega) & \epsilon_{y'y'}(r,\omega) & \epsilon_{y'z'}(r,\omega) \\ \epsilon_{z'x'}(r,\omega) & \epsilon_{z'y'}(r,\omega) & \epsilon_{z'z'}(r,\omega) \end{pmatrix}. \tag{7}$$

In non-magnetic and transparent materials, this tensor is symmetric ($\epsilon_{ij} = \epsilon_{ji}$), and thus can be diagonalized choosing an appropriate reference system (x,y,z) called *principal axes*

$$\epsilon(r,\omega) = \begin{pmatrix} \epsilon_{x(r)}(r,\omega) & 0 & 0 \\ 0 & \epsilon_{y(r)}(r,\omega) & 0 \\ 0 & 0 & \epsilon_{z(r)}(r,\omega) \end{pmatrix}, \tag{8}$$

where ϵ_x ϵ_y and ϵ_z are the principal dielectric constants. Optical materials may be classified in the following groups depending on these values:

GROUP I: ISOTROPIC When $\epsilon_x = \epsilon_y = \epsilon_z$ materials are called isotropic and permittivity is not influenced by direction, materials with cubic lattices are usually found in this group.

GROUP II: UNIAXIAL There is only anisotropy in a principal axis called Optical Axis (OA), usually depicted as ϵ_e while the other two axes share the same value ϵ_o (o and e account for ordinary and extraordinary[1]). When $\epsilon_o < \epsilon_e$, media is said to be positive uniaxial, being the opposite case negative uniaxial. This group encloses trigonal, tetragonal and hexagonal systems.

GROUP III: BIAXIAL There is no equivalent crystallographic directions $\epsilon_x \neq \epsilon_y \neq \epsilon_z$. Common biaxial structures are orthorhombic, monoclinic and triclinic lattices.

The anisotropy in the electric permitivity produces a change in electric field **E** compared to displacement **D** being no longer parallel. From Maxwell's equations it is deduced that this mismatch between **E** and **D** produces also a difference between energy and phase propagation[2]. Assuming plane waves and employing Maxwell's equations the relation between phase propagation direction $\hat{k}$, **D** and **E** is

$$\mathbf{D} = \frac{1}{\mu_0 v^2}\left[\mathbf{E} - \hat{k}(\hat{k}\cdot\mathbf{E})\right]. \tag{9}$$

This relation is depicted in Fig. 1.a. From this equation, the phase velocity v can be deduced establishing the condition $\mathbf{D}\cdot\hat{k} = 0$:

$$\sum_i \frac{k_i^2}{v_i^2 - v^2} = 0, \tag{10}$$

where $v_i = \dfrac{c}{\sqrt{\epsilon_i}}$ and i=x,y,z are the principal axes. Eq. 10 has two solutions that corresponds to two monocromatic plane waves with phase velocity v_1 and v_2 and orthogonal linear polarizations. Let's assume an uniaxial media with $\epsilon_o = \epsilon_x = \epsilon_y \neq \epsilon_z = \epsilon_e$ and an incident plane wave. The plane containing propagation direction and Optical Axis is called principal plane. The electric field can be decomposed in components perpendicular

1 This notation was first used in 1669 by Erasmus Bartholinus while studying the optical properties of calcite.
2 Having also different velocities.

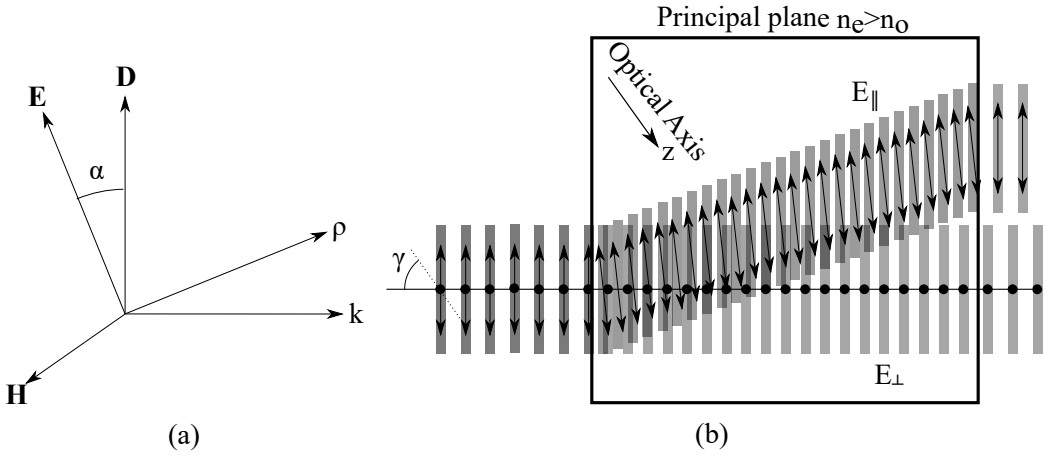

Figure 1: Relation between the electric field **E**, the displacement vector **D** the auxiliary field **H**, the phase propagation direction $\hat{k}$ and energy propagation direction $\hat{\rho}$ (a). A plane wave with both electric field parallel $E_\parallel$ and perpendicular $E_\perp$ to the principal plane of a negative uniaxial material. In the material, the perpendicular field remains unaffected traveling at n_o. However, the wavefront of the parallel field will propagate at different velocities depending on direction, exhibiting a lateral displacement while propagating through the material (b).

($E_\perp$) and parallel ($E_\parallel$) to principal plane. Fig. 1.b depicts the OA, the principal plane and the incident plane wave. From Eq. 10 it is deduced that

$$\begin{aligned}(v_o^2 &- v^2)\left[(k_x^2+k_y^2)(v_e^2-v^2)+k_z^2(v_o^2-v^2)\right]=0\\ v_1 &= \pm v_o \qquad (11)\\ v_2 &= \pm\sqrt{v_o^2\cos^2\gamma+v_e^2\sin^2\gamma}. \qquad (12)\end{aligned}$$

The perpendicular component $E_\perp$ will propagate at velocity v_o, thus, a RI n_o. In contrast, the parallel component will propagate at a velocity v_2 and hence, n_2 that depends on the angle between OA and $\hat{k}$, γ. Uniaxial crystals split the incident light in two waves with different RIs. When a plane wave perpendicularly crosses the material (with thickness L), parallel and perpendicular components will exhibit a phase difference $\Delta\phi$ at the exit of the material

$$\Delta\phi = \frac{2\pi L}{\lambda}(n_0 - \frac{1}{\sqrt{n_o^{-2}\cos^2\gamma+n_e^{-2}\sin^2\gamma}}). \qquad (13)$$

If the propagation direction is perpendicular to OA, retardation $\Delta\phi = 0$ and both components will propagate with n_o. When light propagates perpendicular to OA, then $n_2 = n_e$ and the retardation will achieve a maximum value for the given material length L.

This phenomenon is called birefringence and draws considerable attention for its capability to modify the polarization state of an incident wave. Birefringence is measured by

$$\Delta n = n_0 - n_e, \qquad (14)$$

that accounts for the maximum difference in the RI of the material. Another interesting parameter is the retardation or retardance Γ,

$$\Gamma = L(n_o - n_e). \tag{15}$$

Which is the maximum lagging distance after both rays have exited the crystal. Retardance measures the maximum Optical Path Difference (OPD) that sample can produce, being an essential parameter for sample characterization.

2.1.1.2 *Absorption*

In most cases, only the real part of RI is taken into account as its imaginary counterpart usually is negligible. RI can be represented as $n = n + i\kappa$. κ is also called the extinction coefficient and its effect in a plane wave will be

$$E = E_o e^{i(k_0(n+i\kappa)\hat{k}\vec{r}-\omega t)} = E_0 e^{i(k_0 i\kappa\hat{k}\vec{r})} e^{i(k_0 n\kappa r-\omega t)} = E_0 e^{-k_0\kappa\hat{k}\vec{r}} e^{i(k_0 n\hat{k}\vec{r}-\omega t)} \tag{16}$$

$$I \propto |E_0 e^{-k_0\kappa\hat{k}\vec{r}}|^2 \Rightarrow I = I_0 e^{-2k_0\kappa\hat{k}\vec{r}} = I_0 e^{-\alpha\hat{k}\vec{r}} \tag{17}$$

where α means the absorption coefficient. When this value is high, light propagating in the media will be exponentially attenuated as it propagates (Fig. 2.a). When light is intended to propagate along an optical material, high absorption is not desired. However, there are several cases where light filtering is desired. Several coatings are designed to exhibit high absorption at particular wavelengths.

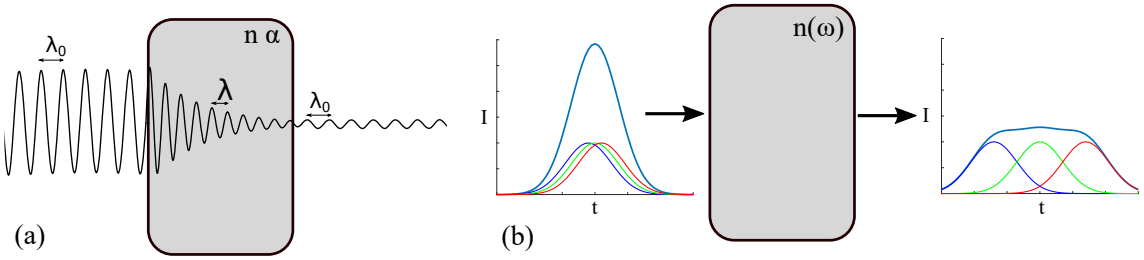

Figure 2: Absorption through a material (a), chromatic dispersion (b).

2.1.1.3 *Dispersion*

As mentioned above, RI changes with frequency and it is responsible for dispersion effects. The most characteristic example of light dispersion is a prism illuminated with white light. Due to Snell's law, the light will be refracted with a different angle as a function of its wavelength, generating a chromatic dispersion (Fig. 3.a). Dispersion effect can also be manifested when a pulse light propagates through a dispersive material. Its temporal pulse width will increase as light at the extremes of spectral broadband will travel at different speeds (Fig. 2.b). In addition, it generates different values from phase velocity and group velocity.

2.1.1.4 *Geometry*

Finally, from Eqs. 2-6, it is clear that incidence angle mostly determines the interaction of light with an optical material. This value can be controlled in several ways, but one of the most important is the shape of the optical material. This is not an intrinsic property of raw optical materials but its role in several optic devices can be decisive. Four obvious

examples of the potential exhibited by selected geometries are prisms, lenses, diffraction gratings and waveguides. Prisms can change the trajectory of light, lenses can converge and diverge light rays, being indispensable for beam shaping and microscopy; diffraction gratings split incident light into a set of diffraction orders whose direction angle depends on the period; finally, waveguides can guide light through its core being the building block of optical communications.

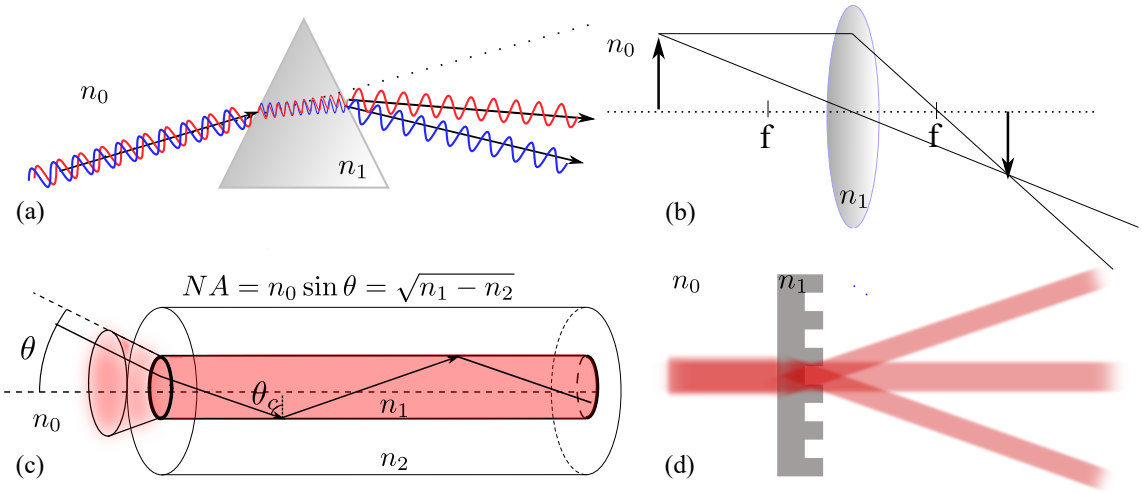

Figure 3: Examples of geometry exploit: prisms(a), lenses (b), waveguides(c) and diffraction gratings (d).

The working principle of waveguides is based on total reflexion. There is a slab media with n_1 (core) surrounded by a media n_2 (cladding) with $n_1 > n_2$, as depicted in Fig. 3(c). Propagating light rays with incident angles to $n_1 - n_2$ intersection higher than the critical angle will suffer internal reflexion being forced to propagate along the n_1 cavity. Waveguides are of special interest for the thesis outline as its manufacture process is different from prisms and lenses. In order to produce one of the aforementioned products, only a shape-shifting process is required to manufacture the instrument [3]. On the contrary, optical waveguides require rather core/cladding sealing process or some kind of processing to modify RI of core or cladding as well. For example, for optical fibers which are the most common type of waveguide, the core n_1 value is achieved by doping the silica material and the cylindrical shape is achieved by a drawing process.

2.1.1.5 *Summary*

The most fundamental properties of optical materials have been quickly reviewed, namely RI, absorption, dispersion, and geometry. Absorption and dispersion are direct consequences of RI complex and frequency dependent nature but its effect is sufficiently notorious to be considered separately. The geometry is another key parameter that determines the optical behavior of the element. Thus, the processing of optical materials, not only for shape-shifting but also for RI modification, is indispensable for several optical devices manufacture. In the following section, the potential of the laser as a material processing tool will be highlighted.

3 At least from a theoretical point of view, several treatments are applied to the glass such as coating deposition in order to enhance its functionality.

2.1.2 LASER PROCESSING

LASER is the acronym of Light Amplification by the Stimulated Emission of Radiation, referring to its underlying principle of function. It is an amplifying light source that generates highly coherent and monochromatic light with small divergence[4]. There were invented around 1958-1957 independently by Bell's laboratory and the University of Columbia[5]. Its appearance unleashed several patents and upgrades up today. This is caused by its intrinsic properties and its potential to achieve high intensities that quickly draw the attention of the industry. Few years after its invention, many proof concepts came up and applied its results to prototypes and research[6]. These first reports and proposed applications were laser drilling, welding[7] and heat treating[8] followed by beam cutting in 1967 [28]. In the 70s, thanks to a decade of laser technology development and the spread of laser applications, led to a boom in laser industrialization. Last decade applications were implemented into the industry and product line. The first automobile containing laser-cut parts was launched in 1975, laser hardening was applied by first time on the industry at 1974. New applications were developed such as pulsed laser cleaning[9] and laser cladding[10] [29]. The decade of 1980 was marked by the search of new methods of using the laser for modern processing rather than direct replacing for conventional processes. Laser began its use on tissue, giving birth to several laser surgery processes such as LASIK[11]. Integrated optics allowed more compact and functional laser device drastically reducing its cost and spreading into industry up to entirely replacing processing tools with its laser counterpart in some plants. The economic recession experimented back in the 90s slowed down the growth experimented in previous decades. However, at this point, laser processing was completely established in the industry and considered another means of manufacture. First femtosecond laser micromachinings date between the late 80s and mid-90s [30, 31, 32]. With the new millennium, lasers were consolidated in the nanotechnology field thanks to its capability to generate nanoscale structures. However, in the world of large-scale material processing, cutting and wielding still dominate. An example of microscale laser inscription is found in the Blu-rays whose pit spacing is $\approx 0.5\mu m$.

In overall, laser processing can be classified as shown in Fig. 4. Lasers can be used to machine materials through a thermal or non-thermal process. In the first case, the laser heats the material up to fusion and then the melted material is removed through a gas jet. Non-thermal machining relies on photoablation or plasma-induced ablation, there is no appreciable melt phase and barely damages the underlying material. Plasma formation

4 Its divergence is usually $\approx 10^{-3}$ rads.

5 Its patent was resolved through 20 years of dispute. Arthur L. Schawlow and Charles H. Townes from Bell's lab first claimed the patent in 1958 [25]. However, Ph.D. student Gordon Gould from the University of Columbia already had theoretically developed laser theory at 1957 but did not patent as he wanted to manufacture a prototype first. The first experimental demonstration was performed by Theodore Maiman in 1960 with a pulsed ruby laser.

6 For example, around 1963, Ruby-laser welding was used to fabricate first Apollo lunar sample return containers [26].

7 Whose first commercial application in the USA was in 1965 introduced by western electric [26].

8 Interaction between laser ruby radiation and graphite coated metal surface showed remarkable results for laser metal hardening research [27].

9 Taking advantage of the absorption difference between substrate and debris.

10 Applying metal coatings by fusing metal rods or wires through the action of a laser beam.

11 This stems from the 1983 proposal of a pulsed excimer laser to ablate regions of corneal epithelium to correct vision defects [4].

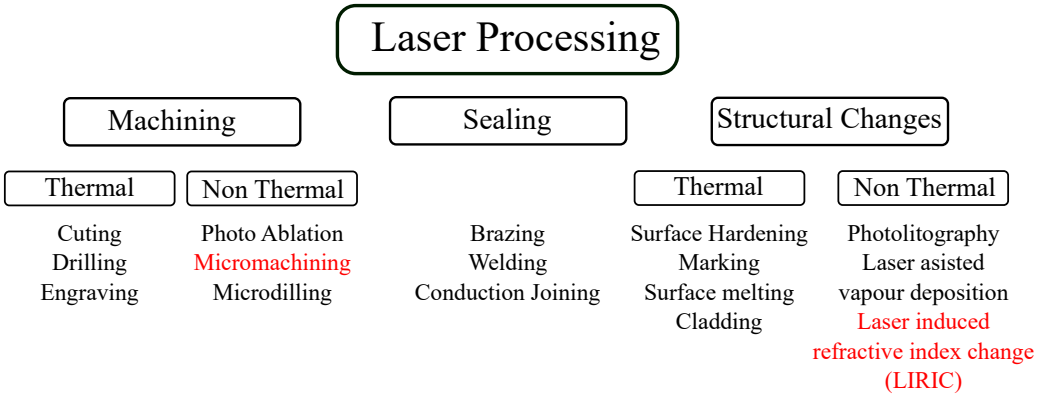

Figure 4: Schematic of laser processing techniques.

requires really high power densities that are achieved through tightly focused ultrashort pulses, which make them adequate for micromachining.

Another extremely wide branch of applications is those that produce a structural change in raw material. Again, one can split these processes in thermal and nonthermal. Thermal processes employ thermal treatment such as annealing to increase its performance as in surface hardening and surface melting processes. Other processes, such as Laser Assisted Vapor Deposition (LAVD) or Laser Induced Refractive Index Change (LIRIC) that improve material properties through laser-assisted chemical or physical changes. There are other applications that can be performed through thermal and nonthermal processes. Laser Marking is a good example of that flexibility, as marking can be performed through bleaching which involves a photochemical reaction or discoloration which is a type of thermal degradation. Finally, sealing techniques hold an important spot in laser processing as keyhole welding is widely spread in industry. These techniques are mainly thermal.

The micromachining and LIRIC (red colored techniques) have several applications in the integrated photonics industry. The micromachining can modify the surface of an optical material, creating complex structures such as microlenses [33] and also producing cavities within the optical material which is an effective way to produce interference [34]. LIRICs by the other hand can be used for optical device inscription in the own optical material [35, 36]. These processes exhibit an outstanding potential for compacting optical designs and will be further studied in sections below and compared to other processing techniques.

2.1.3 OTHER PROCESSING METHODS

There are alternative ways to material process without requiring a laser source depending on the process. This was obvious for several machining and welding techniques until laser replaced already established methods. In terms of LIRICs, the amount of alternatives stretches to annealing [37] and Chemical Vapor Deposition (CVD) [38, 39][12]. CVD are a set o different techniques where a chemical reaction in the vapor phase is deposited on a heated surface. [39]. Examples CVD techniques are modified vapour axial deposition, plasma-activated vapor deposition, direct liquid injected chemical vapor deposition...

12 As mentioned in 2.1.1.4, this method is employed to obtain core/cladding RIC through dopant formation[40, 41, 42, 13] which include TiO_2, GeO_2, P_2O_5, Al_2O_3, B_2O_3 [13].

These techniques can generate thick substrate[13] not restricted to the line of sight, which is useful for complex pieces with difficult 3D geometries whose coating would be challenging otherwise. However, this later advantages can become disadvantages in some scenarios, as techniques were thought for film deposition and are unable to modify bulk material[14] and all the exposed material surface will be equally affected. LIRICs, on the contrary, produces a structural change only in focal volume[15] allowing spatial control of RIC at both surface and bulk.

Micromachining can also be performed by traditional microscale tools [43], Electrical Discharge Machining (EDM) [44] and Focused Ion Beam (FIB) [45]. This later technique consists in the production of high energy ionized atoms of a relatively massive element[16] to be focused into a sample with the purpose of etching/milling or imaging said surface. The ions' large mass allows them to remove surface atoms (milling) and produce secondary electrons which allow the imaging of the sample before, during, and after processing.

The use of massive elements solves one of the major problems in microscopy, the diffraction limit. The spot focused by a circular lens is diffracted creating an airy disc pattern with diameter $d = 1.22\lambda N$ being N the f-number. Otherwise, ions exhibit de Broglie wavelengths[17] several magnitude orders lower than photons and hence they are able to perform mechanization with higher precision than laser mechanization. It can engrave complex patterns in the nanoscale. Its main disadvantage is the effective cost of these systems.

2.1.4 SUMMARY

This section addressed the basic aspects of optical materials performing a quick review of their properties. For that reason a quick glance of physical properties of refractive index, such as birefringence, absorption and dispersion have been performed. Besides, the role of geometry in the behavior of the material has been highlighted.

Following this review on intrinsic properties, an analysis of laser processing was also performed, explaining different ways on how the properties above can be modified. Micromachining and LIRIC have been found to be of special interest for integrated optics, and hence, its performance was compared with other techniques.

2.2 DIFFERENT PROCESS AFFECTING MATERIAL REFRACTIVE INDEX

In the previous section, laser processing has claimed to exhibit many applications. Among all of them, Laser Induced Refractive Index Change (LIRIC) draws attention to manufacturing new photonics devices. The Refractive Index Change is caused by one or many structural changes that affect Refractive Index. In this section, a review of the most common processes that affect the RI will be addressed.

13 In some cases centimeters thick.

14 Unless CVD is performed while the material is being manufactured, as in the case of optical fibers.

15 And vicinity in function of laser type and parameters.

16 Generaly, Ga^{+}.

17 $\lambda = \frac{h}{mv}$, for a proton traveling at 255*10^6 m/s for example λ = 1.55 fm.

2.2.1 KRAMERS-KRONING RELATION

As mentioned in section 2.1.1.2, RI is a complex linear passive system holomorphic[18] in the upper complex ω. This property stems from the principle of causality, which states that *effect* cannot precede the *cause*. This principle can be applied to relativity to address the term *relativistic causality* that states, no signal can propagate Faster Than Light (FTL). Causality indicates that no scattered wave can exist before the incident wave has reached the scattering center. This implies that optical systems are analytical in the upper complex plane and which makes real and imaginary parts not independent but connected by a special form of Hilbert transforms, which are termed Kramers-Konig relations (KKr).

Kramers-Konig relations describe a fundamental connection between the real and imaginary parts of linear complex optical functions descriptive of light-matter interaction phenomena. In the case of RI, KKr are termed as follows [46]

$$n(\omega) = 1 + \frac{2}{\pi} P \int_0^\infty \frac{\omega' \kappa(\omega')}{\omega'^2 - \omega^2} d\omega' \tag{18}$$

$$\kappa(\omega) = -\frac{2\omega}{\pi} P \int_0^\infty \frac{n(\omega') - 1}{\omega'^2 - \omega^2} d\omega', \tag{19}$$

where P denotes the principal part of the integral. From Eq. 18 one can rewrite the equation as a function of absorption and wavelength and also assume a discrete amount of absorption spectrum changes ranging from λ_i^- to λ_i^+ to get RIC through derivation:

$$\Delta n(\lambda) = \frac{1}{2\pi^2} \sum_i P \int_{\lambda_i^-}^{\lambda_i^+} \frac{\Delta\alpha_i(\lambda')}{1 - \left(\frac{\lambda'}{\lambda}\right)^2} d\lambda'. \tag{20}$$

The equation above clearly shows how KKr state that a change in absorption spectra implies a change in RI real part as well and vice-versa. Changes in the absorption spectra can be caused by structural or chemical changes in the material. For example, dopant addition is a way to increase/reduce RI of optical fiber core/cladding. Dopants can drastically modify the carrier's rate of the material, which strongly affects absorption. Another example is defect generation, in this case, the structural sequence of the material exhibits anomalous changes and broken bonds that again alter absorption spectra.

2.2.2 LORENTZ-LORENZ RELATION

Another way to influence Refractive Index is through density changes. This is somehow intuitive as compaction/expansion implies more/fewer atoms per unit volume and hence a change in its dielectric constant. In the presence of an electric field, these atoms will generate a dipole moment[19] proportional to the total electric field by polarizability α which influences permittivity through the following relation:

18 A holomorphic function is a complex-valued function of one or more complex variables that is, at every point of its domain, complexly differentiable in a neighborhood of the point.

19 Atoms, even electrically neutral, they still are composed of a positively charged core and a negative electron cloud and hence these two regions are influenced by the field, one pushed in direction of the field and the other in the opposite way.

$$\epsilon_r = 1 + \frac{N\alpha}{\epsilon_0 - N\alpha/3} \tag{21}$$

Where N is the number of atoms per unit volume. This equation may be solved for polarizability

$$\alpha = \frac{3\epsilon_0(\epsilon - 1)}{N(\epsilon + 2)} \tag{22}$$

which is the $Clausius - Mossotti$ equation [47]. From here, relation RI and density can be deduced:

$$\frac{n_0^2 - 1}{n_0^2 + 2} = \frac{N\alpha}{3\epsilon_0} = \frac{4\pi\alpha}{3V}. \tag{23}$$

V is the molecular volume, n_0 is the initial isotropic RI, this is the so-called Lorentz-Lorenz relation [48]. Through derivation, one can get

$$\frac{\Delta n}{n_0} = \frac{(n_0^2 - 1)(n_0^2 + 2)}{6n_0^2}\left(\frac{\Delta\alpha}{\alpha} - \frac{\Delta V}{V_0}\right) \tag{24}$$

$$\Delta n = \frac{(n_0^2 - 1)(n_0^2 + 2)}{6n_0}(\Omega - 1)\frac{\Delta V}{V_0} \tag{25}$$

where $\Omega = \frac{\Delta\alpha}{\alpha}/\frac{\Delta V}{V_0}$ is the change of polarizability with compaction and also note that $\frac{\Delta V}{V_0} = tr(\overline{\overline{\epsilon}})$ with $\overline{\overline{\epsilon}}$ as the strain tensor [47]. Strain is the geometric lenght change rate respect the original position along the body axis. Eq 25 shows that an expansion/desification induces a isotropic RIC proportional to $(\Omega - 1)$. In silica glass $\Omega \approx 0.2$ [49] giving $\Delta n \approx -0.8\epsilon_0$ for $n_0 = 1.445$ where $tr(\overline{\overline{\epsilon}}) = 3\epsilon_0 < 0$ for densification[20].

Strain can be either permanent or elastic. The first one is isotropic while the latter always implies a stress field following Hooke's law. Stress produces interesting changes are discussed in the section below.

2.2.3 ELASTO-OPTIC EFFECT

When a material is subjected to a field of elastic stress, it suffers an elastic deformation. The local density of the latter is modified and therefore its optical properties are also modified as seen in section above. Stress σ and strain are related by Hooke's law [49]

$$\epsilon_{ii}^e = \frac{1}{E}\left[(1 + \nu)\sigma_{ii} - \nu\sum_i \sigma_{ii}\right] \tag{26}$$

and hence, they can be used interchangeably. The elasto-optic effect in materials couples the mechanical stress or strain to the Refractive Index. When a stress is applied to a body, the dielectric tensor is modified, and it may be assumed that the changes in the components of the dielectric tensor are related to the stress components

20 Densification is always isotropic, otherways is called linear contraction.

$$\Delta\overline{\overline{\eta}} = -\frac{2}{n_0^3}\Delta\overline{\overline{n^e}} = \overline{\overline{P}}\,\overline{\overline{\epsilon^e}}. \tag{27}$$

In this equation, $\overline{\overline{\eta}}$ is the inverse permittivity tensor[21], $\Delta\overline{\overline{n^e}}$ is the anisotropic elastic RIC, $\overline{\overline{P}}$ is the elasto-optic tensor composed of p_{ijkl} components and $\overline{\overline{\epsilon^e}}$ is the elastic strain tensor. Due to the symmetry of the photo-elastic and elastic strain tensor, $p_{ijkl} = p_{jikl} = p_{ijlk}$ and $\epsilon^e_{ij} = \epsilon^e_{ji}$, the subscripts *ijkl* can be contracted to *mn*, where m and n take the values from 1 to 6 (1, 2, 3, 4, 5, 6 for xx, yy, zz, yz, xz, xy), one can rewrite Eq. 27 to obtain the components of $\Delta\overline{\overline{n^e}}$ [50, 47, 51]:

$$\begin{pmatrix} \Delta n^e_{xx} \\ \Delta n^e_{yy} \\ \Delta n^e_{zz} \\ \Delta n^e_{zy} \\ \Delta n^e_{xz} \\ \Delta n^e_{xy} \end{pmatrix} = -\frac{n_0^3}{2} \begin{pmatrix} p_{11} & p_{12} & p_{12} & 0 & 0 & 0 \\ p_{12} & p_{11} & p_{12} & 0 & 0 & 0 \\ p_{12} & p_{12} & p_{11} & 0 & 0 & 0 \\ 0 & 0 & 0 & \frac{1}{2}(p_{11}-p_{12}) & 0 & 0 \\ 0 & 0 & 0 & 0 & \frac{1}{2}(p_{11}-p_{12}) & 0 \\ 0 & 0 & 0 & 0 & 0 & \frac{1}{2}(p_{11}-p_{12}) \end{pmatrix} \begin{pmatrix} \epsilon^e_{xx} \\ \epsilon^e_{yy} \\ \epsilon^e_{zz} \\ \epsilon^e_{zy} \\ \epsilon^e_{xz} \\ \epsilon^e_{xy} \end{pmatrix}. \tag{28}$$

Note that p_{11} and p_{12} are the Pockels coefficients[22]. Eq 28 shows that unlike expansion/densification caused by a permanent strain, elastic strain RIC is anisotropic, causing birefringence. The later is usually weak, causing retardances about 40nm.

2.2.4 FICTIVE TEMPERATURE

The structure of a material plays a decisive role in its properties. This structure is highly dependent on the thermal history of the material. Quenching and annealing can greatly change the properties of a material such as volume, Young's modulus or etching rate. A useful parameter to measure the internal disorder of a glass structure is the fictive temperature (T_f).

The fictive temperature of a non-equilibrium substance can be defined as the temperature of the same substance in an equilibrium state when the internal structure is similar to the current non-equilibrium state. When the fictive temperature is applied to glasses, it becomes the last temperature reaching equilibrium (liquid state) before reaching room temperature through a fast cooling.

More specifically, in the case of glasses, when the temperature is above the melting point if the glass experiences a fast cooling below the melting point, due to a lack of crystalline cores or high viscosity, it remains as a supercooled liquid instead of crystallizing. As the supercooled liquid is being cooled down, viscosity increases, and also the time required to perform structural relaxation. In the liquid state, relaxation processes are almost instanta-

21 $\eta = \frac{1}{\epsilon_r}$, a change of notation has been performed for the sake of clarity as both permittivity and strain use the epsilon letter.

22 For bulk glasses at 632nm $p_{11} = 0.126$ and $p_{12} = 0.26$ [52]. For fibers at same wavelength $p_{11} = 0.113$ and $p_{12} = 0.252$ [53].

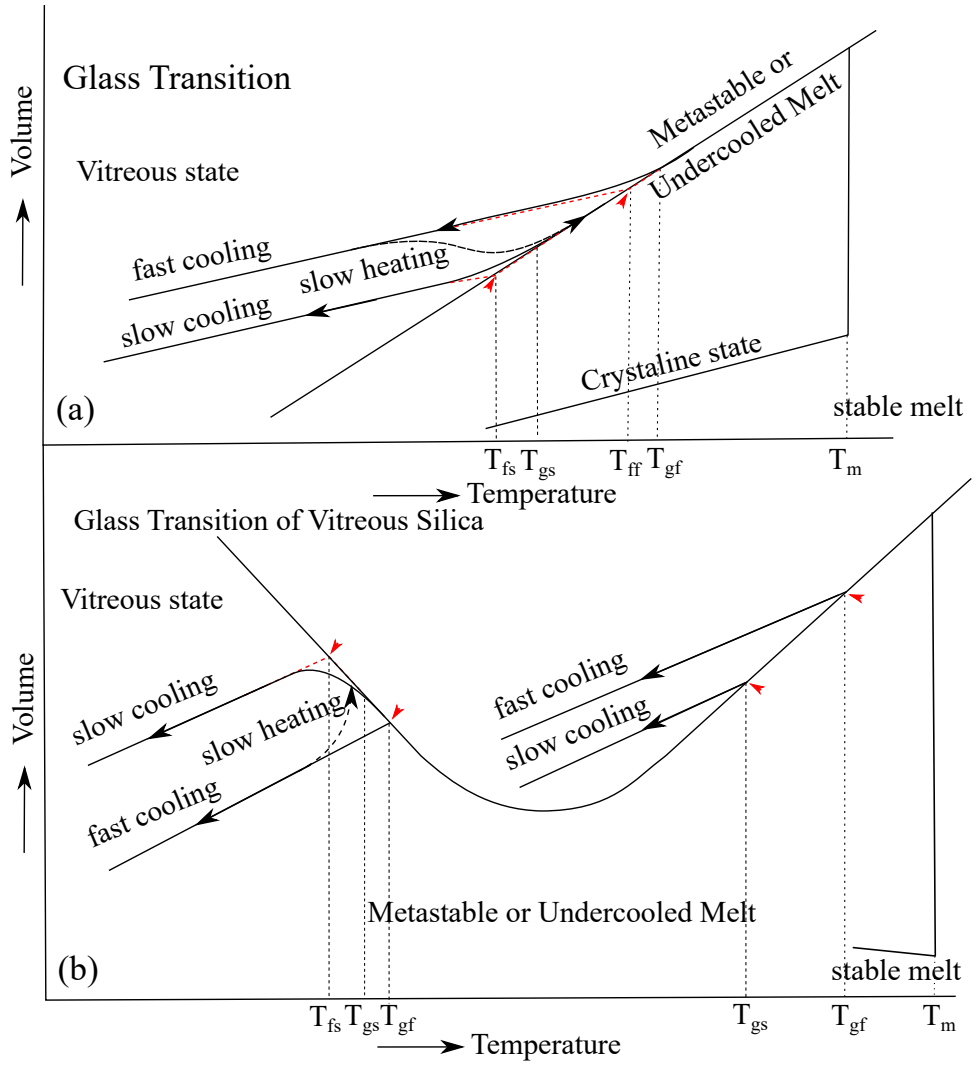

Figure 5: Transition curves for: common glass (a), vitreous silica (b) [54].

neous compared to the observation time, allowing the system to be regarded as ergodic[23]. However, the supercooled liquid exhibits relaxation times of the same order than measuring time, thus as the system cools, it will eventually exhibit an ergodicity breakdown. This change is represented by the glass transition temperature T_g, which is the temperature at which the viscosity reaches 10^{13} poises. At this state, any further irreversible cooling process will lead to a temperature change where the structure cannot relax accordingly, thus remaining *frozen* while glass solidifies. The solid glass deviates from the liquid curve as depicted in Fig. 5.a due to the even higher viscosity at the solid state that produces a smoother curve. In Fig. 5.a, both T_g and T_f are depicted. It is clear that these two temperatures depend on the cooling process, achieving a higher T_f at faster cooling. This implies a volume increment (thus, RI decrement) with T_f.

23 Ergodic hypothesis assumes that the measuring time of a macroscopic parameter for a given system is far larger than the particle timescales conforming the system. The microstates of the particles visit all the values of the phase space in the measurement time, being the phase-averaged function equivalent to the time-averaged function.

In the case of fused silica, its curve diagram exhibits anomalous behavior. Fig. 5.b depicts the volume curve of fused silica with an anomalous region for 1000-1500°C. In this region, an increase of fictive temperature implies densification following the relation [55].

$$\rho\left[g/cm^3\right] = 02.1898 + 9.3 \times 10^{-6} T_f\,[^oC]\,. \tag{29}$$

The fictive temperature plays a role in many other properties. Silica optical fibers, for example, exhibit an increase in Young's modulus and Rayleigh scattering with the increase of fictive temperature [37].

2.2.5 SUMMARY

This section has shown that RI depends on several parameters. Structural changes that alter absorption or polarizability, Density changes caused by a quick heat and cooling process or by permanent strain, even stress can produce RIC. LIRICs can be explained by one or more of these relation. In the following section, LIRICs caused by fs lasers will be explained in more detail.

2.3 THE FEMTOSECOND LASER

A femtosecond laser emits pulses of 1 to 1000 femtoseconds durations. They were developed in the 80s [56, 57] and their improvement continues until today. Their short pulse duration allows high peak power and operation in a shorter time scale than different physical processes of the material. This property makes femtosecond laser very attractive for optical material processing. In this chapter, a quick glance of different techniques for ultrashort pulse generation through history will be performed followed by a review of different processes produced by ultrashort pulse irradiation to conclude in a summary of the potential applications of this technology to optical material post-processing.

2.3.1 STATE OF THE ART OF FEMTOSECOND LASER TECHNOLOGY

In order to generate short laser pulses, there is a lot of special techniques applied to the laser cavity and pump source. Q switching[24] technique can led to nanosecond pulses. Some mode-locking[25] arrangements can led to shorter pulses. For example, a mode-locked pump laser matching cavity length using synchronus pumping technique can generate

24 Q-switching is achieved by putting some type of variable attenuator (or shutter) inside the laser's optical resonator. When the attenuator is functioning, light which leaves the gain medium does not return, and lasing cannot occur. As stimulated emission is low due to the cavity effect cancelled by attenuator, the amount of stored energy increases due to continued pumping until some critical value is reached (as another emission effects such as spontaneous emission start to balance tha gain caused by pumping). In this moment the Q factor is switched from low to high. Because of the large amount of energy stored in the gain medium, the intensity in the laser resonator builds up very quickly; this causes the energy stored to be depleted almost as quickly. The net result is a short pulse $\approx$ ns which may have a very high peak intensity.

25 Mode-locking takes advantage of longitudinal modes. This modes stems from the resonant condition of laser cavity $L = q\lambda/2$ being L the cavity length and q an integer representing the mode order with a frequency spacing between orders of $\delta\nu = c/2L$. All of this orders ussually exhibit stochastic phases between others. When the number of longitudinal modes is sufficiently high, their random superposition constitutes an interference pattern with promediated value (Continuous Wave (CW)). However, when exhibit the same amplitude and initial phase value, the quantity of modes N=2n+1 produces the following overlapped electric field

picosecond pulses, in order to generate femtosecond pulses, even more complex techniques are required.

First attempts to generate fs pulses were performed trough dye lasers with the Colliding Phase Mode-locking (CPM) technique were an absorber inside a ring resonator achieves passive mode-locking in a CW dye laser [58]. Unfortunatelly, dye lasers exhibit *several*[26] drawbacks for their extended use and commercialization. Later, self-modelocking Ti:sapphire lasers [59] substituted dye lasers, being the key technology on many commercial laser systems up to now. Parallel to this trend, Erbium fiber lasers achieved also high commercial demand due to intrinsic compaction of optical fiber [60]. However, ultrafast fiber lasers exhibited low pulse energy compared to Ti:sapphire, being unreliable for micromachining [58].This issue was fixed with the implementation of Chriped Pulse Amplification (CPA), this technique implies pulse stretching[27] in time to linearly increase group velocity dispersion. This in turn reduces peak power and prevents the gain media to be damaged while amplifying the stretched pulse. Once the pulse has been amplified, it is compressed through a compressor with opposite group velocity dispersion [61].

Fiber Chirped Pulse Amplified (FCPA) laser systems are able to operate at high levels of the nonlinear phase shift providing high-peak-power, high-quality pulses [62, 63]. Another noteworthy technology for high power lasing is Optical Parametric Amplification (OPA) developed thanks to the increased developement of nonlinear optical materials. Ultrafast OPAs are getting more important as a practical source of femtosecond pulses with tunable wavelengths across the visible and infrared spectral ranges. This technique stems from parametric nonlinearities[28] of non linear materials where coherent pump and seed light sources incide into a nonlinear material and converts pump photons into same number of seed photons and idler photons $\nu_{pump} = \nu_{seed} + \nu_{idle}$. As the pump energy is fully converted into energy of the desired signal and idler beams, the crystal material is not heated in this process. This phenomenon can also be produced in optical fibers thanks to their intrinsic $\chi^{(3)}$ nonlinearity. Fiber-laser-pumped parametric amplifiers can achieve peak powers of in the order of GW, becoming increasingly used for micromachining, imaging, and frequency comb applications [64].

The constant trend to develop shorter pulse sources has led to reach the attosecond scale ($1as = 10^{-18}s$) in 2001 [65] being the shortest pulse achieved 43 attoseconds [66].

$$E(t) = \sum_{q=-n}^{n} E_0 \exp i2\pi(\nu_0 + q\delta\nu)t = E_0 \exp i2\pi\nu_0 t \frac{\sin(\pi(2n+1)\delta\nu t)}{\pi\delta\nu t}$$

From here, it is clear that an increasing amount of in phase longitudinal modes interfere generating optical pulses of decreasing temporal width. Mode-locking involves several techniques (passive and active) that fixes mode phases in order to constructively interfere with each other similar to equation above.

26 They are expensive, complex, bulky and require several maintenance. First, gain media degrades due to photochemical effects. Second, its high fluorescence makes population inversion vanish in microseconds unless additives are added or mechanic methods are used to avoid continuous pumping to same region of gain media. Third, its wide broadband is achieved by the employ of different dye gain media, implying that laser cavity must drain the former gain media to introduce the new one.

27 Pulses stretching is achieved with a set of carefully designed diffraction gratings and lenses to force higher wavelengths to take less time to travel trough the device than lower wavelengths (positive dispersion, in negative counterpart the wavelength travel time is inverted).

28 optical nonlinearities with an instantaneous response based on the second order and third order nonlinearity of a medium, causing frequency doubling, sum and difference frequency generation, parametric amplification and oscillation.

However, such designs are still young technologies more oriented towards the study of electron motions and quantum effects than commercial material processing [67].

2.3.2 INTERACTION WITH OPTICAL MATERIALS

When a high intensity laser irradiates a material, an interaction with the system is produced (denominated absorption) that leads it out of equilibrium, subsequently suffering a relaxation process. Absorption can be divided into ionization and fragmentation. Ionization is produced when $E_{photon} > E_{gap}$ and mainly consist in the emission of an electron to an excited level to be emitted back to the fundamental level in a *direct* (the phenomenon is produced in same temporal range) or *indirect* (the phenomenon is produced a posteriori, being ruled by an statistic approach) way. Fragmentation is produced when internal vabrational energy of material is higher than dissociation energy. In this case, initial system (called *father*) is fragmented into smaller systems (again, its origin may be of statistic nature).

Ionization exhibits a huge interest and hence will confer the appropriate context for ultrafast and ultraintense lasers. In this context, there are two major types of fundamental ionization for the study of irradiated matter, Multiphoton Absorption (MPA) and tunneling ionization.

2.3.2.1 *Multiphoton absorption*

This first type is manifested at moderate intensities ($10^{10} - 10^{13} W/cm^2$) at several photon energies. It simply consist in the absorption of n photons whose energy addition surpasses E_{gap} releasing an electron from valence band to conduction band in exchange (depicted in Fig. 6.a). The energy balance is given by

$$E_c + E_{int} = N\hbar\omega - E_{gap}, \tag{30}$$

where E_c is the electron's kinetic energy in conduction band and E_{int} is the internal vibrational energy of the system.

The absorption rate (Γ_N) decreases with required photon number N to surpass E_{gap} and exponentially increases with laser irradiance [68]

$$\Gamma_N = \sigma_N I^N, \tag{31}$$

being σ_N the N photon absorption crossection (which significantly decreases with N). Γ_N shows how rate becomes more and more strongly dependent on irradiance with the increase of required photon number.

2.3.2.2 *Tunneling ionization*

If laser's electric field is on the same order as Coulomb's atomic potential and its frequency is low, the laser radiation may distort atomic band structure reducing E_{gap}[29] enough to allow tunneling effect (depicted in Fig. 6.b). These two ionization ways are found in the same study frame thanks to Keldysh work, where transition between this two regimes is shown through Keldysh parameter:

29 Even completely suppressing this potential sometimes.

$$\gamma = \sqrt{\frac{E_{gap}}{2U_p}} = \sqrt{\frac{\epsilon_0 m_e c E_{gap} \omega^2}{q^2 I}}. \tag{32}$$

Here, ponderomotive energy is introduced, which is the average oscillation energy adquired by a free electron in a high electromagnetic field

$$U_p = \frac{q^2}{2m_e \epsilon_0 c \omega^2} I = 9.34 * 10^{-20} \lambda^2 * I. \tag{33}$$

It is shown that Keldysh parameter on laser irradiance and wavelength. When $\gamma > 1$, the system is within the perturbative non lineal regime where MPA predominates. If $\gamma << 1$ which is asociated to low frequency and moderated-high energy, then system is in a intense field regime where tunneling ionization prevails. When inscribing waveguides, $\gamma \sim 1$ [69] suggesting a combination of both processes (Fig. 6.c).

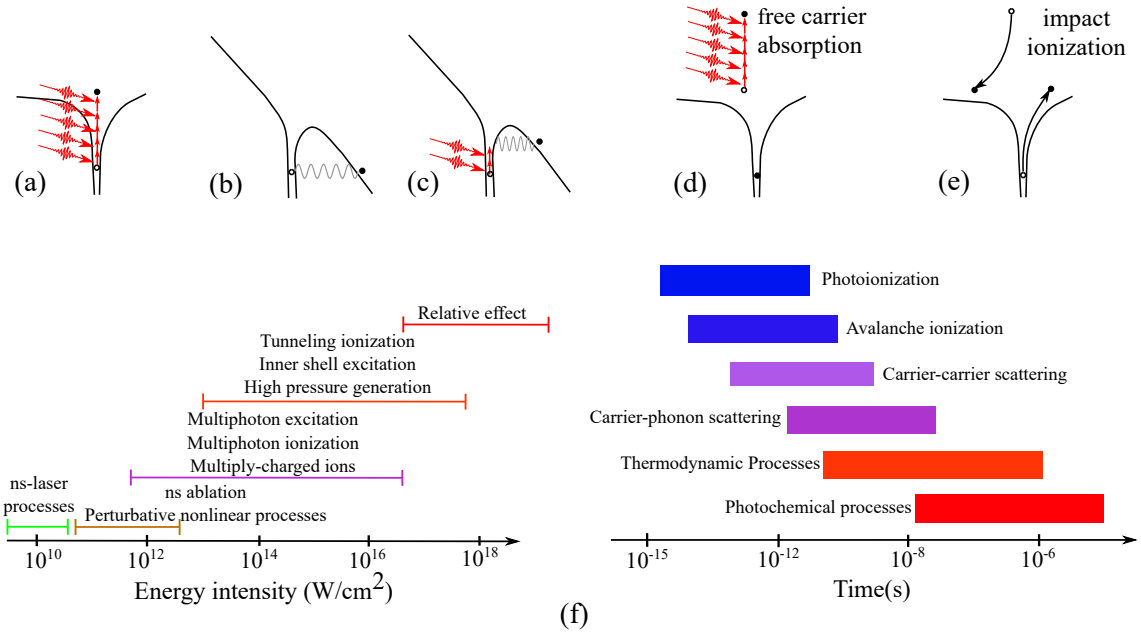

Figure 6: Absorption processes: MPA (a), tunneling ionization (b), combination of both (c), free carrier absorption (d), impact ionization (e) and energy/timescales of different light-matter interaction processes (f).

2.3.2.3 *Avalanche Ionization*

In addition to aforementioned processes, there is a third relevant ionization process that occurs when a free electron produces an impact ionization. Basically, a free electron in conduction band lineally absorbs n photons and ascends to the higher levels of the band (Fig. 6.d). When its kinetic energy (the energy difference between ground level of conduction band and the upper level where electron is placed) is higher than E_{gap}, the electron may excite another electron from valence band into the conduction band, resulting in two electrons in conduction band (Fig. 6.e) that can absorb photons again to repeat the process. This process manifests as long as laser radiation is present, increasing its frequency rate with time due to carrier increment. This phenomena exponentially increases electron density in conduction band in the following way [70]:

$$\frac{dN}{dt} = \eta N. \tag{34}$$

This process requires the presence of seed electrons that may be found in impurities, thermally excited electrons or by aforementioned processes. In the case of picosecond or wider pulse lasers, this is the most common process[30], and hence conferring a statistical behavior to the whole laser-matter interaction as avalanche ionization strongly depends on initial seed electrons.

In the case of fs laser pulses, the ionization relies more on MPA and tunneling ionization achieving deterministic behavior. In laser pulses with a duration shorter than picoseconds, the absorption processes are being produced during a temporal scale lower than lattice energy transferring processes, being absorption processes and lattice heating decoupled.

Electron density (N), grows due to avalanche ionization until free electron plama frequency[31] reaches laser frequency. In that moment, plasma becomes overdense[32] and highly absorbent as it reaches free electron critical density.

2.3.2.4 *Comparison with ns pulses*

Once electrons have been excited, their temperature is higher than lattice thus, they must exchange energy until a thermal equilibrium is reached [71]. Taking a look into Fig 6.f, the different time scale of light-matter effects can be noticed. Photoionization and avalanche ionization are the fastest processes ranging the fs scale, being photochemical processes the slowest as light must interact with the whole molecule. Carrier-phonon scattering are inelastic electron phonon collisions that transfer energy to the lattice, their timescale ranges around picosecond scale, thus, in ultrashort pulses heat transfer to the lattice can only be produced *after* the pulse. This is a key concept to understand the differences between ultrashort and common laser processing. In longer pulses, electron and lattice temperature reach the equilibrium *within* the pulse [72]. These pulses generate a temperature raise above melting point while each pulse is still active, making ablation or other processes carried out thermally, causing a large heat affected zone and leaving behind thermally induced defects such as cracks and chipping.

When electrons transfer energy to the lattice through inelastic electron-phonon collision, several structural changes occur that lead to different macroscopic changes. These can classified into Type I-III explained below.

2.3.2.5 *Type I*

The first macroscopic effect that fs lasers can produce at relatively low pulse energies (E_p)[33] is a smooth isotropic Refractive Index Change (RIC) [73]. Its threshold states the first effects asociated to optical breaking but below catastrophic breackdown. When this change is manifested alone, it ussually exhibits changes ranging from $\Delta n \approx 10^{-4}$ to $\Delta n \approx 10^{-3}$ and when is acompanied by higher types (usually by filamentation process caused by self-

30 The avalanche ionization contribution increases with pulse duration and material E_{gap}.

31 $\omega_p^2 = \frac{Ne^2}{\varepsilon_0 m_e}$.

32 With this carrier density, only a tiny portion of incident light is reflected, having the remaining light absorbed.

33 Ranging from 0.1 to 0.5 μJ at NA=0.65 [73].

focusing[34]) can reach $\Delta n \approx 10^{-2}$ being this later often associated to stress deposition. There are no exact consensus about the mechanism that cause this index change [49]. There are several proposed mechanisms as a function of the material. In the particular case of fused silica, one proposed mechanism is defect formation. Particularly nonbridging oxygen hole centers (NBOHCs) and E' centers[35] are though to contribute trough KKr and defect-induced densification to the RIC. However, this cannot be the only mechanism as these defects that would be commonly ereased at 200 °C annealing while type I RIC can resist up to 1000°C. In fact, these defects increase with the annealing when they are produced by type, implying the presence of more underlying rearrangements of the silica matrix [75]. Other alternative explanation is that the electron plasma, when transfers heat to the lattice it quickly heats and cools the affected zone, changing its fictive temperature (T_f) and hence producing permanent densification/expansion.

Fig. 7.I depicts several lines inscribed at $w_s = 100\mu/s$, PRR = 200kHz with different pulse energy (E_p) captured by transmission microscopy and with de Sénarmont compensation technique (birefringence meassurements, see section 4.3.3). Those with lower E_P do not exhibit retardance thus they are isotropic. It should be pointed out that type I modifications can exhibit small stress induced birefringence caused by permanent densification/expansion [73].

2.3.2.6 *Type II*

When pulse energy (E_p) increases above a higher threshold of 0.31 μJ (for $\lambda = 800nm$, $\tau_p = 160fs$, 200kHz and NA = 0.5 when the irradiated material is fused silica) [78], and several pulses are delivered to the same volume with enough Pulse Repetition Rate (PRR) to interact with each other[36], a large birefringent and negative RIC emerges. It can be as large as $\approx 2x10^{-2}$ [35] with remarkable thermal stability [79]. The induced birefringence is not related to stress as in type I but to the formation of sub-wavelength features of the

34 Self-focusing is a direct cause of optical Kerr effect. This phenomena stems from taking into account third non-linear susceptibility $\chi^{(3)}$ in polarization **P**. By rearranging elements to a single χ and then turning it into a RI ($n = (n_0 + \chi)^{1/2}$) one can get

$$n = n_0 + n_2 I.$$

RI depends on Intensity of irradiated field. This effect only becomes relevant at high intensities as n_2 value is quite low ($\approx 10^{-20} m^2/W$ for typical glasses). In the case gaussian pulses, RI will exhibit a graded profile affecting the pulse in a similar way than a lenses, thus colapsing the pulse when reaching certain critical peak power threshold [70]:

$$P_{cr} = \frac{3.77\lambda^2}{8\pi n_0 n_2}. \tag{35}$$

This compression leads to even higher intensities where a strong plasma is formed leading a local reduction of refractive index and defocusing the pulse.The self-focusing and plasma defocusing compete each other along the laser pulse propagation inside the medium. As a result, a long plasma channel, a filament, is formed [74].

35 Atomic structure of fused silica will be explained in section 4.4.3, but a brief explanation would consist in each silica atoms sharing four covalent bonds (this is, sharing electrons in order to fill respective last layer) with oxygen sharing one each. Defects to this configuration can be either oxigen-deficiency related or oxigen-excess related. Here, E' centers belongs the first type and NBOHCs the later. E' centers consist in a Si with three regular bonds and a free pair ($\equiv Si\bullet$). NBOHCs consist in a regular SI atom bonded to a oxygen atom with a free pair ($\equiv Si - O\bullet$). Defects posses a charasteristic photoluminescence/phosphorescence, being the NBOHC band 1.9eV, this bands generate absorption changes that modify the color of the glass in the afected zone, being called color centers.

36 When the time between pulses is less than the thermal diffusion time of the material.

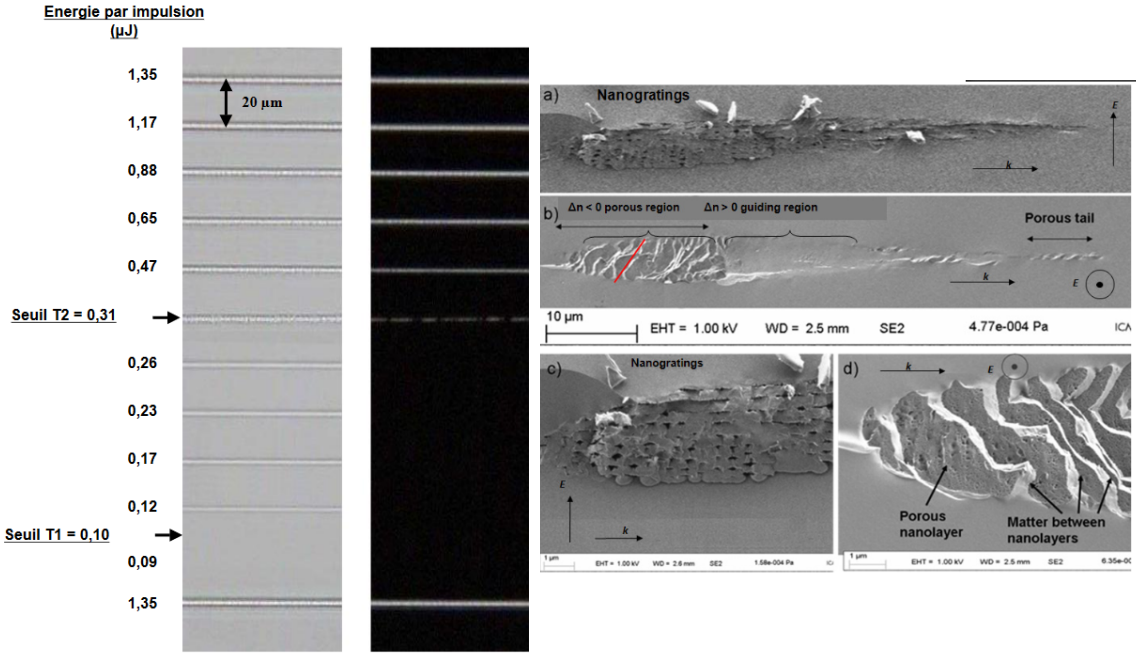

[Sudrie 2002] [Canning 2011]

(I) (II)

Figure 7: Microscope image of several lines inscribed by fs laser with the following parameters: $\tau = 160fs$ $NA = 0.5$, $\lambda = 800nm$, $PRR = 200kHz$ and $w_s = 100\mu/s$ in silica glass at several E_p (left). Same sample under the de Sénarmont compensation technique (birefringence meassurements, see section 4.3.3) (right) [76] (I). FEG-SEM, Secondary electrons images of laser tracks cross-section for each writing laser polarisation. The laser parameters were: 0.5 µJ/pulse, 1030 nm, 300 fs, 200 kHz, 200 µ m/s. A fosusing lens of 0.5 NA was used. With the laser polarisation perpendicular (a) and parallel (b) to the scanning direction. (c) and(d) show close-ups of the nanograting and nanoplane regions respectively [77] (II).

so-called *nanogratings* or *nanoplanes*. These structures are composed of several nano porous layers perpendicular to polarization direction where SiO_2 releases oxygen atoms through bond breaking [77]. The grating arrangement is thought to be caused due to an interference mechanism between pulse and somekind of seed element. These seeds have to be generated by multiple pulse depositions as nanograting formation requires several pulses per micrometer (from 10 to 100 pulses) [80]. Beresna et al. propose that polaritons created from MPA interfere with Self-Traped Excitons (STEs) creating the nanograting pattern [81]. STEs relax into defect formations that eventually leads to oxygen emigration [80].

In Fig. 7.II various Field-Emission Gun Scanning Electron Microscope (FEG-SEM) captures of laser tracks with polarizations perpendicular and parallel to scanning directions are depicted. The heads of laser track are composed of porous nanolayers distributed at constant spacing. This later depends on wavelenght rather than pulse energy [82] and is distributed perpendicular to laser direction. The birefringence achieved is higher than the one caused by stress and can be related to

$$\Delta n = n_e - n_o = \frac{n_1 n_2}{\sqrt{f_\perp n_2^2 + (1 - f_\perp))n_1^2}} - \sqrt{f_\perp n_1^2 + (1 - f_\perp))n_2^2}, \tag{36}$$

where $f_\perp = t_1/(t_1 + t_2)$ and n_1, n_2 are RI of porous and non-porous material. Similarly t_1 and t_2 are the material thickness.

2.3.2.7 *Type III*

When pulse energy E_p is high enough, the overdense electron plasma will be so populated that electrons will repel each other while confined in the material, generating pressures as high as terapascals [83]. Eventually, the plasma will collapse and generate a coulombian explosion. This will allocate focal volume material and will create a microvoid. In other words, a central rarefacted zone and a densified shell both exhibiting abrupt negative and positive RIC respectively. This sudden explosion can also generate microcracks.

2.3.3 FEMTOSECOND LASER POST-PROCESSING OF OPTICAL MATERIALS

The applications of fs lasers can be divided into three categories: surface modifications, bulk modifications and deposition techniques. Among surface modifications, any structural or geometrical rearrangement is comprehended. It can be used for surface texturing where many surface structures can be performed, including conical peaks [84], periodic gratings [85] and ripples [86]. This processing can be useful to increase absorption in solar cells [85] and to create hydrophobic surfaces[37]. Of course, fs lasers can be employed in surface micromachining, they can be used for scribing drilling and dicing with superior quality than longer pulse counterparts [72]. Besides, one unique application of fs laser processing of semiconductors is the ability to hyperdope[38] target materials. The key point in this process is that molten liquid phases can host more dopants than equilibrium solid phases. This was first introduced to silicon materials where several fs pulses exposure in the presence of a wide variety of dopant precursors led to a high dopant substrate with almost unity absorption broadband [87]. fs laser processing allows dopant incorporation at concentrations thousands of times above the solid solubility limit [88].

Deepening into plausible bulk applications, one direct application is fs waveguide inscription. Aforementioned Type I and II modifications can be used to create a confining region with higher RI[39] than surroundings allowing both week and strong guiding regimes[40] depending on pulse parameters and material composition. Propagation losses around $1 dB/cm$ have been achieved in Schott AF32 and Borofloat-33 glasses [89]. This can be applied not only to integrated photonic devices, but also for the fabrication of non-linear devices. Bulk modifications are not limited to index change, the irradiation of photosensitive gels can lead to the formation of 3D structures [90].

Finally, it is worth noting the potential of fs laser in nanoparticle formation [91] and Pulsed Laser Deposition (PLD) [92].

37 Studies showed that fs laser texturing of silicon in SF_6 yields microsize spikes whose contact angle can be varied with pulse fluence thus controlling the fluid penetration.

38 Hyperdope basically consist in doping a material at concentrations beyond equilibrium solubility limit without phase change.

39 The opposite procedure is also possible, two parallel lines with negative RIC can be inscribed, achieving lower index cladding and higher index core due to stress accumulation, these are called *Type III waveguides*.

40 This is possible thanks to the wide range of RIC that fs laser can produce (from 10^{-4} to 10^{-2}).

2.3.4 SUMMARY

This section has performed a review of femtosecond lasers from multiple points of view. First of all, a state of the art of fs laser technology has been performed. Here, attention was drawn towards Chirped Pulse Amplification (CPA) laser systems and ultrafast Optical Parametric Amplification (OPA). The discussion was then focused on the interaction of optical pulses with matter. The nonlinear absorption processes combined with a pulse duration lower than the carrier-phonon interactions allow high control over the processed region with few heat deposition to the lattice. These pulses can perform three types of modifications in function of pulse energy and pulse deposition. Type I produces a smooth RIC attributed to many physical processes while type II modifications produce strong negative form birefringence. This phenomenon is produced by consecutive exposition to laser pulses of average intensity that produce porous nanolayers. Finally, type III produces ablation in the focal volume that leads to nanovoids.

The processing of femtosecond lasers can be divided into surface modifications, bulk modifications, and deposition techniques. One of the most interesting applications for the thesis outcome is the inscription of waveguides. Propagation losses can be as low as 1dB/cm and can be inscribed by several methods, exhibiting high potential for sensor manufacturing.

2.4 POST-PROCESSING OF OPTICAL FIBERS

Since Elias Snitzer proposed in 1961 for the first time that a fiber waveguide can behave as a Fabry-Perot Interferometer [17], the outstanding potential of fiber optic as a sensing element continues to be exploited up to the present. The possible ways that sensing can be achieved or improved is still enormous and more works with new methods of fiber sensing are being published every year. This massive amount of fiber research is paired with the number of ways optical fiber can be post-processing. This post-process techniques mentioned at the beginning of the chapter allow the manufacturing of several structures with applications not only to sensors but also to telecom. In this section, the focus will be placed into the state of the art of the wide amount of fiber structures relevant to the thesis outcome.

2.4.1 FIBER BRAGG GRATINGS

In 1913 W.L. Bragg demonstrated that incident rays to a crystalline structure are reflected when a specific condition is fulfilled due to the periodic arrangement of atomic structure [93]. This relation allowed diffraction of photons, neutrons and electrons to be used for crystalline lattice study.

Bragg, basically, reduced the crystal into consecutive crystalline plates with period d that behave like mirrors, reflecting each one a tiny amount of radiation while the rest is transmitted. Two consecutive reflected rays exhibit an OPD of $2d\sin\theta$ as depicted in Fig. 8.a, thus, wavefronts with path differences equivalent to $\frac{m\lambda_o}{n}$ will constructively interfere (being m an integer). This gives rise to the Bragg law:

$$2dn\sin\theta = \lambda_B. \tag{37}$$

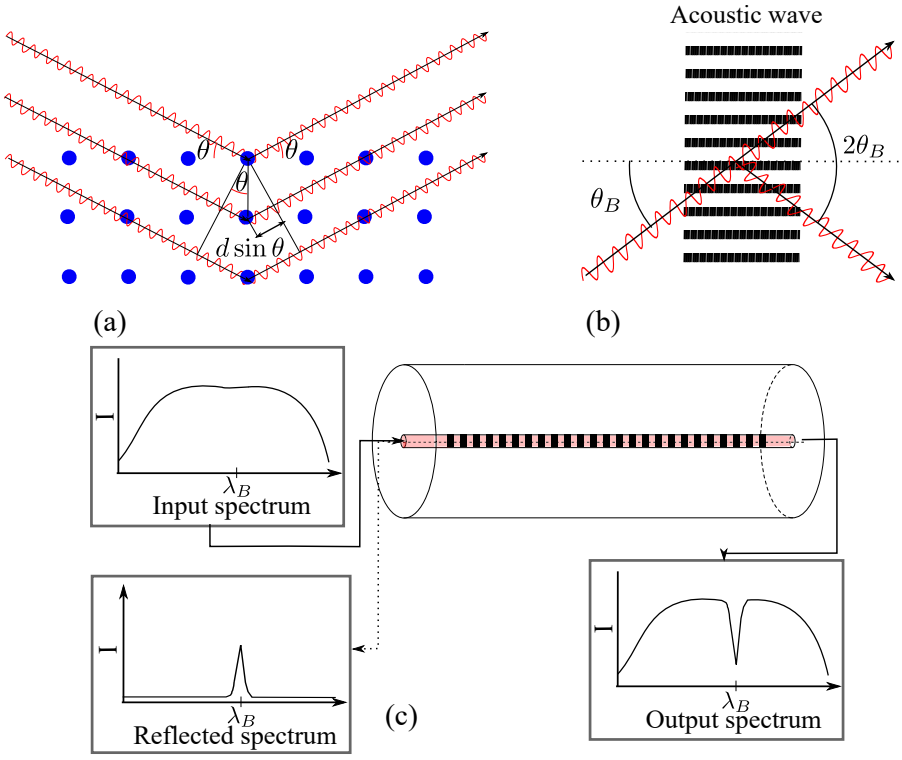

Figure 8: Examples of Bragg diffraction. In crystals (a), sound waves (b) and FBGs (c).

Here, λ_B is the so-called Bragg wavelength and n the refractive index. This equation predicts that for a given incidence angle θ, Bragg wavelength λ_B will be reflected while the rest of spectrum will be transmitted. As Bragg reflection will only be produced for $\frac{\lambda_0}{n} \leqslant 2d$ and atomic spacing is generally a few armstrongs, visible light can not be used, requiring the use of X rays or electron neutron irradiation as mentioned above.

Despite being originally discovered for lower wavelengths, this phenomena has been extensively studied for visible and infrared radiation as many structures exhibit a similar behavior at those ranges. Take for example ultrasound waves[41]. As they propagate, the air is compressed and expanded, generating a sinusoidal index change that can cause Bragg diffraction to incident electromagnetic waves (depicted in Fig. 8.b).

Bragg diffraction posses a strong niche in optical fibers, where periodic index modulations of fiber core along propagation direction may be inscribed. This kind of structures are called Fiber Bragg Gratings (FBGs) and in their most simple configuration, they reflect λ_B at $\theta = 90°$. In a similar way that a crystal lattice, they have a periodic RI modulation written at the fiber core that can be described as

$$\Delta n(z) = \frac{\Delta n_0}{2} + \sum_{m=1}^{\infty} \Delta n_m \cos\left(\frac{2\pi m z}{\Lambda}\right). \tag{38}$$

Δn_0 is the averaged RIC of the inscribed pattern and Δn_m is the amplitudes of the Fourier term m Each periodic modulation of the pattern decouples light from propagating mode to its counter-propagating counterpart generating a phase match between backscattered modes when fulfilled Bragg condition:

41 Over $\nu = 10^9$ Hz frequency.

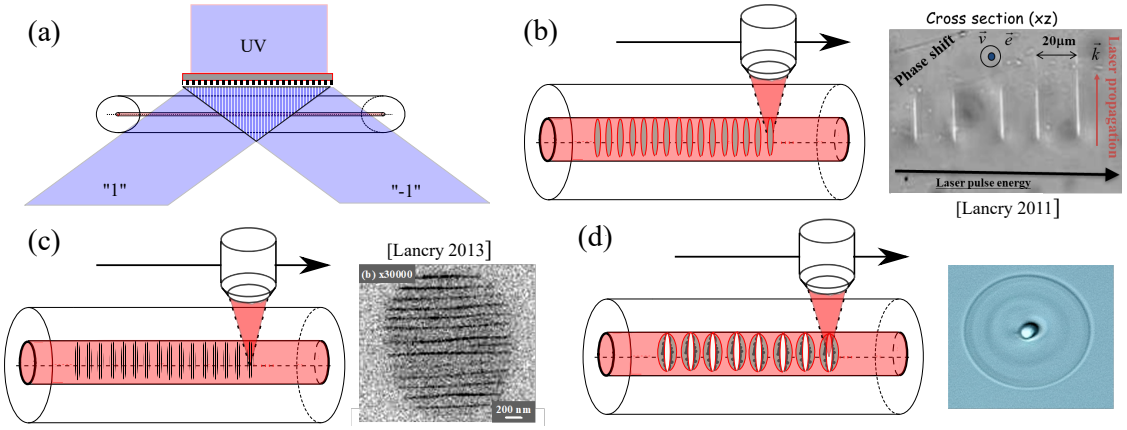

Figure 9: FBG classification: Type I-UV (a), Type I-fs [99] (b), Type II-fs [80, 77] (c), type III-fs (d).

$$\lambda_m = 2n_{eff}\Lambda/m. \tag{39}$$

Here, n_{eff} is the effective mode index inside FBG and λ_m is the resonant wavelength of the "mth" Fourier harmonic. Homogeneous sinusoidal patterns exhibit only one harmonic while nonsinusoidal patterns can exhibit up to Δn_4 strong amplitudes [94]. When this condition is satisfied, decoupling from propagation mode to backward mode will be maxed, not only generating a reflexion peak but also a transmission dip, filtering in this way Bragg wavelength λ_B. A more rigorous approach to the mode coupling can be performed by Coupled Mode Theory (CMT) [95]; however, the thesis scope will be more focused on potential applications and types rather than a full theoretical study.

FBGs are a mature technology that harness an outstanding potential for a wide variety of scenarios such as fiber lasers [96], optical communications [97] and sensing [2, 98]. This last potential stems on Λ and n_{eff}, these parameters can be greatly influenced by external forces. This is mainly the case of n_{eff} whose influence has been thoroughly revised in section 2.2, being λ_B sensible to a wide variety of changes. Parameters like Temperature (T), strain (ϵ) and presure (P) may shift Bragg wavelength. As an example, variation of λ_B for this three parameters can be described as:

$$\delta\lambda_B\lambda_B = C_{T\lambda_B}\delta T + C_{\epsilon\lambda_B}\delta\epsilon + C_{P\lambda_B}\delta P \tag{40}$$

$$C_{T\lambda_B} = \alpha + \zeta = \frac{1}{\lambda_B}\frac{\delta\lambda_B}{\delta T} \approx 11 pm/^\circ C \tag{41}$$

$$C_{\epsilon\lambda_B} = \frac{n_{eff}^2}{2}[p_{12} - \mu(p_{11} + p_{12})]\frac{1}{\lambda_B} = \frac{\delta\lambda_B}{\delta\epsilon} \approx 1.31 pm/\mu\epsilon \tag{42}$$

$$C_{P\lambda_B} = \frac{1}{\lambda_B}[\epsilon_z - \frac{n_{eff}^2}{2}[p_{11}\epsilon_r - p_{12}(\epsilon_r + \epsilon_z)]] = \frac{1}{\lambda_B}\frac{\delta\lambda_B}{\delta P} \approx -3.5 pm/MPa. \tag{43}$$

Thus, a change in one of these parameters can be easily determined by the measurement of the produced $\Delta\lambda_B$. This potential has motivated the study of FBG and the search of several configuration and manufacturing processes. The most common types of FBGs are classified as follows:

[Type I-UV] This FBGs typically are manufactured by a CW or ns UV-laser in photosensitive fibers, mostly Ge-doped or B-doped silica cores. They are inscribed using a

phase mask designed to suppress 0 "th" order and equally distribute +1,-1 diffraction efficiency. In this way, optical fiber is placed at near field regime, where +1 and -1 orders interfere with each other causing a fringe pattern and thus causing the RI modulation through color center formation [100] (depicted in Fig. 9.a). The resulting RIC exhibits a high quality sinusoidal pattern ($\Delta n_1 >> \Delta n_{m>1}$) over the entire core. This type is ubiquitous at telecom being able to last up to 25 years at temperatures between -25°C and 80 °C. This pattern is completely erased at 600-800°C [101].

[Type I-fs] A femtosecond laser employing the Point-by-Point (PbP) technique is used to inscribe "smooth" positive index changes[42] (induced densification) into the fiber core. In this case the grating is completely erased at 1000 °C [101, 102] (depicted in Fig. 9.b). PbP is a direct writing technique consisting in the proper control of PRR and writing speed to deposit pulses with the desired period. This technique is more complex than phase mask inscription, raising its effective cost [94]. The produced index profile is nonsinusoidal and is usually inscribed only in one section of the fiber core. These patterns usually lead to higher order resonances and coupling to higher order modes[43].

[Type II-fs] Type II porous birefringent nanostructures are employed to inscribe the FBG pattern. They can be stable up to 1200 °C for 10 hours [103] (depicted in Fig. 9.c) but exhibit high scattering losses.

[Type III-fs] Ablation threshold can be surpassed to produce nanovoids surrounded by a densified shell using PbP writing. Due to the mechanical modification, these gratings can be stable up to temperatures higher than 1000 °C [100] but exhibit a lower mechanical resistance due to ablation process (depicted in Fig. 9.d).

From this list, it is clear that temperature resistance implies several drawbacks that decrease the attractiveness of this technology. However, there is an increasing demand for this technology in the oil, drilling, smelt, aircraft and high power laser industries where FBGs must withstand high temperatures [104]. This is why the improvement of FBG technologies to adequately operate in harsh and extreme environments has become a rapidly growing field of research. This effort led to another type of FBG with high-temperature resistance and without the drawbacks above.

2.4.1.1 *Regenerated Fiber Bragg Gratings*

This type of FBG involves the complete erasure and resurrection of a seed FBG[44] through thermal annealing. Seed structure changes the thermal history of glass modifying local response to homogeneous thermal processes, having consequently different parameters in processed and unprocessed regions. This FBG can work up to 1295 °C with comparable losses [105].

42 These changes can be achieved without photosensitive fibers, unlike UV inscription[99].

43 In the CMT, the transversal coupling constant between two modes is

$$\kappa_{ab} = \int\int dx dy 2\epsilon_0 \Delta n_m(x,y) n(x,y) \mathbf{E_a^T}(x,y) \cdot \mathbf{E_b^{T*}}(x,y).$$

Here, if $\Delta n_m(x,y)$ covers the entire cross section of the fiber homogeneously, then the orthogonality relation will exclude coupling between different modes. However, an asymetric value of $\Delta n_m(x,y)$ produces light decoupling to higher m and l modes [94].

44 Usually type I-UV but regeneration may also be achieved using seed type I-fs[102].

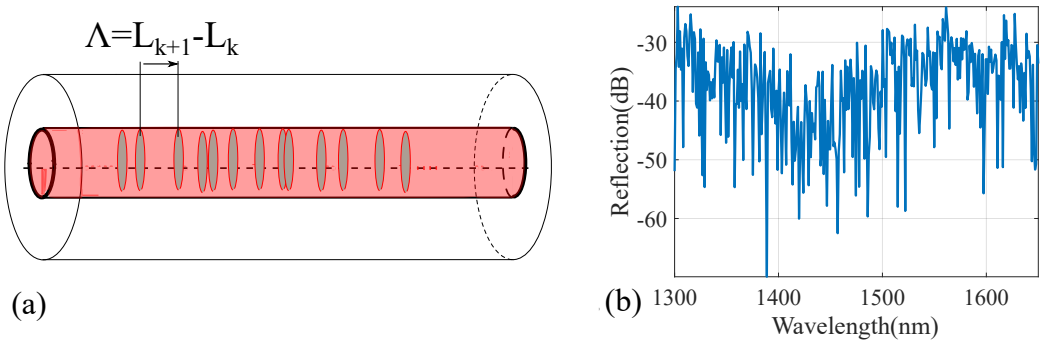

Figure 10: Diagram of RFG (a), reflection spectra of RFG (b).

There are several proposed mechanisms to explain this phenomenon such as dopant migration, crystallization or structural variations. Initially, dopant chemical migration was proposed for fluorine doped fibers where UV irradiance generates hydroxyl radicals. When a FBG is annealed, these radicals assist the fluorine diffusion thus producing fluorine concentration variations responsible for the RI modulation of regenerated grating [106]. Subsequent studies exhibit that fluorine is not necessary to achieve regeneration, Er-doped fiber with other dopants can also be regenerated [107]. Later works also found out that Er dopants are not necessary either, regeneration can be performed by a simple H-loaded germanosilicate fiber [108] due to molecular water modulation caused by thermal annealing [109]. Furthermore, regeneration may also be regarded as a polymorphic transition from metastable silica glass to a more ordered structure such as α-quartz due to a transition to tridymite through annealing and then converted to α-quartz through the cool back [104].

This proposed mechanism often neglects relaxation process and multi-material structure. Annealing involves structural relaxation, being the aforementioned mechanisms additional manifestations rather than possible causes. There is an increasing need for the local structural relaxation study in regeneration process, more specifically in multi-material systems interface as stress relaxation in optical fibers is strongly related to core/cladding interface. In order to overcome this need, some results of stress relaxation in multilayer regenerated Fiber Bragg Grating (rFBG) will be presented in section 4.4.3 performed by micro Raman spectroscopy.

2.4.2 RANDOM FIBER GRATINGS

Fiber Bragg Gratings have been shown to be promising devices whose key technology relies on an inscribed periodic modulation of RI to reflect/filter a single wavelength. In such structures, noise in periodicity is undesired as they can compromise their ideal optical properties. There are several works focused on the effect of noise[45] in optical fibers [110, 111, 112] and how to control its impact. However, noise can play a positive role in fiber grating fabrication in some cases where a broadband spectrum can be required [113, 114]. This gives rise to a new type of fiber grating fabricated with random phase, RI and period variations called Random Fiber Grating (RFG) [115].

45 Noise can be understood as any random or undesired perturbation in any relevant parameter for FBG characterization, namely phase, period RI etc...

In these gratings, as perturbations are randomly placed[46] (Fig. 10.a), light is partially reflected back any time it faces an inscribed perturbation. In contrast to UV phase mask inscription where the pattern covers the core homogeneously, a pointlike perturbation reflects light by scattering. Depending on the scattering angle, light can be reflected to the core or the cladding. These reflections instead of equally contribute to the same interference, independently interfere with their consecutive reflection, generating multiple FPI (core-core mode interference) and MZI (core-cladding mode interference) interferences. The overall interference pattern of the reflected irradiance I_r from the random grating can be theoretically expressed as [115]:

$$\begin{aligned} I_r &= I_0 \sum_{k=1}^{M} \sum_{k=1}^{M} \exp -\alpha(L_k + L_{k'}) r_k^{core} r_{k'}^{core} \exp i(\phi_k^{core} - \phi_{k'}^{core}) \\ &\quad + 2\bar{c} I_0 \sum_{k=1}^{M} \sum_{k=1}^{M} \exp -\alpha(L_k + L_{k'}) r_k^{core} r_{k'}^{clad} \exp i(\phi_k^{core} - \phi_{k'}^{clad}) \\ &\quad + \bar{c}^2 I_0 \sum_{k=1}^{M} \sum_{k=1}^{M} \exp -\alpha(L_k + L_{k'}) r_k^{clad} r_{k'}^{clad} \exp i(\phi_k^{clad} - \phi_{k'}^{clad}). \end{aligned} \tag{44}$$

Where α is the averaged attenuation of the unit-length random grating, L_k is the fiber length at k^{th} spot, r_k^{core}, ϕ_k^{core} and r_k^{clad}, ϕ_k^{clad} are the reflection coefficients and phase respectively of core and cladding modes at the kth spot respectively. From this equation, if phase and period distributions are truly random, then the interference patterns will combine in a noise-like shape with an average reflection over a broad spectrum. In Fig. 10.b, a common reflection spectrum is presented.

These RFGs are of particular interest for random fiber lasers. This kind of lasers operate with an open cavity where light is reflected back due to Rayleigh scattering. This phenomenon consists in the elastic[47] scattering of photons by atoms or other particles with a size lower than wavelength[48] [13]. In an optical fiber, small scale inhomogeneities (RIC caused by density and composition variations) produce this type of scattering. The reflectivity produced by Rayleigh scattering is quite low[49], therefore, several meters of fiber are required to produce enough backscattering. This requirement can be avoided employing a RFG where each reflector scatters light independently, reducing the amount of needed fiber.

The written reflectors by the fs lasers in addition to scatter light at the Mie regime[50] they also exhibits an increase of Rayleigh scattering due to structural changes involving higher disorder (T_f increment and defect formation) making them the ideal choice for these devices. Examples using fs direct writing to achieve RFGs have been reported in [115, 117] and, in section 5.2.2, the Point-by-Point (PbP) technique will be employed for RFG inscription in a Tapered Optical Fiber (TOF).

46 Period must exhibit wavelength-scale length.
47 Its inelastic counterpart, Raman scattering, will be studied in section 4.3.4.
48 In this regime, the defect can be approximated to an atom with a resonant frequency.
49 Reflection coefficient can be as weak as $r \approx 7.3 * 10^{-8}/m$ [115].
50 This regime governs light scattered by particles with sizes similar or bigger than the wavelength [116, 13].

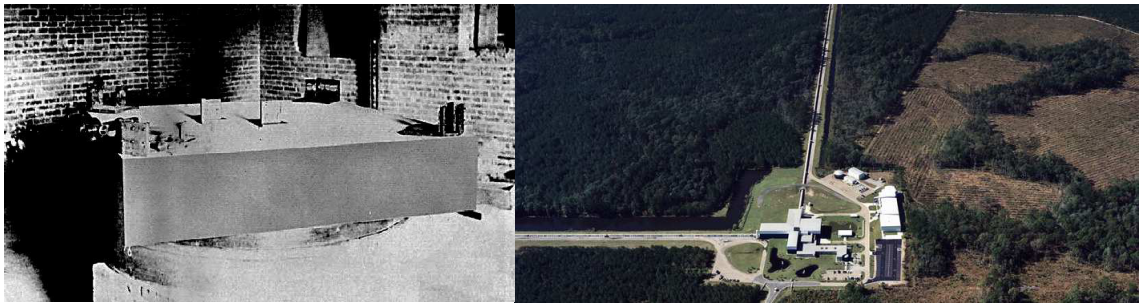

Figure 11: Image of the interferometric setup for Michelson and Morley's experiment in 1887 (left). LIGO observatory in Livingstone (right). The building is essentially a Michelson interferometer with 4 km arms length.

2.4.3 IN FIBER INTERFEROMETERS

Discovering of the interference effect was strongly related to the development of wave optics. Its first reported use in its early stage was the experimental prove of wave nature of light. With this purpose, Young stated the principles of interference in his Bakerian lectures in 1801 and 1803, demonstrating that ray superposition can lead to darkness with his well-known interferometer which is the original version of the modern double-slit experiment. Over the following decades, more and more effort was placed in the understanding of light nature and behavior, giving rise to a wide variety of interferometers in order to collect experimental evidence. One of the most famous experiments of these decades was the Michelson-Morley experiment where optical interference reliably discarded the aether concept and laid the foundations for the special theory of relativity [118].

The designed interferometer for such experiment, the Michelson interferometer, has been widely used for countless applications and experiments, remaining its key concept intact up to the present. In fact, it was used to detect one of the most revolutionary discoveries of the decade, the gravitational waves [119]. In Fig. 11, one can see the setup for Michelson-Morley experiment and the Laser Interferometer Gravitational-Wave Observatory (LIGO) facility at Livingston. The entire building may be regarded as a giant Michelson interferometer whose arms are 4 km in length. This is an excellent example of how interferometers from XIX century are still used with very specific configurations depending on the measured parameter.

Interferometers not only can be adapted to building like sizes, but also can be manufactured on a micro scale and here is where Single Mode Fiber (SMF) comes into play. Due to the large optical path that fibers can accommodate, they are magnificent mediums for different kinds of interferometers, being the amount of reported in fiber interferometers massive.

The underlying motive for this continuous research of optical fiber interferometers is stated in the interference equation

$$I = I_1 + I_2 + 2\sqrt{I_1 I_2}\cos\delta. \tag{45}$$

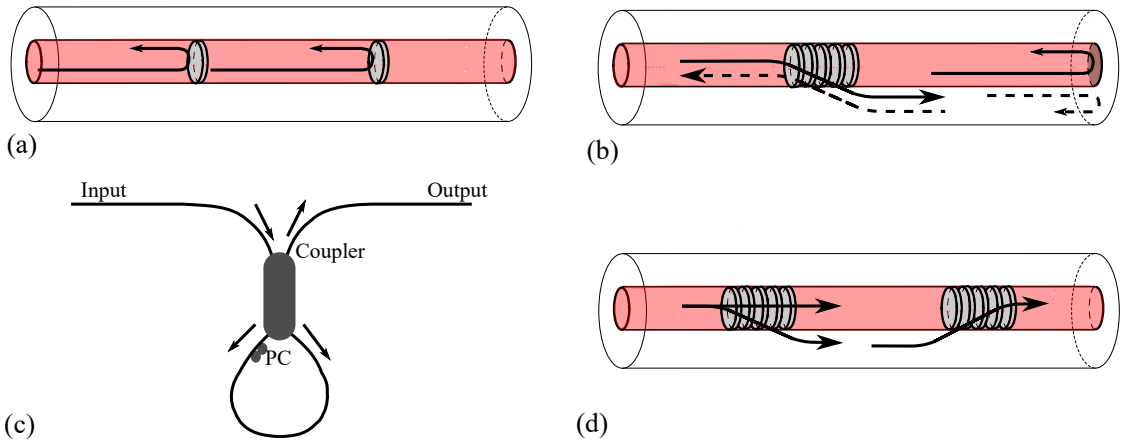

Figure 12: Types of in fiber interferometers: Fabry-Perot(a), Michelson (b), Sagnac (c) and Mach-zehnder (d).

In this example case, two linearly polarized waves $E_1 = E_{01}\cos(K_1 r - \omega t + \epsilon_1)$ and $E_2 = E_{02}\cos(K_2 r - \omega t + \epsilon_2)$ are superposed, resulting in the above irradiance[51] quantity where $\delta = k_1 r - k_2 r + \delta\phi$ is the Optical Path Difference (OPD). Eq. 45 highlights that any change in phase or optical path change cause a dip shift in irradiance spectrum. As pointed out in section 2.2 and 2.4.1, a huge amount of external factors can alterate these two parameters. This allows in fiber interferometers to harness an outstanding potential to behave as optical sensors of a wide amount of magnitudes (temperature, strain, stress, RI, bending,...) in a similar way to FBGs.

As interference pattern may be shifted by several amounts of external factors, its sensing versatility comes with an evident drawback, cross-sensitivity. In fiber, interferometers must be designed in such a way that $\Delta\delta$ is only influenced by desired parameters being insensitive to the rest. This gives rise to many trade-off decisions when new interferometric configurations are designed.

There are four main types of in fiber interferometers, namely: Fabry-Perot, Sagnac, Michelson and Mach-Zehnder [120]. These types will be briefly introduced in subsections below showing their typical OPD.

2.4.3.1 *Fabry-Perot interferometers*

Fabry-Perot Interferometer (FPI) are based in a cavity[52], where part of the fundamental mode is reflected at its boundaries. This gives rise to an interference pattern with an Optical Path Difference consisting of twice the cavity length as depicted in Fig 12 and a phase difference:

$$\delta_{FPI} = \frac{2\pi}{\lambda} n_{cavity} 2L. \tag{46}$$

Where L is the cavity length and n_{cavity} the effective refractive index of propagated mode in the cavity. This type of interferometer can be placed near the fiber end-face and there-

51 Irradiance is defined as $I = \frac{\epsilon}{\sqrt{\epsilon\mu}} < E^2 >$ where $< E^2 >$ denotes time average of electric field square $< f(t) >_T = \frac{1}{T}\int_t^{T+t} f(t')dt'$.

52 These cavities may be external as two spliced fiber connected or intrinsic, formed by two reflectors.

foreit can be easily used as probe for multiple measurements such as bending [121], temperature and strain [34].

2.4.3.2 *Sagnac Interferometers*

Sagnac Interferometers (SI) are quite unusual in the sense that one of their key features is the use of different polarization states. In this configuration, light is split trough a fiber coupler with both arms fused, resulting in a fiber loop where the split modes propagate in counter directions. A polarization controller is placed at the beginning of sensing fiber, here Optical Path Difference will be governed by birefringence:

$$\delta_{SI} = \frac{2\pi}{\lambda}\Delta n = |n_o - n_e|. \tag{47}$$

2.4.3.3 *Michelson Interferometers*

Michelson Interferometers (MIs) are based on two different paths that are reflected at their respective ends interfering at the reflection. Fig. 12.b shows how these paths consist in two modes with different effective index. Usually, the fundamental mode is partially decoupled to a cladding mode. Both modes travel to the reflector[53], then they are reflected and the cladding mode is coupled back to the fundamental mode producing the interference. In this case, path difference is

$$\delta_{MI} = \frac{2\pi}{\lambda}2\Delta nL. \tag{48}$$

Here L is the distance from the decoupler to the reflector and $\Delta n = n_{cor} - n_{cladd}$ is the effective index difference between core and cladding modes. The decoupling of core mode to cladding mode can be performed by several methods, being LPGs [120], core mismatch [122] or even inscribed beamsplitters [36] just a few remarkable examples.

2.4.3.4 *Mach-Zehnder*

Finally, Mach-Zehnder Interferometers (MZIs) are quite similar to MIs but lacking the reflector structure, requiring the cladding mode to be coupled back to the core by another structure. This causes MZIs to exhibit an interferometric transmission spectrum rather than reflexion spectrum. The OPD of MZI is usually expressed as:

$$\delta_{MZI} = \frac{2\pi}{\lambda}\Delta nL. \tag{49}$$

Decoupling of fundamental the mode can be achieved by several ways just like the MI. Here, more examples such as tapers [123, 124, 125], thin core fibers [126], MMF segments [124] can be mentioned. In addition, MZI can also use cavities where a portion of core mode travels in a different medium than fiber core [20, 127, 128]. The Free Spectral Range (FSR) of an interferometer is the chromatic distance between two successive optical irradiance maxima or minima (dip) for a given wavelength λ_0. For a MZI, its FSR will be expressed as:

$$FSR \approx \frac{\lambda_0^2}{\Delta nL}. \tag{50}$$

53 This reflector is usually placed at the fiber end-face, being this configuration quite useful for fiber-end sensing.

From equations above, it is clear that a high value of Δn implies a lower path length L, allowing cavity MZI to be more compact than common MZIs, exhibiting lengths shorter than $75\mu m$ [128]. This cavity may be in contact with the surrounding fiber medium and thus exhibiting high sensitivity to RI external medium and high value of Δn or inside the optical fiber [127] (which is a hybrid technique involving fusion splicing). As cavity is mainly produced by ablation, fs lasers are widely used for this kind of configurations. Unfortunately, they are unable to detect bending direction and the induced ablation may deteriorate the mechanical response of the device, limiting the maximum bending (before breaking the fiber) that can be reached. On the contrary, there are very few examples of MZI using LIRIC to the best of the authors' knowledge. Said phenomenon exhibits a tremendous potential for waveguide and other microphotonic devices development. There have been reports of waveguide inscription in fiber optics, but with an index change of $3.2 * 10^{-3}$ [129], having asymmetric structures not fully explored except for X-couplers [130]. This will be further discussed in section 5.2.2 where a waveguide based MZI will be manufactured.

2.4.4 OPTICAL FIBER TAPERS

A Tapered Optical Fiber (TOF) consists in an optical fiber that exhibits in some region of his entire length a diameter change produced by any post-processing process[54]. This diameter modification produces several perturbations to the guided modes that can be employed in several applications. When TOFs exhibit a reduced diameter (the most common type of taper), the taper transitions transform the local fundamental mode from a core mode in the untapered fiber to a cladding mode in the taper waist [132]. This makes them suitable for mode filtering, turning higher order modes into weakly guided modes or even completely lost through the taper. Also, TOF can be used for mode coupling or decoupling, being employed in MZI manufacture [120]. Its capability to reduce undesired stimulated Brillouin scattering, thus increasing Rayleigh scattering [133] will be employed for RFG inscription in section 5.3.2.1.

2.4.5 POST-PROCESSING OF THE END-FIBER

The majority of reviewed post processed structures are placed at an intermediate position of the fiber, however, even not so intensively studied, end-fiber also exhibits high potential as sensing element. In subsection 2.4.3 this potential was already highlighted as FPI and MI can be manufactured in the end-fiber.

There are a wide variety of reported ways that fiber end-face can be used for sensing purposes. The end-face can be mechanically modified, molding it to a spherical shape that works as a Fabry-Perot cavity [134] or tapering [135] for example. Thin film deposition is other a common method for sensing a multitude of different parameters. This can be achieved by reflective mirrors [136], porous materials, allowing to change its refractive index with different substance concentration depending on the material [137], or layers working as diffraction gratings [138].

54 Examples are heating and tapering regular-size optical fiber, the flame brushing technique, the microwave heater brushing technique, CO_2 laser irradiation [131].

The diffraction gratings are of special interest due to the versatility offered by these structures. They can be used for light couple/decouplers as spectral filters and for several sensing purposes [138]. Diffraction gratings are often manufactured by the deposition of a thin film layer, which increases its manufacturing cost and complexity [23]. There are some studies featuring diffraction grating inscription by femtosecond lasers at the end-face surface such as beam-shaping of Single Mode Fiber (SMF) [139]. However, femtosecond laser inscription at fiber end-face is still a growing field that requires several characterization studies both at end-face surface and the bulk. In addition, these studies have been limited to Single Mode Fiber (SMF), remaining Multi Mode Fiber (MMF) and more complex fibers such as Multicore Fiber (MCF) or Polymer Optical Fiber (POF) uncharacterized. Chapter 6 will be focused on filling this gap of knowledge.

2.4.6 SUMMARY

In this section, a wide amount of fiber structures have been presented. These devices are versatile, being able to perform several functions with high reliability. The potential of optical fiber leads to a wide development, producing mature technology such as FBGs or truly specialized configurations such as optical interferometers. These trend has also been highlighted in the fiber end-face, conferring an overall vision not only of fiber potential but also some insights of knowledge gaps. For example, the intrinsic mechanism of rFBGs is still a major discussion. The are many trade-off decisions involved in fiber interferometers such as length, sensitivity, mechanical resistance and the laser inscription at fiber end-face is still a growing field with several fiber types not studied.

In conclusion, the amount of previous research in the fiber sensors field is outstanding but there are still room for further research thanks to the femtosecond laser post-processing techniques.

2.5 CONCLUDING REMARKS

In this chapter, a quick revision of optical material properties has highlighted the relevance of controlling the Refractive Index (RI) and shape of the material as effective ways to reflect, split, delay, absorb even guide the light. The RI can depend on several properties such as density, stress or fictive temperature. These properties may be modified through material processing. Lasers are an interesting choice for material processing given its high spatial precision at both surface and bulk, allowing selective modifications at a reasonable cost. Among laser processing, fs lasers have proven to be of special interest in the microprocessing of optical materials. Their pulses shorter than the lattice energy transfer rate allow both micromachining (change in geometry) and structural changes (RIC) at a microscale level without significant thermal effects. These two modifications are of special interest to create sensing structures in optical fibers such as interferometers, end-fiber, and FBGs. All of them can be manufactured by fs lasers. However, there are still several ways to manufacture these configurations that have not been fully explored yet, being a growing research field.

3

OBJECTIVES

After reviewing the current state of the art performed in the previous chapter concerning fs laser processing of optical fibers, the gaps of knowledge have been spotted. Some areas require more research work to reach advanced and optimized optical sensing structures. In order to focus this work towards the completion of the identified niches of knowledge and technique, five main goals have been formulated:

1. **To establish and study characterization and simulation tools.** Simulations are useful for preliminary studies, determining the viability of a certain design or even corroborating some theoretical approaches. Characterization allows the quantification of the changed properties. The correct measurement of these properties[1] is essential for reliable simulation performance. Simulations also offer the possibility to isolate certain critical parameters and check its effect on design.

2. **To explore different setups for Type I & Type II inscription.** Effort will be focused on the study of various writing configurations to compare their different inscription. The focusing optics plays a crucial role in the final result; this may be completely different in function of the Numerical Aperture (NA) or presence of some adaptive optics. Different setups must be studied, and their result, characterized.

3. **To conceive and design new structures for sensors.** The effort put in the previous point must give rise to structures such as waveguides or gratings that can be employed in the manufacture of new sensors.

4. **To explore the potential of the end-face inscription.** Inscriptions at the end-face must be thoroughly studied in several scenarios, such as surface and bellow surface inscription. These measurements must also be performed through different types of optical fiber.

5. **To apply the inscription at the fiber end-face to design new types of sensors.** The FFP of the inscriptions can be employed as a transducer. The work performed in the previous point must allow turning the fiber end face, or even the entire fiber in a multiparameter sensor.

1 For this dissertation, index and birefringence are the primary goals. Structural changes are also good indicators of these properties changes at a quantitative level.

Part II

CONTRIBUTIONS

4

TECHNIQUES IMPLEMENTATION

The goal of this chapter is to introduce to the reader several useful tools and concepts that will be employed later in the following chapters. Here, a brief description of the typical fs laser inscription setups will be summarized. Then, two simulation methods will be presented in order to check consistency of future designed devices. After that, four characterization techniques that will help to check the properties of irradiated devices will be also presented. Finally, some applications aforementioned characterization tools and simulation techniques will be highlighted in order to show their potential utility.

4.1 EXPERIMENTAL SETUP

The processing of an optical device by laser must be carried out in a proper setup where both the sample and laser properties must be carefully controlled. When processing is mainly focused towards laser inscription, the setup can be divided into the following parts: Laser, pulse control, focusing optics, monitor system and sample control.

Laser part is the most obvious one as no setup can run without it. However, it still requires the other steps in order to effectively process the sample. This part consists in both laser and electronic controllers, some controllers allow Pulse Repetition Rate (PRR) and other parameters[1] modulation, unfortunately, they do not provide the required pulse shaping in order to reliably process optical material.

The laser output is collimated with a low divergence, this distribution prevents the pulse to achieve irradiances above the damage threshold of the material and hence, requires focusing optics to process the material. Laser pulse also exhibits fixed pulse energy that must be modulated in order to control the affected sample region.

Next section of the stage is pulse control. In this part, all the optics and electronics are designed to effectively shape the beam and set desired parameters. This step can be divided into two functions: those components that modulate pulse properties independent to transversal distribution and those that modulate transversal distribution e.g. a pulse shaper. The first category includes pulse energy, Pulse Repetition Rate and polarization control. E_p can be controlled by a shutter with modulable transmittance or by a couple of polarizers[2]. Pulse Repetition Rate can be controlled by an external trigger synchronous

1 Wavelength can be controlled due to Second Harmonic Generation (SHG) or by OPA.

2 Applying malus's law that correlates total output irradiance with the angle between the two transmission axes of the polarizers θ

$$I = I_0 \cos\theta.$$

This requires one of the polarizers to be coupled to a motorized rotation stage to adequately modify energy with precision. In addition, the working region is usually limited to a linear zone of the equation above.

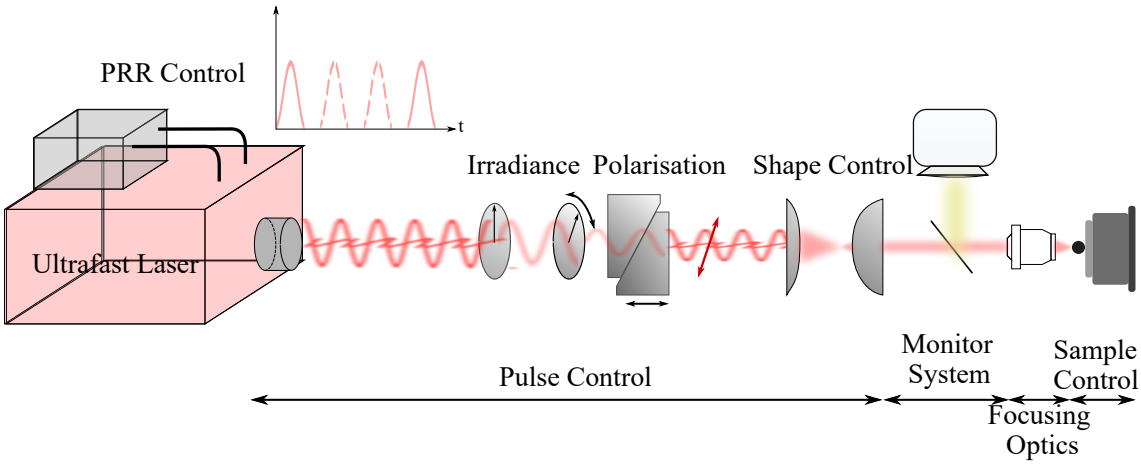

Figure 13: Diagram of a generic laser inscription setup.

to the pulse emission. In this way, PRR can be modified by blocking n consecutive pulses and transmitting one. This leads to $PRR = PRR_0/(n+1)$ where PRR_0 is the output PRR of laser system. In addition, this system can adjust PRR of different train pulses. Essentially, it is possible to deliver a sequence of several pulses at PRR_t with a frequency $\nu_t << PRR_t$. This is critical for grating inscription employing the PbP technique [94]. Polarization can be changed with the help of a compensator system to induce the desired phase difference between axes. Polarization can be important in several cases such as for nano-gratings inscription, that are formed perpendicular to the polarization direction as mentioned in section 2.3.2.6 or during the inscription of waveguides, whose properties may change as well [140].

Pulse shaping optics is usually composed by a lens system that modifies pulse propagation to best fit the processing application. In the following subsection, the disadvantages of gaussian propagation for waveguide inscription will be highlighted.

Once the pulse has acquired a proper shape, it must be focused in majority of applications[3]. This is usually achieved by a microscopic objective with a given NA. This is a key parameter that not only established the width of focal volume but also influences the damage threshold [73].

Laser processing is extremely delicate and hence it must be performed with proper care. This makes sample monitoring mandatory in order to confirm the correct operation of laser inscription. For waveguide and other inscription processes where an inscription path must be designed, monitoring is performed by imaging of the sample material[4] prior and posterior to sample acquisition.

Finally, the sample must be placed in an adequate location at the desired distance from the focal position in the appropriate conditions[5]. When performing pattern inscription, the

3 This is also the case of phase mask techniques, instead of focusing on a single point, phase mask spreads the previously expanded pulse (or beam in the case of some UV lasers) to the whole processing region but concentrated into a fringe pattern.

4 This is usually achieved by placing a beamsplitter before the light enters the objective and a CCD camera (or another imaging instrument) at the beamsplitter transmission path of the light emerging from microscopy. With this configuration, the objective not only focuses the pulse but also collects light for imaging at CCD image.

5 For example, in optical fibers, sample should be under the effect of some tensile stress and, in some cases, in an adaptive optics system to correct spherical aberrations caused by its cylindrical geometry.

focal volume must move through the sample at a given speed. This is usually achieved by placing the sample into a movable platform. It also requires a good illumination of the sample when an imaging system is implemented. For complex patterns, the movable platform requires at least three degrees of freedom with precision below the focal volume size. In some really complex patterns, more degrees are required, sample rotation can write concentric patterns easier than by just displacement though orthogonal axes. The whole setup scheme is depicted in Fig. 13 with each step highlighted.

Depending on the main direction of pattern inscription, two writing geometries can be distinguished, transversal and longitudinal inscription. Both exhibit advantages and drawbacks that will be explained in their respective subsections below.

4.1.1 TRANSVERSAL CONFIGURATION

Transversal writing refers to inscription along axes perpendicular to laser propagation direction (Fig. 14.b). This writing geometry is the most employed in optical fibers as allows wide inscription range with same inscription shape. Problems with this technique arise from the shape of emerging pulses from a lens. The minimum spot width ω_0 is limited by diffraction the following equation

$$\omega_0 = \frac{M^2\lambda}{\pi NA} \tag{51}$$

and being M^2 the Gaussian beam propagation factor. Focal volume is defined by ω_0 and Rayleigh range z_R (1/2 depth of focus)

$$z_R = \frac{\pi\omega_0^2}{\lambda}. \tag{52}$$

This makes focal volume to exhibit an ellipsoidal shape[6] (depicted in Fig. 14.a). This results in inscriptions with an asymmetric cross-section. When inscribing asymmetric waveguides, their guiding modes will exhibit elliptical cross sections that couple poorly to optical fibers [141] and losses vary in function of polarization [69]. This asymmetry may be corrected by placing additional optics before (Astigmatic Beam shaping Technique [142]) and after (Slit Beam Shaping Technique [143]) focusing optics.

4.1.2 LONGITUDINAL CONFIGURATION

Longitudinal writing geometry appears when writing direction is parallel to the beam propagation direction (Fig. 14.c). This geometry offers the advantage that waveguides exhibit circular shape[7], however, it also comes with two main drawbacks. First, the inscription is limited to the Working Distance (WD) of the lens[8] and second, as penetration depth varies while inscribing, spherical aberrations increase and hence the peak power decreases. This drastically reduces the effective WD if not corrected. In optical fibers, this writing

6 Chromatic and spherical aberrations of the microscope objective can make the equations 51 and 52 no longer valid. Spherical aberrations are easily introduced by the air-material interface. This can be solved by submerging objective in index matching liquid.

7 Actually, waveguides will be perfectly circular when $M^2 = 1$, when this is not the case, waveguides will exhibit some eccentricity.

8 For a typical NA=0.4, this yields to approximately 5mm[141].

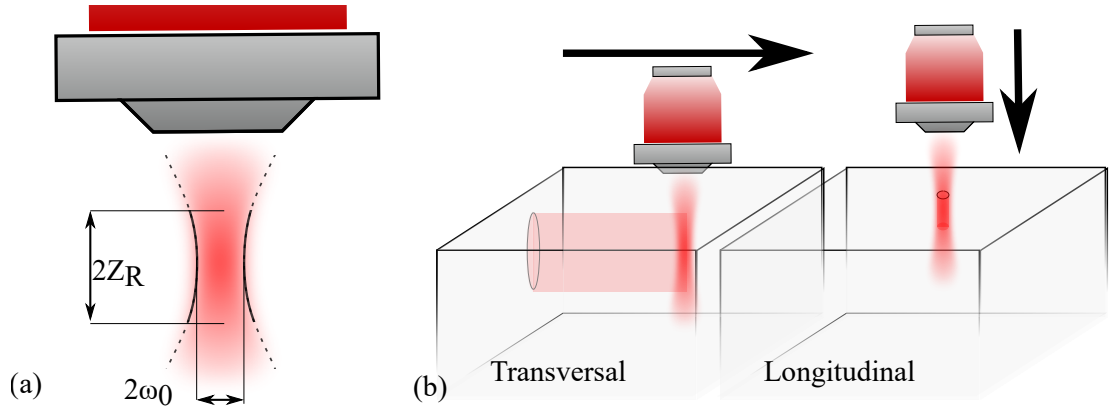

Figure 14: Focal volume (a), transversal writing (b) and longitudinal writing (c).

geometry is barely used, which is mainly caused by its shape and operation principle. This geometry can be used combined with longitudinal geometry at the bulk fiber end-face in order to inscribe 3D structures.

4.1.3 SUMMARY

In this section, the common parts of any inscription setup have been presented and explained. In this context, two types of writing geometries can be easily achieved with this setup. Both exhibit advantages and disadvantages, being the most adequate in function of desired pattern. In optical fibers, transversal writing is the most employed method. However, longitudinal inscription may be employed at the fiber end-face combined with transversal writing.

4.2 SIMULATION TOOLS

When conceiving new optical devices (e.g. optical sensors, couplers, diffractive elements, amplifying cavities, etc...), its complexity can surpass known analytical equations, requiring handy and quicker solutions to theoretically overcome the design challenges.

Simulation consists in the reduction of the desired scenario into a limited simplification with the established properties that are enough to play a role[9] in the studied phenomena. After simplifying the problem in a limited space with proper boundaries, the underlying physic is simplified through an established method. In this way, the desired phenomenon is calculated through a physic simplification that records a set of monitor parameters.

For example, to simulate propagations loses through a distance L in a SMF for several wavelengths, one can establish a two-dimensional environment (assuming radial symmetry) with a slab core of length L and a typical width (8-10µm) surrounded by an infinite cladding. Here an initial radial mode field will be launched to the core and propagated along the whole distance L to compare initial and final amplitude stored into core section. Repeating the same process at different wavelength results in a loss plot vs wavelength. This process may consume a massive quantity of computation effort when size or preci-

9 For optical materials, study parameters are mainly those already mentioned in section 2.1.1, of course, for more critical and specific simulations, another parameter must be taken into account, such as thermal and expansion coefficient, donor and acceptor density, etc...

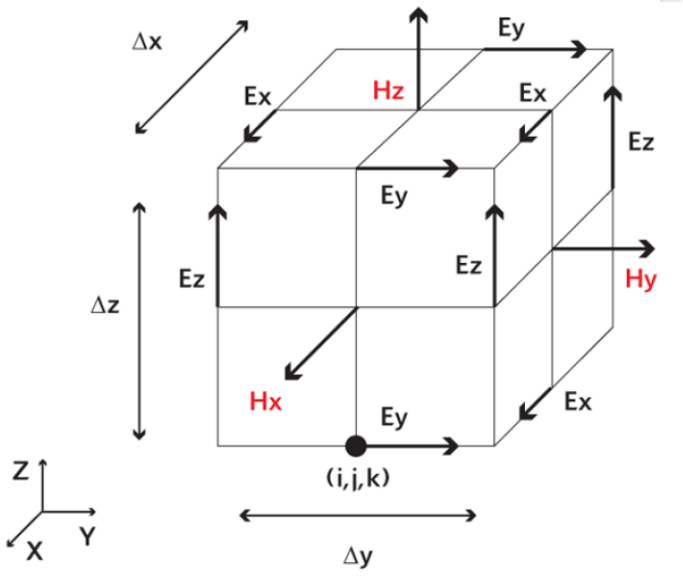

Figure 15: Cell of dimension Δx,Δy,Δz. H field is calculated at points shifted Δx,Δy,Δz/2 from E field grid points.

sion are extremely large in function to the applied simulation method. When designing a simulation domain, one must choose wisely its parameters in order to obtain a reasonable trade-off between accurate results and computation time.

While interpreting simulation results one must take into account the imposed limitations into the system. For example, if the simulation above was performed taking only into account Helmholtz wave equation, then scattering loses wont be introduced into the result. In the following subsections a few useful simulation methods will be presented at the bottom of the chapter, one practical application will be presented.

4.2.1 FINITE DIFFERENCE TIME DOMAIN

The Finite Difference Time Domain (FDTD) method is a rigorous solution to Maxwell's equations and does not have any approximations or theoretical restrictions. This method is widely used as a propagation solution technique in integrated optics, especially in situations where solutions obtained via other methods cannot meet the structure geometry or are not adequate solutions. Since FDTD is a direct solution of Maxwell's curl equations, it, therefore, includes many more effects than other approximate methods.

In a region of space which contains no flowing currents or isolated charges, Maxwell's curl equations it can be written in Cartesian coordinates as six simple scalar equations.

$$\frac{\partial H_x}{\partial t} = \frac{1}{\mu}\left(\frac{\partial E_y}{\partial z} - \frac{\partial E_z}{\partial y}\right) \quad (53) \qquad \frac{\partial E_x}{\partial t} = \frac{1}{\epsilon}\left(\frac{\partial H_z}{\partial y} - \frac{\partial H_y}{\partial z}\right) \quad (56)$$

$$\frac{\partial H_y}{\partial t} = \frac{1}{\mu}\left(\frac{\partial E_z}{\partial x} - \frac{\partial E_x}{\partial z}\right) \quad (54) \qquad \frac{\partial E_y}{\partial t} = \frac{1}{\epsilon}\left(\frac{\partial H_x}{\partial z} - \frac{\partial H_z}{\partial x}\right) \quad (57)$$

$$\frac{\partial H_z}{\partial t} = \frac{1}{\mu}\left(\frac{\partial E_x}{\partial y} - \frac{\partial E_y}{\partial x}\right) \quad (55) \qquad \frac{\partial E_z}{\partial t} = \frac{1}{\epsilon}\left(\frac{\partial H_y}{\partial x} - \frac{\partial H_x}{\partial y}\right). \quad (58)$$

Maxwell's equations describe a situation in which the temporal change in the E field is dependent upon the spatial variation of the H field, and vice versa. The FDTD method solves Maxwell's equations by first discretizing the equations via central differences in time and space, and then numerically solving these equations. This is achieved by decomposing the space into a mesh grid whose points are spaced a Δx, Δy, Δz depending on direction as depicted in Fig. 15. In this mesh, E will be calculated one-half grid spacing from H field. In addition, E field must not change significantly between neighbor grid points[10]. Time is also divided into discrete elements with increment Δt[11]. E field is measured at intervals $t = n\Delta t$ and H field at $t = (n + 1/2)\Delta t$. With the following mesh, Eqs 53-58 turn into a set of finite difference equations [144]:

$$H^{n+1/2}_{x(i,j,k)} = H^{n-1/2}_{x(i,j,k)} + \frac{\Delta t}{\mu\Delta z}(E^{n}_{y(i,j,k)} - E^{n}_{y(i,j,k-1)}) - \frac{\Delta t}{\mu\Delta y}(E^{n}_{z(i,j,k)} - E^{n}_{z(i,j-1,k)}) \quad (59)$$

$$H^{n+1/2}_{y(i,j,k)} = H^{n-1/2}_{y(i,j,k)} + \frac{\Delta t}{\mu\Delta x}(E^{n}_{z(i,j,k)} - E^{n}_{z(i-1,j,k)}) - \frac{\Delta t}{\mu\Delta z}(E^{n}_{x(i,j,k)} - E^{n}_{x(i,j,k-1)}) \quad (60)$$

$$H^{n+1/2}_{z(i,j,k)} = H^{n-1/2}_{z(i,j,k)} + \frac{\Delta t}{\mu\Delta y}(E^{n}_{x(i,j,k)} - E^{n}_{x(i,j-1,k)}) - \frac{\Delta t}{\mu\Delta x}(E^{n}_{y(i,j,k)} - E^{n}_{y(i-1,j,k)}) \quad (61)$$

$$E^{n+1}_{x(i,j,k)} = E^{n}_{x(i,j,k)} + \frac{\Delta t}{\epsilon\Delta y}(H^{n}_{z(i,j,k)} - H^{n}_{z(i,j-1,k)}) - \frac{\Delta t}{\mu\Delta z}(H^{n}_{y(i,j,k)} - H^{n}_{y(i,j,k-1)}) \quad (62)$$

$$E^{n+1}_{y(i,j,k)} = E^{n}_{y(i,j,k)} + \frac{\Delta t}{\epsilon\Delta z}(H^{n}_{x(i,j,k)} - H^{n}_{x(i,j,k-1)}) - \frac{\Delta t}{\mu\Delta x}(H^{n}_{z(i,j,k)} - H^{n}_{z(i-1,j,k)}) \quad (63)$$

$$E^{n+1}_{z(i,j,k)} = E^{n}_{z(i,j,k)} + \frac{\Delta t}{\epsilon\Delta x}(H^{n}_{y(i,j,k)} - H^{n}_{y(i-1,j,k)}) - \frac{\Delta t}{\mu\Delta y}(H^{n}_{x(i,j,k)} - H^{n}_{x(i,j-1,k)}). \quad (64)$$

Giving the proper initial conditions, this method allows vectorial electric and auxiliary field E and H calculation in the entire simulation volume at every moment of the study time interval. Now, the robustness of this method carries a major disadvantage. The consuming computational resources limit its use to small simulation domains[12]. This method can simulate optical fiber when cladding can be regarded as infinite and the study volume is not very long.

4.2.2 BEAM PROPAGATION METHOD

In those cases where long sizes must be taken into account, Beam Propagation Method (BPM) can be a reliable option as substantially reduces the computation cost. Here, the monochromatic wave equation is solved using the finite-difference approach. It starts from the well known Helmholtz equation for monochromatic waves

$$\frac{\partial^2\phi}{\partial x^2} + \frac{\partial^2\phi}{\partial y^2} + \frac{\partial^2\phi}{\partial z^2} + k(x,y,z)^2\phi = 0. \quad (65)$$

Where ϕ is the scalar amplitude of electric field $E(x,y,z,t) = \phi(x,y,z)e^{-i\omega t}$.The simulation domain will be entirely defined by specifying its RI ($k = 2\pi n/\lambda$). For this method, the

10 In general, the following rule is used to avoid unstable results: $\Delta x, \Delta y, \Delta z < \lambda/10$.

11 Similarly to space increment, the temporal stability criterion sets $\sqrt{(\Delta x)^2 + (\Delta y)^2 + (\Delta z)^2} > c\Delta t$.

12 For example, a simulation of light ($\lambda = 1.55\mu m$) propagating $100\mu m$ trough an optical fiber with cladding diameter $d_{cladd} = 125\mu m$ and applying $\Delta x, \Delta y, \Delta z = \lambda/10$ in a commercial software (thus, optimized to perform the algorithm efficiently) requires an estimated memory of 8.4 Gb and an estimate time of 5.5 days in a conventional computer.

first simplifying assumption is that field will mainly propagate along the guiding axis (usually z), other directions will exhibit slower change. This can be expressed by introducing the slowly varying field u:

$$\phi(x,y,z) = u(x,y,z)e^{-i\bar{k}z}, \tag{66}$$

$\bar{k}$ is a constant number that represents the average phase variation of the field ϕ. Applying slowly varied field, Eq. 65 becomes

$$\frac{\partial^2 u}{\partial z^2} + 2i\bar{k}\frac{\partial u}{\partial z} + \frac{\partial^2 u}{\partial y^2} + \frac{\partial^2 u}{\partial x^2} + (k^2 - \bar{k}^2)u = 0. \tag{67}$$

Now that working with a slowly varying field whose variation with z decreases sufficiently gradual with time, the first term of the equation may be neglected and hence can be finally rewritten as

$$\frac{\partial u}{\partial z} = \frac{i}{2\bar{k}}\left(\frac{\partial^2 u}{\partial x^2} + \frac{\partial^2 u}{\partial y^2} + (k^2 - \bar{k}^2)u\right), \tag{68}$$

which is the solving equation in BPM. Again, this equation will be calculated for all the grid points involved in the designated mesh similar to the one explained in the previous section (but with a single scalar value placed at grid position)[13]. The reduction of calculated values from the vectorial value of both fields for each step of time domain (in FDTD) to a single value of scalar electric field over the simulation domain implies a massive computation effort reduction. In addition, this simplification allows not only a coarser wavelength grid along z thanks to the factoring of rapid phase variations but also to be solved by simple integration of the above equation rather than iteration or an eigenvalue analysis.

Of course, the price for such simplifications is: wave must propagate primarily along z axis[14] and RI must vary smoothly along z. Fortunately, several limitations of BPM can be overcome. There are several algorithms to include more information or remove some of its limitations, such as including polarization, remove paraxiality or even handling reflections [146]. This makes BPM a strong and robust simulation method highly versatile that can be employed in many different contexts.

4.2.3 SUMMARY

In this section two simulation methods have been briefly presented, explaining its underlying principle and its strengths and weaknesses. FDTD is by far the most complete and exact simulation tool for electromagnetic phenomena calculations, however, it requires a tremendous computational effort and should be restricted to delicate complex problems

13 For the aforementioned grid, a finite-difference approach based on the Crank-Nicholson scheme can be performed. Calculating Eq. 68 for a fictitious midplane between known n plane and unknown n+1 plane

$$\frac{u_{i,j,k+1} - u_{i,j,k}}{\Delta z} = \frac{i}{2\bar{k}}\left(\frac{\delta^2}{\Delta x^2} + \frac{\delta^2}{\Delta y^2} + (k^2_{i,j,k+1/2} - \bar{k}^2)\right)\frac{u_{i,j,k+1} + u_{i,j,k}}{2}.$$

Here, δ^2 is the standard second-order difference operator $\delta^2 u_i = (u_{i+1} + u_{i-1} - 2u_i)$ and $k + 1/2 \equiv k + \Delta z/2$. This equation is solved for 2D in the following reference [145].

14 This can be a major issue when modeling bending structures, however, in section 4.4, a way to remove this restriction is presented.

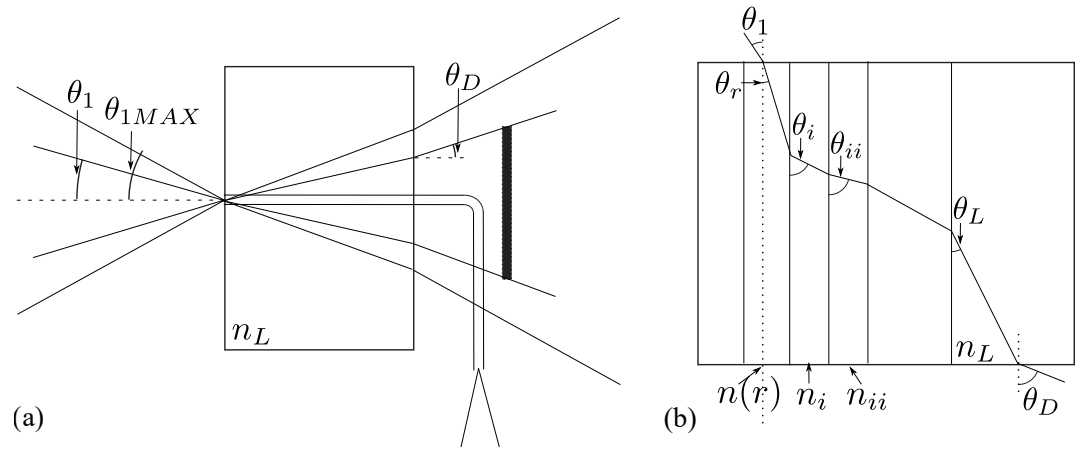

Figure 16: Schematic diagram of RNF (a), dependence of input and output angle with RI.

in a small simulation domain[15] whereas BPM, despite its limitations is a versatile simulation method that can work fine in several scenarios at a cost-effective computation effort. Both simulations will be employed through the thesis, mainly BPM due to the size of the simulation domain.

4.3 CHARACTERIZATION TOOLS

Characterization is the process or processes to highlight and measure the properties of a designated material or structure. It plays a significant role in material processing as it helps to ensure that the object has changed its properties in a quantitatively accurate way.

In fs laser processing, characterization of irradiated samples is important in order to obtain proper feedback of the optical property's modification. This information allows quality control over inscribed patterns, the correct laser parameters choice for future designs and its simulation with reliable data.

In this section five, characterization methods will be presented. Refracted Near Field (RNF) profilometry and Quantitative Phase microscopy (QPm) are two techniques to determine RI or phase (proportional to RI). De Sénarmont Compensator calculates retardance (proportional to birefringence). Micro Raman spectroscopy reveals several hints about the internal structure that can be related to several changes such as expansion or stress relief.

4.3.1 REFRACTED NEAR FIELD PROFILOMETRY

Refracted Near Field (RNF) profilometry is a tool to measure the refractive index modification of waveguides that is used in femtosecond processing, examples are [147, 148, 149]. Its underlying principle is that light focused at waveguide surface with higher NA than the later, will refract a disk containing light collected from a section of incident cone light (thus, an intensity) that depends on RI.

Here, RNF will be explained for the particular case of optical fibers but can be extrapolated to other cases. Optical fiber end-face is placed in a cell filled with an index matching liquid with RI n_L slightly higher than cladding index. Here, at the end-face surface, a

15 For example, a ring resonator.

monochromatic and Lambertian light source is focused with a lens whose NA is significantly higher than measuring optical fiber. This will produce a light cone with a hollow at the center, as the central part of the light cone is being guided by the optical fiber. An additional disk will be placed at the center of the light cone, blocking a small amount of light[16]. In Fig. 16.a the schematic diagram of these regions is depicted. θ_D is defined as the refracted angle incident at the disk circumference. This θ_D corresponds to an input angle θ_1 in such a way that between this angle and $\theta_{1MAX} = \sin^{-1}(NA_{lens})$, the refracted light is not blocked by the disk and can be captured. The relation between θ_D and θ_1 can be determined by applying the Snell's law in the scenario depicted in Fig. 16.b, from where the relations between input angle θ_1 and its refraction θ_R, the intermediate angles $\theta_R, \theta_i, \theta_{ii}, \theta_L$ and θ_D are deducted

$$\begin{aligned} \sin\theta_1 &= n(r)\sin\theta_r \\ n(r)\cos\theta_1 &= n_i\cos\theta_i = n_{ii}\cos\theta_{ii} = \cdots = n_L\cos\theta_L \\ n_L\sin\theta_L &= \sin\theta_D. \end{aligned}$$

This equations can be arranged in the following way

$$\begin{aligned} n(r)^2\left(\sin^2\theta_r + \cos^2\theta_R\right) &= \sin^2\theta_1 n_L^2\cos^2\theta_L \\ &= \sin^2\theta_1 + n_L^2 - n_L^2\sin^2\theta_L \\ n(r)^2 &= \sin^2\theta_1 + n_L^2 - \sin^2\theta_D. \end{aligned} \tag{69}$$

From this equation, it is clear that the angle θ_1 that produces the fixed angle θ_D may vary in function of $n(r)$. This angle is related to the amount of power refracted as a variation on the acceptance cone that implies a variation in the ratio of the total incident power of converging beam that is refracted and unblocked. This power variation with θ_1 is represented by [150]

$$P(\theta_1) = P(0)\left(1 - \frac{\sin^2\theta_1}{\sin^2\theta_{1MAX}}\right). \tag{70}$$

If the RI is assumed to slightly change along fiber diameter, then RI can be rewritten as $n(r) = n(0) + \delta(r)$ with $\delta(0) = 0$ and $n(0) >> \delta(r)$. With this change, the square of RI becomes

$$n^2(r) \simeq n^2(0) + 2n(0)\delta(r) = 2n(0)n(r) - n^2(0). \tag{71}$$

Using Eqs, 69 and 71 on 70, it can be obtained:

$$P(\theta_1) \simeq K_1 - K_2 n(r). \tag{72}$$

Thus, power from the refracted light cone is linearly proportional to Refractive Index (RI) of the focused surface point. With this technique, an scan over the optical fiber diameter retrieves a RI profile of the given optical fiber. This method can retrieve the index change

16 This is performed because the light near the dark cone is composed of leaky and refracted modes whose measurement is complicated.

of an inscribed waveguide by fs laser in an optical fiber when RIC is small enough[17] and the surface doesn't exhibit roughness.

This method enables reliable measurements of RIC when waveguides have been properly inscribed. In order to obtain a plain surface, the best method is to inscribe the waveguide and then cleave the fiber. The inverse method is also possible but requires inscription at low laser fluence and careful inspection of resulting inscription. Inscribing above surface could cause roughness while inscribing below the surface could create a gap of unmodified material that could modify the measurement.

This method has an important drawback, it is a destructive measure in several cases and requires the irradiated region to be constant trough z axis[18]. When Refracted Near Field profilometry is not a suitable option to measure RI, other methods must be employed.

4.3.2 QUANTITATIVE PHASE MICROSCOPY

Quantitative Phase microscopy (QPm) is a microscopy technique that allows phase measurements instead of conventional intensity captures. The key point of this technique is that no especial microscope is required because it relies on the intensity transport equation[151]:

$$k\frac{\partial \tilde{I}}{\partial z} = \nabla(\tilde{I}\nabla\Phi). \tag{73}$$

Where $\tilde{I} = I/ < I >$ being I the image intensity and $< I >$ its spatially averaged value, Φ is the phase of the image. This equation exhibits how phase can be retrieved when intensity change respects its known propagating direction. For that purpose three conventional intensity images are employed. One focused and other two defocused by an amount of $\pm\delta z$. This can be performed in a conventional well illuminated[19] transmission microscope with a step platform that can perform defocussing in an accurate way.

The selection of condenser NA is in conditioned by the microscope objective. ξ, denotes the quotient between both NAs and it has an influence on the final visibility becoming higher when $0.4 < \xi, = NA_{Condenser}/NA_{Ojective} < 0.6$. Another choice is the defocussing length, which depends on the depth of field

$$D_z = \frac{\lambda\sqrt{1 - NA^2}}{NA^2}. \tag{74}$$

Measured phase will be accurate when $\delta z/D_z < 2$ [151]. This is valid both for thin and thick (lower and higher than D_z respectively) samples. It must be pointed out, that several factors can change the phase, for example, the sample must be conveniently focused, otherwise, the measured phase will be lower. In addition, the phase is constant and accurate for thicknesses lower than the width. In section 4.4, some phase captures will be shown, comparing results with RNF profilometry.

17 This restricts Type III as its index change is significantly large.

18 This makes the technique unreliable to measure structures irradiated by pulses whose propagation direction is parallel to fiber propagation axis.

19 Eq. 73 is though for coherent sources, in practice, partially coherent sources are used as the one obtained by Kohler's illumination, which is suggested [152].

4.3.3 DE SÉNARMONT COMPENSATION TECHNIQUE

The de Sénarmont compensator couples a highly precise quarter wavelength birefringent quartz or mica crystalline plate with a 180-degree rotating analyzer to provide retardation measurements having an accuracy that approaches one thousandth of a wavelength or less. Retardation measures the phase shift that a material produces to the light transmitted, measurements can go over an optical path difference range of approximately 550 nanometers (one wavelength in the green region) for the quantitative analysis of crystals, fibers, and birefringence in living organisms, as well as investigations of optical strain. In addition, de Sénarmont compensators are useful for emphasizing contrast in weakly birefringent specimens that ordinarily are difficult to examine under crossed polarized illumination.

This technique can be implemented in several transmission microscopes, requiring a quarter wavelength plate, a monochromatic filter[20]. Also, a polarizer, an analyzer a condenser and a rotatory stage are required.

The principle behind this technique is that incoherent monochromatic light passing through linear polarizer produces linearly polarized light and when trespasses a birefringent sample whose fast axis is oriented 45° over polarizer axis[21], will become elliptically polarized. When this light passes trough a quarter wavelength plate, light will become linearly polarized light having a vibration azimuth different from that of the polarizer. By knowing this azimuth, one can calculate retardance produced by the sample at given wavelength.

This can be explained by Jones matrix formalism. When no sample is placed on the aforementioned scheme, also depicted in Fig. 17, it can be reduced to a polarizer, a quarter wavelength plate with both polarizer and fast axes on x-direction and finally an analyzer with polarizing axis in y direction. In such case the total amount of light transmitted is

$$E_0 e^{-i\omega t} e^{i\pi/4} \begin{pmatrix} 0 \\ 0 \end{pmatrix}_{final} = \begin{pmatrix} 0 & 0 \\ 0 & 1 \end{pmatrix}_{pol} e^{i\pi/4} \begin{pmatrix} 1 & 0 \\ 0 & i \end{pmatrix}_{\lambda/4} \begin{pmatrix} 1 \\ 0 \end{pmatrix}_{pol} E_0 e^{-i\omega t}, \qquad (75)$$

which is a trivial result as retarder plates do not change the polarization of incident linearly polarized light when fast axis and vibration axes are parallel and cross polarizer extinguish light[22]. Now, a birefringent sample acting as a linear retarder (circularity $\Phi = 0$), whose fast axis is placed 45° with respect to polarizer axis ($\theta = 45°$) and, for a simpler calculation, the phase of slow and fast axes can be defined as $\phi_x = \phi/2 and \phi_y = -\phi/2$ the Jones matrix becomes

20 Retarder plates are designed to produce the specified retardance in a particular wavelength, that's why illumination must exhibit the specified wavelength.

21 This can be performed employing the rotatory stage and a full wave retardation plate with white light. Retarder plate produces an exact wavelength retardation, retrieving the exact polarization state to operating wavelength (being nulled later due to the crossed polarizer) the rest of the wavelengths will become elliptically polarized and hence will be transmitted. If operating wavelength is green, then the background will be magenta due to the mix of blue and red. When a birefringent sample is placed between polarizer and retarder plate, If the specimen slow vibration axis is superimposed over the corresponding axis of the retardation plate, the additive retardation effects will result in the linearly polarization of blue wavelengths, being blocked by analyzer. However, if the fast axis of the specimen is parallel to the slow axis of the retardation plate, the relative retardation will be decreased and result in red wavelengths being blocked. In conclusion, when rotating the sample, if birefringent zones exhibit red-yellow color, then axis are parallel to those of the full wave plate.

22 As stated in Mallus's law mentioned in footnote 2.

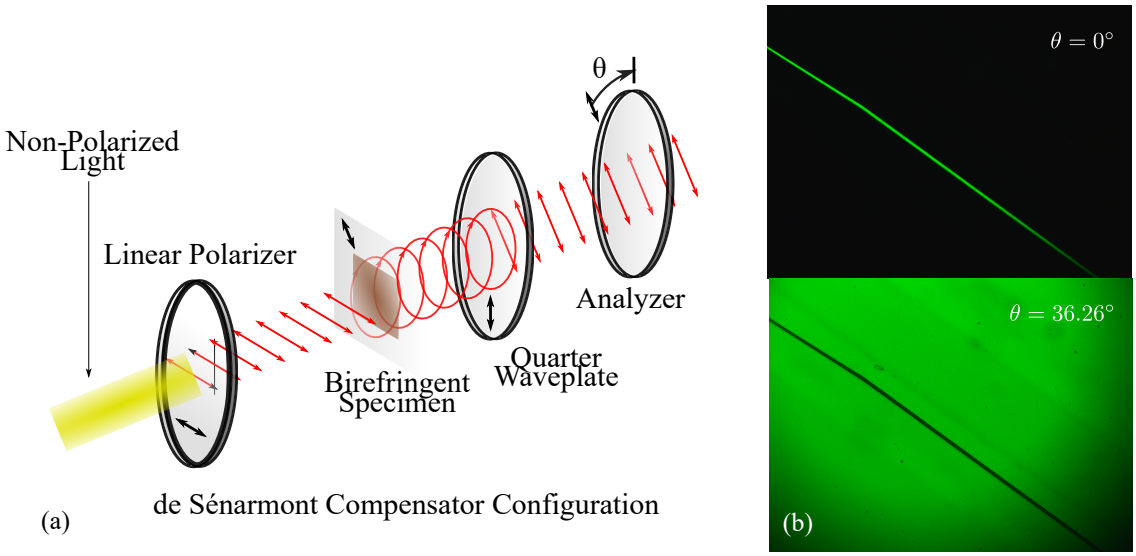

Figure 17: Schematic diagram of the de Sénarmont compensation technique (a) and images of a femtosecond laser inscription in an optical fiber when analyzer is perpendicular to polarizer $\theta = 0°$ and when is rotated $\theta = -\phi/2 = 36.26°$ (b).

$$\begin{pmatrix} e^{i\phi_x}\cos^2\theta + e^{i\phi_y}\sin^2\theta & (e^{i\phi_x} - e^{i\phi_y})\cos\theta\sin\theta e^{i\Phi} \\ (e^{i\phi_x} - e^{i\phi_y})\cos\theta\sin\theta e^{i\Phi} & e^{i\phi_x}\sin^2\theta + e^{i\phi_y}\cos^2\theta \end{pmatrix} = \begin{pmatrix} \cos\phi/2 & i\sin\phi/2 \\ i\sin\phi/2 & \cos\phi/2 \end{pmatrix}. \tag{76}$$

When the sample is introduced, then the light at the exit of the retarder plate is

$$E_0 e^{-i\omega t} e^{i\pi/4} \begin{pmatrix} \cos\phi/2 \\ -\sin\phi/2 \end{pmatrix} = \begin{pmatrix} \cos\phi/2 & i\sin\phi/2 \\ i\sin\phi/2 & \cos\phi/2 \end{pmatrix} e^{i\pi/4} \begin{pmatrix} 1 & 0 \\ 0 & i \end{pmatrix} \begin{pmatrix} 1 \\ 0 \end{pmatrix} E_0 e^{-i\omega t}. \tag{77}$$

Emerging light is linearly polarized along an axis that depends on the phase change $\phi_x - \phi_y = \phi$. If the analyzer has been rotated an angle θ, its Jones matrix will be equal to $J_{rot} = R^{-1}(\theta) * J * R(\theta)$ where $R(\theta)$ is the well-known rotation matrix. This gives (neglecting the constant term)

$$\begin{pmatrix} \sin\theta\sin(\theta + \phi/2) \\ -\cos\theta\sin(\theta + \phi/2) \end{pmatrix} = \begin{pmatrix} \sin^2\theta & -\sin\theta\cos\theta \\ -\sin\theta\cos\theta & \cos^2\theta \end{pmatrix} \begin{pmatrix} \cos\phi/2 \\ -\sin\phi/2 \end{pmatrix}. \tag{78}$$

This means that by rotating the analyzer until sample light vanishes, one can obtain half the phase change angle $\theta = -\phi/2$. This can be translated to an retardance

$$\Gamma = \lambda * \theta/180 \tag{79}$$

where the equation is in degrees as analyzer usually works on this scale.

To illustrate the operation of this technique, Fig. 17.b depicts two images of a femtosecond laser inscription in an optical fiber. As the fiber is tense (there is no bending related strain) and stress-related birefringence is low, the optical fiber can be regarded as isotropic, the only birefringent element is the fs inscription. When the analyzer is perpendicular to

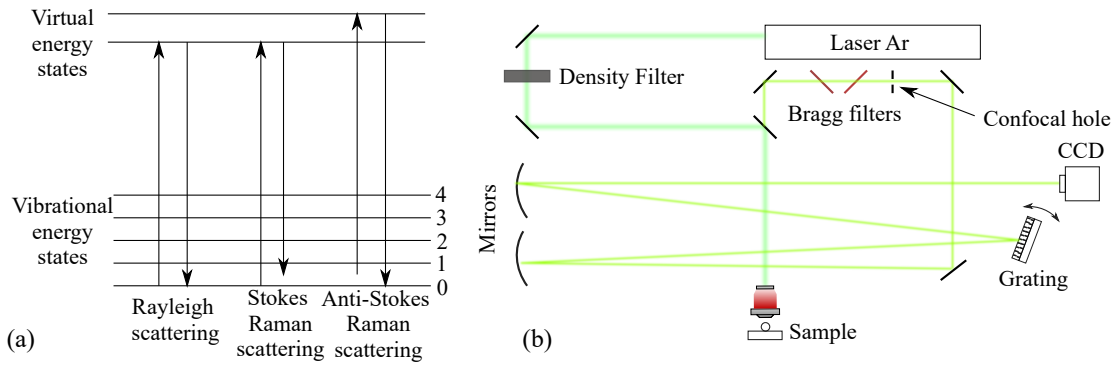

Figure 18: Schematic diagram of Rayleigh and Raman scattering (a) and schematic of a common setup for micro Raman spectroscopy (b).

the polarizer ($\theta = 0°$) the inscription is the only non-dark element, if the analyzer is rotated, the inscription will begin to fade and background will become visible again. When inscription becomes completely dark, rotation analyzer $\theta = -\phi/2$, in this case $\theta = 36.26°$ and hence the retardation is $\Gamma = 110nm$ (operating wavelength $\lambda = 546nm$).

4.3.4 MICRO RAMAN SPECTROSCOPY

Micro Raman spectroscopy is a versatile and very common laser technique that allows the atom-scale structure study of the material. It is based on inelastic scattering of photons by molecules. This molecules exhibit several excited states that corresponds to particular motions and/or vibration configurations. Those states are called vibrational states and usually implies a change in polarizability or dipole moment [11]. When a photon scatters inelastically (Raman scattering), it distorts (polarizes) the cloud of electrons around the nuclei to form a short-lived state called a *virtual state* and then quickly re-radiates the photon with a different energy, thus bringing the electrons to another vibrational state. This is depicted in Fig. 18.a, a lower energy scattered photon is called Stokes Raman Scattering and implies that some energy has been transmitted to the molecule, exhibiting a higher vibrational state, the opposite is called Anti Stokes Raman scattering. Its elastic counterpart, Rayleigh scattering is produced when the photon emitted from virtual state is the same as the absorbing photon.

Raman scattering is a weak process in that only one in every 10^6–10^8 photons which scatter is Raman scattered, however, is an interesting phenomenon as allows to track vibrational states. The number of vibrational states depends on the molecule and each represents a different vibration scheme depending on molecule structure. These vibration states can be said that behave as a "fingerprint" of the molecule.

Raman spectroscopy employs strong laser sources and complex schemes such as the one depicted in Fig. 18.b to measure the frequency shift of scattered photons and represent their spectra. When micro Raman spectroscopy is employed, laser light is tightly focused to a small region of the material with multilayered structure. Then, a movable stage translates the sample, allowing measurement of another region. This allows Raman espectra comparison and even profiling a certain wavelength shift over a distance or surface.

This method can be employed to obtain very accurate characterization as can be noticed in section 4.4 where Raman profiles for FBGs and rFBGs will be shown.

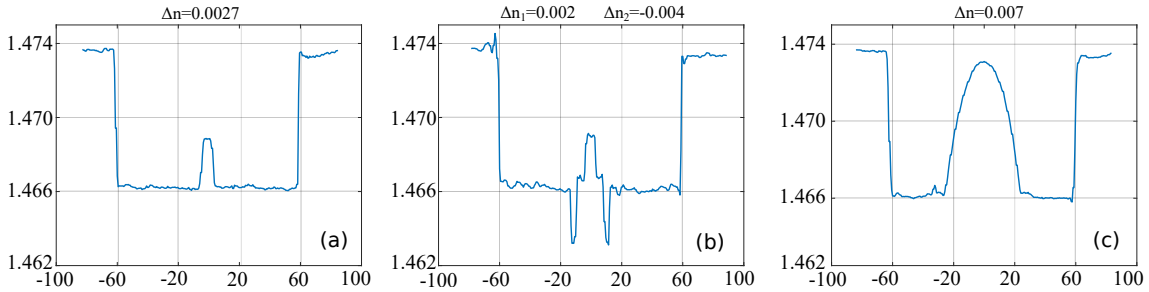

Figure 19: Different Refracted Near Field profiles: SMF28 (a), depressed cladding Single Mode Fiber (b) and Multi Mode Fiber (c).

4.4 EXAMPLE APPLICATIONS

4.4.1 TYPICAL RNF FIBER PROFILES AND COMPARISON WITH QPM CAPTURES

RNF has been performed in three different optical fibers, a standard telecom SMF28, a SMF with depressed cladding[23] (BendBright XS from Draka Comteq) and a MMF. In all cases, fibers have been stripped and carefully cleaved before placing into the cell. Measurements were performed by Sira Optical Fiber Refractive index profiler. Results are depicted in Fig. 19 exhibiting the expected results for each fiber. The index change $\Delta n = n_{core} - n_{cladding}$ has been measured by repeatedly perform the RNF profile and average, results for each fiber are $\Delta n_{smf} = 0.00270(28)$, $\Delta n_{depressed1} = 0.00240(39)$, $\Delta n_{depressed2} = -0.00370(51)$ and $\Delta n_{mmf} = 0.00760(59)$.

Now, the same SMF28 type will be measured trough QPm. First issue that must be faced is the fiber geometry, the cylindrical shape can significantly distort phase image. For that purposes, fiber must be prepared to suppress cylindrical shape effect on light propagation. This is performed by applying the sandwiching technique proposed by Zhou and Roberts [153, 154] that is depicted in Fig. 20.a. In this case, a drop of index matched liquid has been added to the slide and then two auxiliary striped SMFs[24] are placed as close as possible of either side of sample fiber without superposing with each other. This is performed in order to refrain index matching liquid to escape the sample zone and to obtain a processing zone as close to bulk as possible. Finally, a cover slip is placed above the fiber to further prevent index matching liquid from escaping and also homogenizing the surface. Now, three captures of the central SMF with a x20 objective at $\delta z = \pm 3\mu m$ have been performed resulting in the phase image depicted in Fig. 20.b. The cladding and matching liquid interface is salient, the core placed at the fiber center is brighter (implying that exhibit higher phase) surrounded by a darker region. The results shown in Fig. 19.a, does not account for such region thus, is considered a spurious phase contrast that could be caused by an inadequate condenser aperture among other causes. From this image, a profile might have been extracted similar to RNF but transversal $\phi(x, z)$ instead of radial $n(r, z)$[25] as depicted in Fig. 20.c for the position range delimited by dashed red line in Fig. 20.b. This profile is averaged along z axis in order to obtain a stable measurement, the phase

23 Depressed cladding SMFs are those that exhibit a cladding ring surrounding the core with a RI lower than the rest of the cladding. This is performed to reduce the coupling of core modes to the cladding modes when the fiber bent, thus, reducing its losses.

24 Easy to handle fragments preferable.

25 Both profiles if symmetric about its axis, can be commutable though the Abel transform[154].

change $\Delta\phi = 0.38(3) rads$ can be translated to RIC if depth is known using the well known relation

$$\Delta n = \frac{\Delta\phi\lambda}{2\pi z}. \tag{80}$$

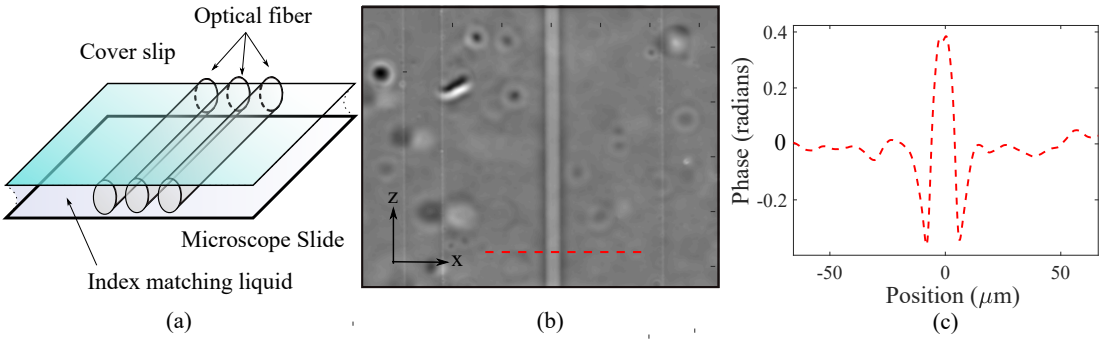

Figure 20: Scheme of adaptive optics process for removing aberrations caused by its cylindrical shape (a). Phase image of SMF (b) and its corresponding phase profile (c).

Assuming that the core distance is just the positive phase change interval ($\approx$ 10% difference compared to RNF), one gets $\Delta n = 0.00320(35)$ which is consistent with the previous measurements. QPm can offer reliable Refractive Index Change values, but a proper result interpretation is mandatory as one must attribute one phase change to a given structure with particular depth. In several cases, the RIC retrieval is so complicated that phase alone is used, which is a reliable indicator of RI distribution. In the following example only the phase will be employed to deduce the behavior of fs inscription in different species.

4.4.2 QPM AND DE SÉNARMONT COMPENSATOR MEASUREMENTS OF FEMTOSECOND LASER INSCRIPTION IN SEVERAL OPTICAL MATERIALS

Femtosecond laser inscribed waveguides are of special interest due to the several applications in integrated optics. This provokes an increasing effort to improve their quality in terms of losses and other properties. For that purposes, the optical material plays a critical role in the quality of inscribed waveguides. This leads to the search for glass materials with superior photosensitive properties. For that purpose, phase measurements of inscribed structures is an easy way to characterize the glass behavior to fs laser irradiation. These measurements give several clues of the waveguide performance.

For example purposes, two crystal families will be irradiated and its phase change will be measured. First one is the BAN[26] family, which is composed by

$$75\%SiO_2 - (12.5 - X)\%Al_2O_3 - X\%B_2O_3 - 12.5\%Na_2O \tag{81}$$

with X varying for each sample. Here, each sample has been irradiated with pulses from 0.3μJ to 4μJ. The concentration of different chemical species in the glass can significantly influence its photosensitive properties. The strength of the oxygen bonds, for example, can play a role in structure densification and defect formation [155]. In order to experimentally determine the best concentrations to produce waveguides or birefringent materials, phase

26 Boron, aluminum and sodium.

and retardance measurement have been performed for each pulse energy and concentration with QPm and de Sénarmont Compensator. In both cases, a measuring methodology is mandatory to obtain reliable results, this involves obviously same imaging parameters (NA, defocusing, etc...). Particularly, focus can become tricky as power increases because the inscription becomes longer and more complex, allowing focusing at several levels. For this methodology, all the samples have been measured at the same level, corresponding with the first focusing structure (the first contrast change detected while you bring the sample closer to the objective) as noted in Fig. 21.a.

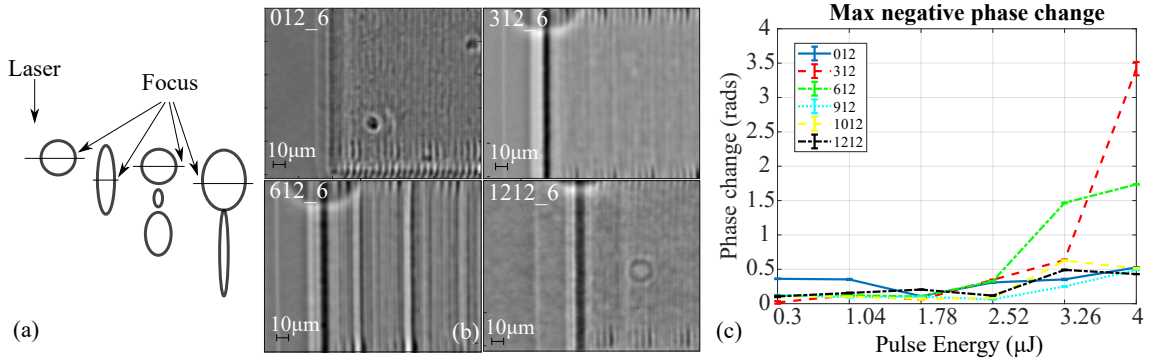

Figure 21: Scheme of QPm focus methodology (a), QPm images of different BAN samples irradiated at 4µJ (b), phase change of BAN samples with pulse energy (c).

In Fig. 21.b, phase images of same irradiation parameters ($E_p = 4\mu J$) at different concentrations X=0,3,6,12 are depicted. It can be noticed that intermediate concentrations produce stronger phase changes than Aluminum or Boron alone. This can be better observed in Fig. 21.c where the phase change of all concentrations is plotted against the pulse energy (E_p). Phase change is approximately constant between concentrations at low pulse energies, however, it is clear that when 3% Boron is included, the inscription exhibits a really high negative phase change at strong pulses energies. This makes the later a good candidate for Type III waveguides as the amount of elastic strain produced at the vicinity of the inscription becomes higher with the expansion produced.

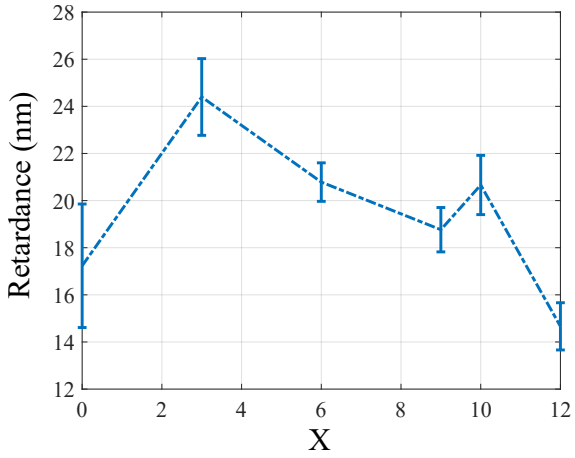

Figure 22: Retardance of different X values for $E_p = \mu J$.

Retardance is only significant for high pulse energies, being difficult to measure for lower energies. Values are depicted in Fig. 22 where a maximum retardance of 24nm has been

achieved, which is actually weak and related to stress effects, not being a suitable option to manufacture birefringent devices (for given parameters). In addition, stress birefringence can also be employed to manufacture birefringent waveguides which are attractive for several applications that require preserving polarization [13]. For these purposes, Rare Earth (RE) co-doped elements have drawn attention due to their strong stress-induced birefringence when irradiated by fs lasers. There are several reports of stress-induced birefringence in RE materials such as Nd:YAG [156, 157], $LiNbO_3$ [158, 159] and $Nd^{3+} : GdVO_4$ [160]. This makes SrF_2 crystal of special interest as is a multifunctional optical host material[27] for RE ions and could be widely disseminated in many fields. However, the concentration is limited by quenching [162, 163]. This may be overcome by the co-doping of buffer ions (e.g., yttrium (Y) and lutetium (Lu)) into RE-doped alkali crystals to minimize the concentration quenching effect and progressively improve its material properties.

For this reason, a transparent sample of $NdY : SrF_2$ with 0.5 mol% Nd and 5 mol % Y has been irradiated at two different PRR (10kHz and 500kHz) to characterize its optical properties. The inscription was performed with an ultrafast laser (Satsuma, Amplitude Systems Ltd.) that operates at 1030nm with a linearly polarized beam and delivers pulses of 250 fs with a varying repetition rate from 10 to 500kHz. Then, a 20x aspheric lens with a numerical aperture (NA) of 0.6 was customized to focus the laser beam at about 150 µm below the front face of $NdY : SrF_2$ crystal plates. Lines were inscribed at ws=0.2mm/s with pulse energy ranging from 0.1-5µJ, being the orientation of the laser polarization perpendicular to the scanning direction.

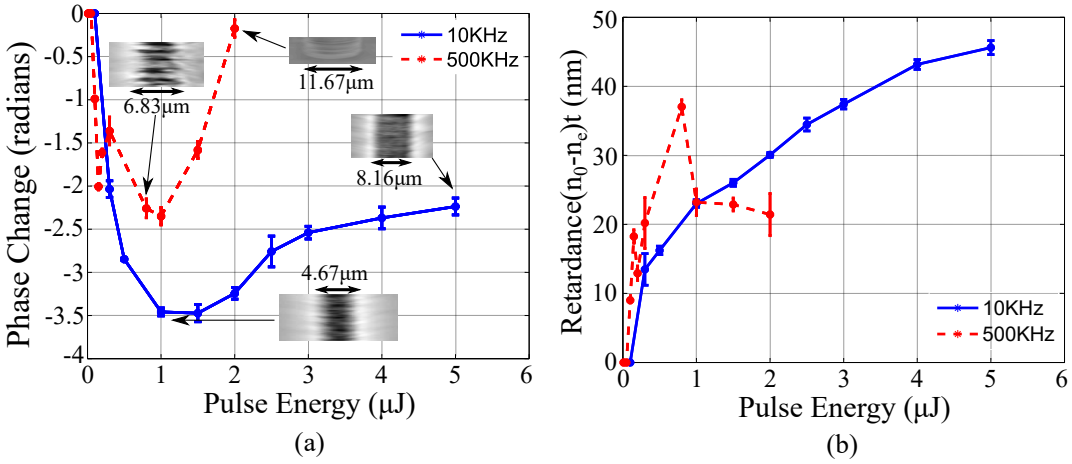

Figure 23: Phase change ($\Delta\phi$) of the laser-written track as per pulse energies according to the repetition rates (10 and 500 kHz) and associated QPM images of the $NdY : SrF_2$ crystal (a). Retardance measurements performed by de Sénarmont compensator of fs inscribed lines in $NdY : SrF_2$ with different PRR and E_p (b).

The phase results are depicted in Fig. 23.a where a particularly different behavior between PRRs can be noticed. For a low PRR (10 kHz), uniform modifications with the absence of voids formation are observed. Contrary to a low PRR, a high value (500 kHz) clearly reveals an inhomogeneous RI due to void formation in inscribed lines as the pulse energy increases above 0.6µJ. Negative phase change in both cases is attributed to volume expansion. It was found that the lines' diameter (black color) follows obvious increment with

27 Thanks to its low phonon energy, high RE solubility, low non-radiative transition probability, long lifetime metastable state, and good transparency spanning up to 11 µm from 0.2 µm [161].

pulse energies. In addition, there are some microscopic disruptions, especially at high PRR, where voids formation or inhomogeneity occurred. The white lines, as mentioned early, represent features of elastic strain occurring in and out of the laser-exposed region as a result of the permanent strain, photo induced within the irradiated area.

From a quantitative view of $\Delta\phi$ evolution with pulse energy one can see that at first, there is no change in the amplitude of phase change (kinetic behavior) until a pulse energy of 0.3µJ. For a low PRR, an increase in the negative phase change is observed until a pulse energy of 1.5µJ is reached down to -3.5 radians[28]. Thereafter, the RI is slightly increased, and it stabilizes at approximately -2.5 radians, whereas the diameter of the waveguides exhibits a monotonous increase from 4.67 to 8.16µm. On the other hand, a similar kinetic behavior could be observed at a high PRR (500 kHz) up to 1.0µJ, and then the phase change dramatically approaches an almost zero phase shift as the pulse energy typically reached 2.0µJ, where catastrophic damage can be observed. This clearly discloses heat accumulation processes in agreement with a width increase that reaches 12µm at 2µJ.

Taking a look on retardance measurements depicted in Fig. 23.b, one can see an even more different trending regarding PRR. At low values, the retardance monotonically increases with pulse energy to reach a maximum retardance of approximately 46 nm for a pulse energy of 5µJ. In contrast, high PRR inscriptions exhibit a growing retardance approaching a maximum value of 40 nm, followed by a significant decrease beyond a pulse energy of 1µJ. Above 2 µJ, the laser tracks were too damaged to probe the photo-induced optical properties due to the heat accumulation phenomenon for 500 kHz PRR waveguides. The lowering in the magnitude of the retardance could likely be attributed to the onset of appearance of the heat accumulation process. This leads to a temperature buildup around the melting temperature, which partly or completely relaxes the stress-induced birefringence occurring within written laser tracks [164].

Heat effects are also of particular interest for waveguide inscription. Given all information obtained, waveguides were written at both PRR. Waveguides inscribed at 10kHz exhibited lower propagation losses at 1µJ which coincides with the higher phase change measured. However, propagation losses at 500kHz are lower despite exhibiting lower phase change due to bleaching of point defects and scattering losses reduction due to heat accumulation [159, 157]. However, waveguides were obtained only for a pulse energy range from 0.1 to 0.3µJ which is in the energy range prior to void formation.

4.4.3 MICRO RAMAN SPECTROSCOPY IN REGENERATED FIBER BRAGG GRATINGS

The lattice of SiO_2 is depicted in Fig. 24.a, silica is arranged in a tetrahedral network where each silica atom shares an electron by a covalent bond[29] with four oxygen. This later exhibit two covalent bonds with silica atoms, arranging this tetrahedral structures in ringlike lattices. This lattice can be simplified into a 2D perspective as in Fig.24.a where, for Crystalline structures, rings have the same shape and six Si-O segments. However, when SiO_2 exhibits an amorphous structure, the shape is irregular and the number n of Si-O segments ranges from three to nine being five and six the most common number of segments. When performing Raman spectroscopy to fused silica, the result consists on a number of (often overlapping) bands that can be assigned to vibrations of different types of bonds in the glass network as depicted in Fig. 24.b where a gaussian decomposition is

28 Employing Eq 80 with known depth of 50µm a RIC $\Delta n = -6 * 10^{-3}$ is achieved.

29 This bond consists in sharing electrons in order to fill its respective last layer.

performed to decouple band information from the spectra. Here, there are two noticeable bands at $\Delta\nu = 495cm^{-1}$ and $\Delta\nu = 605cm^{-1}$ which correspond to the Raman active symmetric breathing modes of the oxygen atoms in the n=4,3 membered ring structures and are called D_1 and D_2 bands respectively [165].

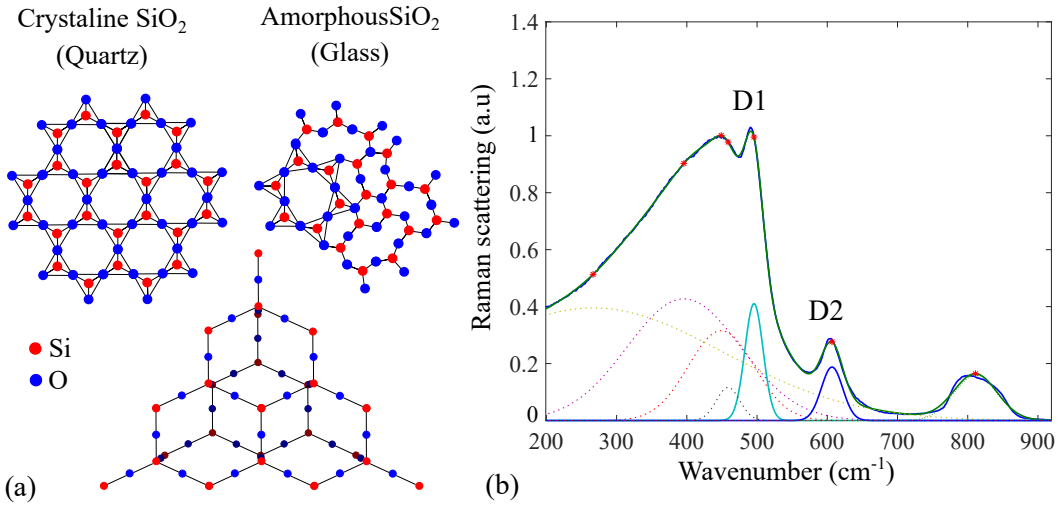

Figure 24: Lattice comparison of Crystaline SiO_2 (Quartz) and amorphous SiO_2 (glass) (a). Raman spectra of amorphous SiO_2 (b).

The value of this two bands correspond to some stored energy per volume unit that increases as glass density increases when there is no other structure modification, thus, they are reliable estimators of densification/expansion [166] and potentially stress relaxation [167, 166].

In section 2.4.1.1, the increasing need for the local structural relaxation study of multimaterial systems in regeneration process was already mentioned. This can be performed by studing D_1 and D_2 profiles.

In this study, four fiber samples were studied: a pristine fiber, a seed FBG fiber, its regenerated counterpart and a pristine fiber with the same thermal process than regenerated fiber (see Fig. 25.a). The selected fiber was a B-codoped germanosilicate GF1 that exhibits 3 layers, core, inner cladding and cladding as depicted in Fig. 25.b.

Fiber Bragg Gratings were produced by direct writing through a 10 mm long optical phase mask using an ArF laser (λ = 193nm ; pulse fluence f_{pulse} = 95 mJ/cm^2; cumulative fluence f_{cum} = 113 J/cm^2 ; PRR = 30 Hz; pulse duration τ = 15 ns). Before grating writing, the fibers were hydrogen (H_2) loaded (T = 80°C, P = 180 bar, t = 4 days). To perform the regeneration process some gratings were placed in a computer-controlled oven. The temperature was risen to T = 850 °C over t = 60 min before keeping this temperature for t = 40 min; during this dwell time the grating decays and regenerates. Subsequently, the cross-section of the samples were analyzed at the cleaved end facet of the sample (depicted in Fig. 25.b) using micro-Raman spectroscopy (Renishaw, inVia spectrometer) with an excitation wavelength of λ = 532 nm and a x100 objective (NA = 0.9) with high confocal[30].

The profiles of D_2 and the ratio D_1/D_2 are depicted in Fig. 26. As already mentioned, D_2 increment implies a density increment. The ratio, however, D1/D2, increases with

30 High confocal is important to spatially filter pump light than has been guided in the fiber and then scattered as could led to distort measurements.

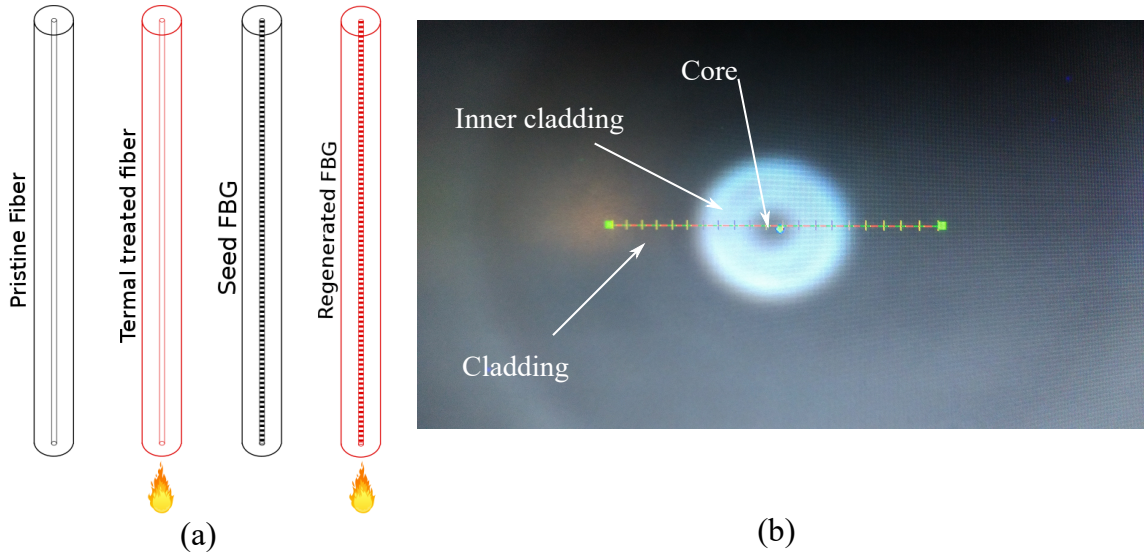

Figure 25: Samples studied by Raman spectroscopy (a). Different layers of GF1 fiber (b).

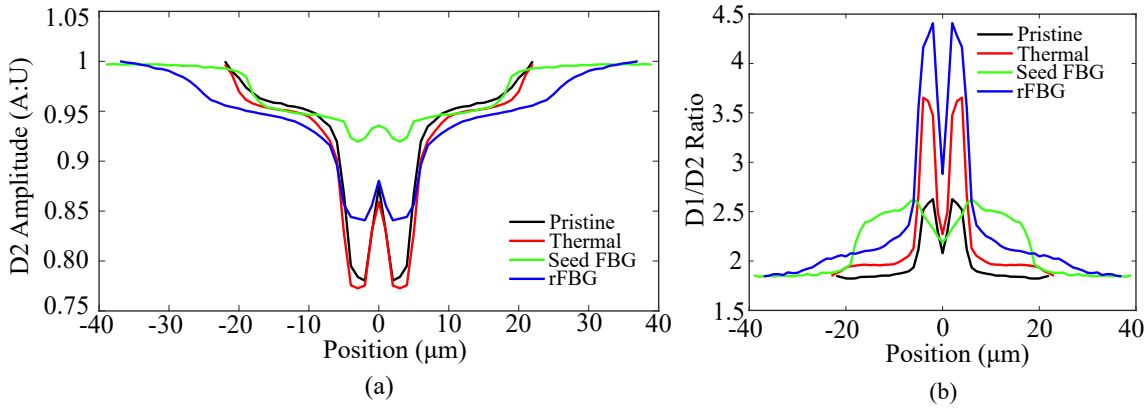

Figure 26: D_2 amplitude profile of studied samples (a) and the D_1/D_2 ratio (b).

decreasing density. As Figure 26.a shows, minor changes for D2 were observed in the core when comparing the pristine fiber and the thermally treated one. Examining the D1/D2 amplitude ratio shown in Fig. 26.b, one can see a spectacular increase everywhere of the ratio revealing a structural relaxation characterized by a decrease in glass density (expansion has occurred). Taking a look on the seed FBG and the pristine fiber, there is an increase for both D peaks in the fiber core and a slight decrease of the D1/D2 ratio, which reflects the expected UV-induced densification. In contrast, the signature of glass expansion is observed within the inner cladding of the seed UV FBG. After regeneration, both D peaks are observed to strongly decrease in height (and in the area as well) when compared to the seed FBG. In addition, there is an increase of the D1/D2 ratio in the fiber center after regeneration, increasing expansion and diameter (especially inner cladding) increase evidence.

From these expansion indicators and taking into account that with regeneration an overall relaxation at fiber core-cladding interface is expected [104], there is a consistency with the model of regeneration being largely driven by the relaxation of dominant tensile stresses through thermal annealing. As thermally treated fiber exhibits different glass relaxation rate than regenerated, the formation of different relaxation rates along the formers

seed fringes is suggested. This helps to conceive a rFBG as an imprinted spatial modulation of the glass fictive temperature $T_f(z)$.

4.4.4 EXAMPLE OF BEAM PROPAGATION METHOD APPLIED TO A BENT REFRACTOMETER

The importance of RI in optical materials has already been pointed out. However, additional information can be extracted from this property. For example, RI in liquids can be correlated to the concentration of a dissolution. An easy way to measure RI is by measuring the propagation losses of an optical fiber submerged in that RI. Optical fibers are designed in a way that minimizes this kind of losses due to surrounded media (by surrounding core with a relatively thick cladding), however, when bending is applied, there is a significant coupling to the cladding modes where some of them escape the fiber and other are coupled back to the core. This is more critical in MMF with large cores. Propagation losses in bent fibers are categorized into transition losses and pure losses. They were analyzed theoretically and experimentally by Gambling et al., who also observed in step-index multimode fibers the effects described for a single mode fiber [168, 169]. Subsequent work by Badar et al., confirmed the same results in multimode fibers [170]. As regards the curvature losses, the transition losses are more important than the pure losses, particularly when the radius of curvature is small. The former increase rapidly from the beginning of the curvature before tending to stabilize, while the latter exhibits a continuous increase [169].

For these reasons, it is interesting to exploit the transition region of a bent fiber to design a refractometer. POFs are ideal for this purpose as they exhibit large core diameters and fracture strength to bending, allowing high curvature exposition without breaking[31]. Cladding in the transition region can also be removed through a lateral polishing and simulate how this new geometry affects the loss performance.

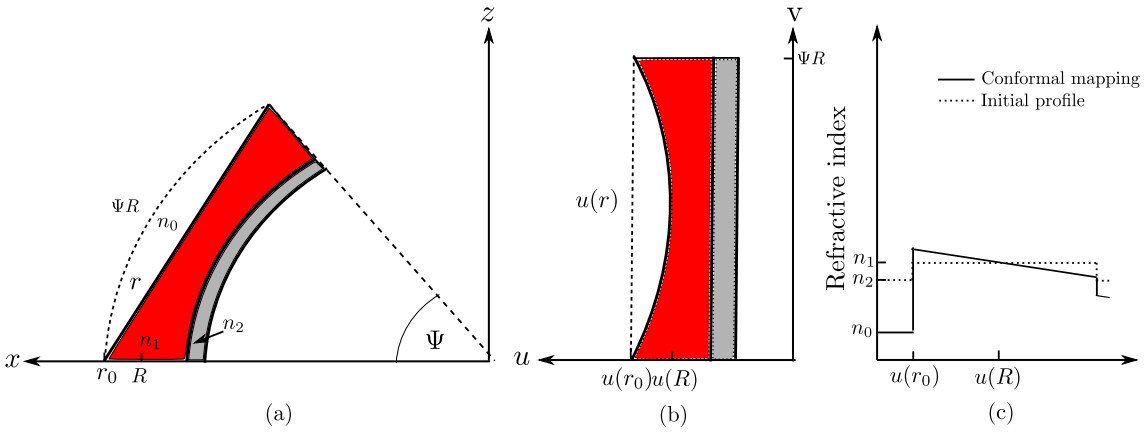

Figure 27: Application of conformal mapping to the simulation region. The bent fiber region in (a) suffers a coordinate transform W=u+iv=f(Z) resulting in (b) with a tilt in refractive index (c).

The polishing can be parametrized as a straight line intersecting two points in circumference with an angular separation of Ψ as explained in Fig. 27.a, this line, can be parametrized in polar coordinates as

31 Glass fibers are notable weak to high curvature bending, this weakness is further increased when exhibiting some microfracture as it becomes the starting point of a brittle fracture.

$$r = r_0 \frac{\tan((\pi - \Psi)/2)}{\cos\theta(\tan\theta + \tan((\pi - \Psi)/2))}. \tag{82}$$

For that reason, BPM can be used to simulate losses at the end of the fiber arc. However, as already stated, BPM is optimized for propagation mainly at z direction. When fiber is bent, BPM can not represent accurately the beam direction change. This can be solved applying a coordinate transform called conformal mapping[171, 172] that turns bend geometry into a straight element (Fig. 27.b) with a tilt RI profile as suggested in Fig. 27.c. and represented by the following equation

$$n_{bend} \approx n(x)\left(1 + \frac{x}{R}\right). \tag{83}$$

For a length $L = \Psi R$ (R=4mm, $\Psi = 40°$) and transforming Eq. 82 , losses were calculated by BPM for both side polished and conventional fibers with diameters d=0.5,1,2mm in the RI range 1.332-1.374. Results depicted in Fig 28.a suggest that for diameters above 1mm, lateral polishing reduces optical losses while keeping sensitivity constant. When the diameter is below 0.5mm, lateral polish fiber exhibits higher sensitivity. Now, the d=2mm lateral polished POF can be compared with experimental results of that same fiber at same parameters submerged in water at different concentrations of NaCl at 22°C and $\lambda = 632.8nm$ (depicted in Fig. 28.b). There is a maximum 0.14dB of loss deviation, and the simulated sensitivity is 12.12dB/RI while experimental sensibility is 16.01dB/RI which is fairly good and support evidence of the good sensor sensitivity given its simplicity and compactness.

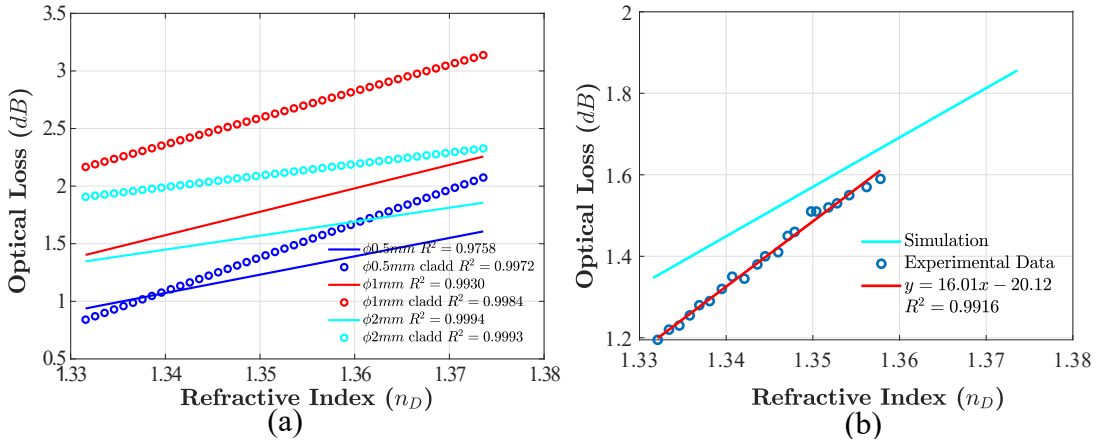

Figure 28: Comparison of bend losses for lateral polishing and conventional (cladd) fibers at diameters d=0.5,1,2mm (a). Optical loses for the d=2mm lateral polished bend POF submerged in water at different concentrations of NaCl at 22°C and $\lambda = 632.8nm$ (b).

4.4.5 SUMMARY

In this section, some practical examples of aforementioned techniques have been presented. Both RNF and QPm have been shown to reliably characterize the RI of optical fiber with their particular flaws and advantages, being the most suitable technique depending on the scenario. In addition, QPm and de Sénarmont compensator have been used for sample characterization of different irradiated samples providing useful information about the

strain, void formation and heat effects that can help in the optimal parameters choice for waveguide writing.

When these changes are discrete, Raman can give some hints of structural lattice material which can be used for tracking material changes suffered by processing techniques such as annealing.

Finally, when comes to device design, BPM has been proved to be a reliable tool to predict (when specified approximations remain valid) the behavior of different features and see how affect to the overall performance of the conceived device.

4.5 CONCLUDING REMARKS

A global vision of inscription setups has been performed, dividing the components involved in several stages for an easier understanding. The two more used writing geometries have been explained, addressing both advantages and disadvantages.

The simulation methods have proved its capability to reduce an actual problem to a set of given parameters and reproduce consistent results. The Beam Propagation Method is a flexible tool that can address several scenarios without consuming excessive resources.

Four different characterization techniques have been presented and its role in fs laser processing has been discussed. Two of them (Refracted Near Field profilometry and Quantitative Phase microscopy) are useful tools for RI characterization that complements each other. The de Sénarmont compensator is a simple tool to measure the optical retardation of birefringent samples. Their measurements allow the distinction between stress-related birefringence and the form birefringence of the induced nanogratings. The structure composition can be studied through micro Raman spectroscopy. With this technique, some conclusions about the role of expansion and relaxation of the optical fiber have been discussed.

5

IN FIBER INSCRIPTION

The later chapters introduced several tools and concepts essential to the study described in the rest of this dissertation. The primary goal of this chapter is the study of fs inscription in fiber. This work will start from simple inscriptions made to the fiber and their characterization that will conclude in their application to manufacturing new structures. The chapter comprehends two inscription methods: direct inscription and inscription using adaptive optics. The first method exhibits a cylindrical lens effect caused by the geometry of the fiber while in the latter the effect is negligible. Both methods produce different structures addressed in their respective sections.

The first section will cover the inscription setup employed to write in the optical fiber. In the second section, the direct exposition method will be analyzed, performing a waveguide characterization that will be applied to MZI manufacturing. This interferometer will be temperature and curvature characterized and implemented in a TOF for enhanced RI sensitivity. Moving to the third section, a similar structure, but employing an adaptive optics setup to remove problems during focusing produced by cylindrical lens effect. Here the characterization process will lead to grating inscription along the fiber core, manufacturing Fiber Bragg Gratings (FBGs) and Random Fiber Gratings (RFGs) employing this later in a single cavity fiber laser. The concluding remarks will be stated in the last section, closing the entire chapter.

5.1 SETUP

A transversal setup has been chosen for in-fiber inscription over a longitudinal configuration as several patterns exhibit a main writing direction along the fiber rather than perpendicular to the fiber. The Setup covers the points marked in section 4.1. The laser employed in the setup is a commercial Fiber Laser Chriped Pulse Amplifier (FLCPA) from CALMAR lasers operating at 1030nm, 370fs pulse duration and a maximum pulse energy $E_p = 0.01 - 4.93\mu J$. Laser beam falls upon a beamsplitter 90/10 reflecting the beam to an x100 microscope objective with NA=0.5. This objective is focused on a sample holder placed above a nano-resolution movable platform. White light LEDs illuminate the holder in order to monitor the sample with a CCD camera placed at the transmission line of the beamsplitter. Fig 29 depicts the scheme of the setup mentioned above.

Prepared fiber samples are placed above microscope slides. These fibers were prepared by stripping the jacket with a fiber optic stripper and then removing remaining material or dust particles with a lens cleaning film and ethanol. Once stripped and cleaned, the fiber has been fixed to the microscope slide with a Kapton film. It is essential to apply tensile strain along fiber optic before fixing the fiber to the slide to avoid micro arc bending as

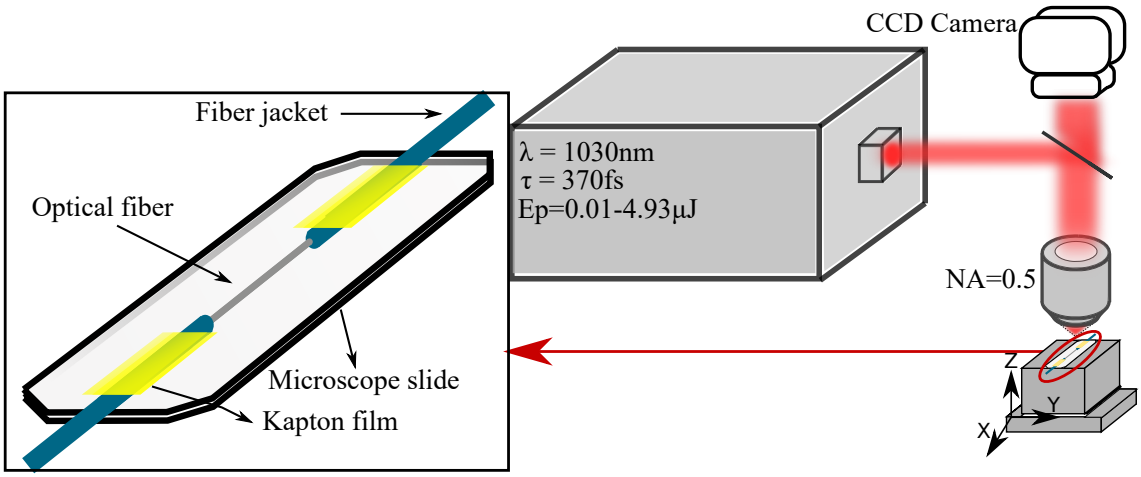

Figure 29: Scheme of the setup employed for in-fiber inscription. The fiber sample is stripped and placed above a microscope slide attached with kapton film..

much as possible. These undesired bendings make the inscribing process more challenging because the writing trajectory cannot be approximated by a straight line and without the tensile strain, the fiber may move within the holder as the platform is under movement.

The sample can be processed in its current state; however, it will suffer from spherical aberrations due to fiber cylindrical geometry. Even with spherical aberrations one can achieve robust structures, as it can be noticed in the following examples. This effect can be neglected by applying the same procedure employed for QPm characterization of optical fibers explained in section 4.4.1.

5.2 INSCRIPTION WITHOUT ADAPTIVE OPTICS

The first experiments will be carried out without employing adaptive optics. The reason is that, despite the drawbacks above, cylindrical geometry produces a loss of focus and an optical lens effect that should be briefly characterized. Said effect is depicted in Fig. 30, here a NA=0.5 with Working Distance (WD) of 12 mm is focusing monochromatic light $\lambda = 1033nm$ to a plate and a cylindrical fused silica sample at different positions. When the plate is placed $30\mu m$ above WD (Fig. 30.a), the higher RI of the sample reduces the half angle and consequently, is focused below the working distance[1]. If the plate sample is substituted by a cylindrical lens (Fig. 30.b), the amount of spherical aberrations and the focusing distance of the transversal axis is reduced. There is one particular case where the lens focuses inside the cylinder at the same position as in air: when the WD matches the cylinder radio as depicted in Fig. 30.c. This result can be deducted from Snell's law (Eq. 2), all the incident lines are perpendicular to the lens surface, preventing them from experiencing a propagation shift that produces the new focusing spot.

When working with planar samples, the focusing spot will exhibit a circular shape as depicted in Fig. 30.d as has been mentioned in section 4.1.2. However, in a cylindrical lens, as light focuses differently between axes, the spot is significantly reduced in the

1 In paraxial approximation, the focus change when a sample with different RI is placed a length d above the focal point is $d * n_2/n_1$. When the aperture angle is higher than 23°, this value deviates 5%.

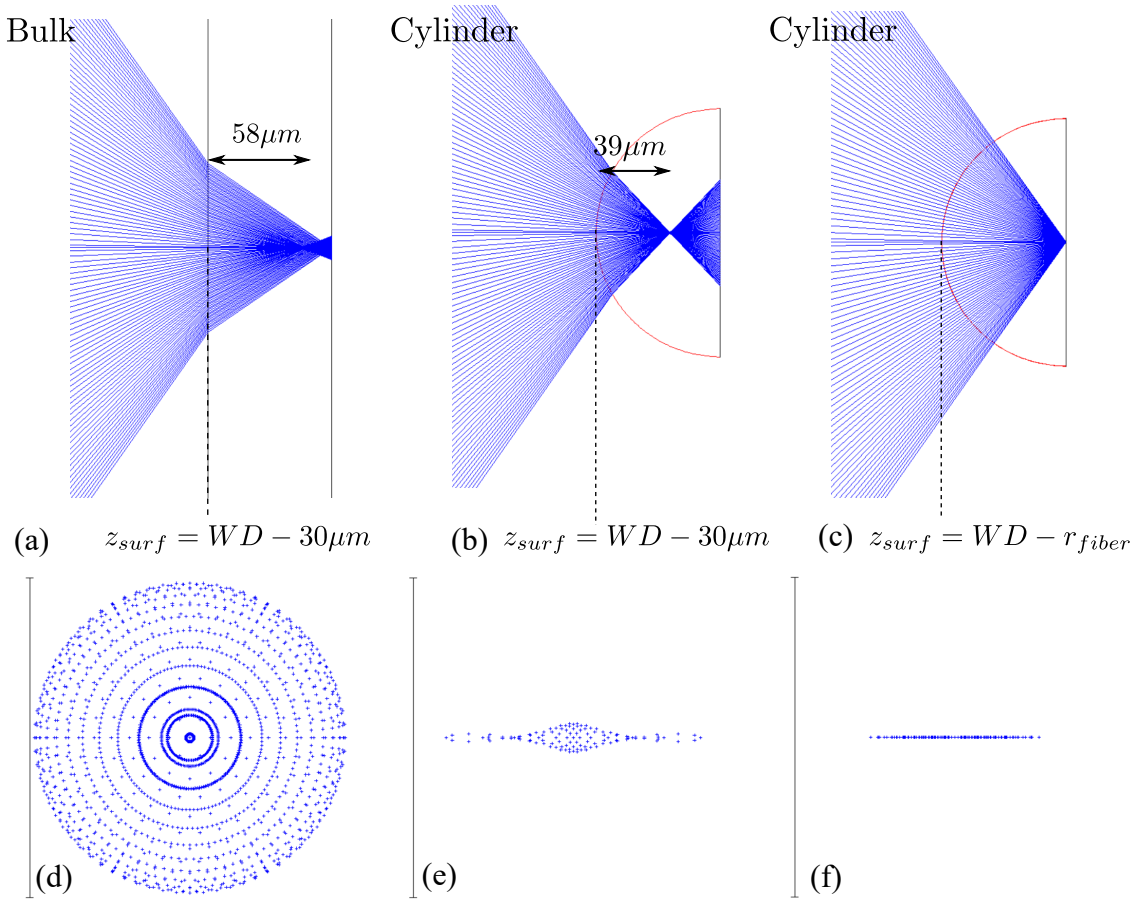

Figure 30: Ray trace of a NA=0.5 microscope lens focused in: a bulk object of RI=1.45 30µm above working distance (a), a cylindrical object of same RI placed at same position in the plane perpendicular to cylinder length axis (b), the same case when the cylinder center is placed at WD. (d), (e) and (f) are cross section of focal volume of (a), (b) and (c) respectively.

transversal direction (Fig. 30.e and f). The optical fibers also exhibit this effect that could lead to different modifications as the focal volume significantly changes. In this section, the potential of the structures performed by this particular focal volume will be studied.

5.2.1 WAVEGUIDE INSCRIPTION

In order to determine the best parameters to produce waveguides, some preliminary experiments will be performed. First one will consist in 300µm length lines inscribed at the end of an optical fiber with ws=0.1mm/s and PRR=120kHz fixed and different pulse energies (E_p). Here, exploiting optical fiber properties, one can determine without using QPm or RNF the sign of the LIRIC. By illuminating the opposite side of the optical fiber, if there is a positive LIRIC irradiated region should be brighter as the light from the core will be guided to the higher RI. However, if the focal volume exhibits negative RIC, their guiding properties will deteriorate favoring the appearance of dark spots.

Employing this method in a range $E_P = 0.47 - 1.66\mu J$ no positive LIRIC at focal volume has been observed. Fig. 31 shows three examples of those lines. It is noteworthy that the

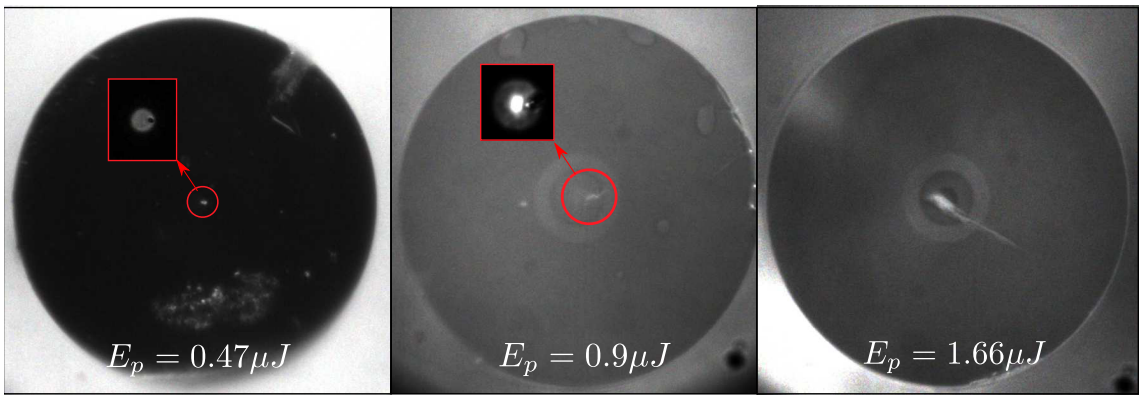

Figure 31: Examples of inscribed lines ws=0.1mm/s and PRR=120kHz at different E_p. At higher pulse energy, a filament below focal volume is obtained.

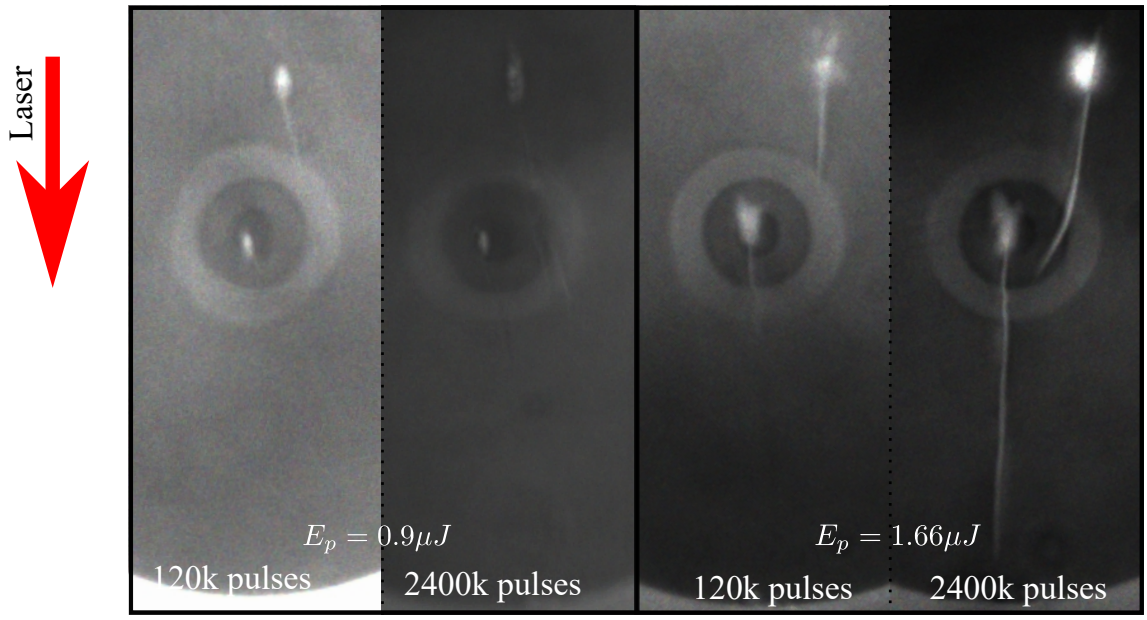

Figure 32: Dependence of pulse energy and pulse deposition on filament formation. Irradiation has been performed at two different E_p (0.9-1.66μJ) and pulse depositions ($120 * 10^3$ and $2400 * 10^3$ pulses) focused at fiber core and 30μm above.

filament is formed for $E_p = 1.66\mu J$. This structure, as discussed in section 2.3.2, might exhibit different RIC than focal volume, thus, its behavior should be studied.

For such purpose, the end-face of optical fibers have been transversally irradiated at the core and 30μm above at different pulse energy and with different amount of pulses deposited. Fig. 32 depicts images of irradiated areas at pulse energies of 0.9 and 1.66 μJ with pulse depositions of $120 * 10^3$ and $2400 * 10^3$ pulses. The inscription above the core produces filament in all cases while at the core is not produced at $E_p = 0.9\mu J$ and $120 * 10^3$ pulses. However, when pulse deposition of energy increases, the filament is produced. It is clear that pulse energy increases the filament length as deducted from Eq. 35. Pulse deposition also increases the length of the filament, as pulses seed the irradiated region allowing the filament to reach longer regions or even produce additional filaments, as in the case $E_p = 0.9\mu J$ and $2400 * 10^3$ pulses at 30μm above the core. For $E_p = 1.66\mu J$,

the increase of pulse deposition not only produces longer filaments but also with higher contrast.

The phase of both focal volumes has been measured with the inscription setup and QPm technique has been applied with a ±3µm defocusing. The results depicted in Fig 33 reveal a negative phase change in all the cases. When the focal volume is focused 30µm above the core, less E_p is required to perform LIRIC and phase change is greater than inscription at the core for low energies. This behavior is presumably caused by the increase of spherical aberrations on the longitudinal axis with distance. Despite transversal focus produced by cylindrical lens effect (Fig. 30.b,c), the transversal axis still suffers an increase of focal volume (Fig. 30.a) that reduces laser fluence. When pulse energy increases, phase change at the core is increased until $E_p = 1.99\mu J$ where phase change experiences a decrement. Inscription 30µm above the core exhibits a more constant phase change through different pulse energies. For energies higher than 1.5µJ phase change of both core and 30µm above become consistent and approximately of the same order.

Given the measured optical properties of focal volume, depressed cladding waveguides could be inscribed. The pulse energy range where a-priori best performance is expected is $1.5 - 2.18\mu J$. However, the characterization of filament properties will be addressed before in order to look for alternatives.

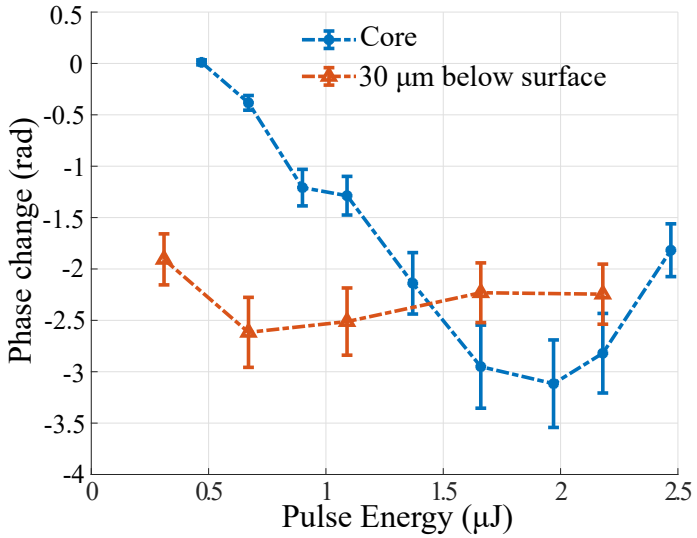

Figure 33: Phase change in the focal volume of lines written with ws=0.1mm/s, 120KHz at different pulse energies. The focal volume was focused at core (blue) and 30µm above (orange).

The main issue to be studied about filament is its RIC. This parameter can be qualitatively checked by placing the filament in the core region as in the previous experiment. Again, 300µm length lines were inscribed at the end of different optical fibers with ws=0.1mm/s and PRR=120kHz fixed and pulse energies 0.67,1.09,1.37,1.66 and 2.77µJ. The inscriptions were focused 30µm above the core. The results are depicted in Fig. 34. For $E_p \geqslant 1.66\mu J$ light is not guided through the filament, suggesting negative RIC. As can be noticed for $E_p = 1.66\mu J$, light is not being guided through the filament but for its vicinity. This is consistent with an expansive strain (negative RIC) filament surrounded by a compaction strain (positive RIC) to reach local equilibrium. At lower pulse energies, this trend is inverted. Induced filament guides light, their shape is amorphous, which suggest a lower

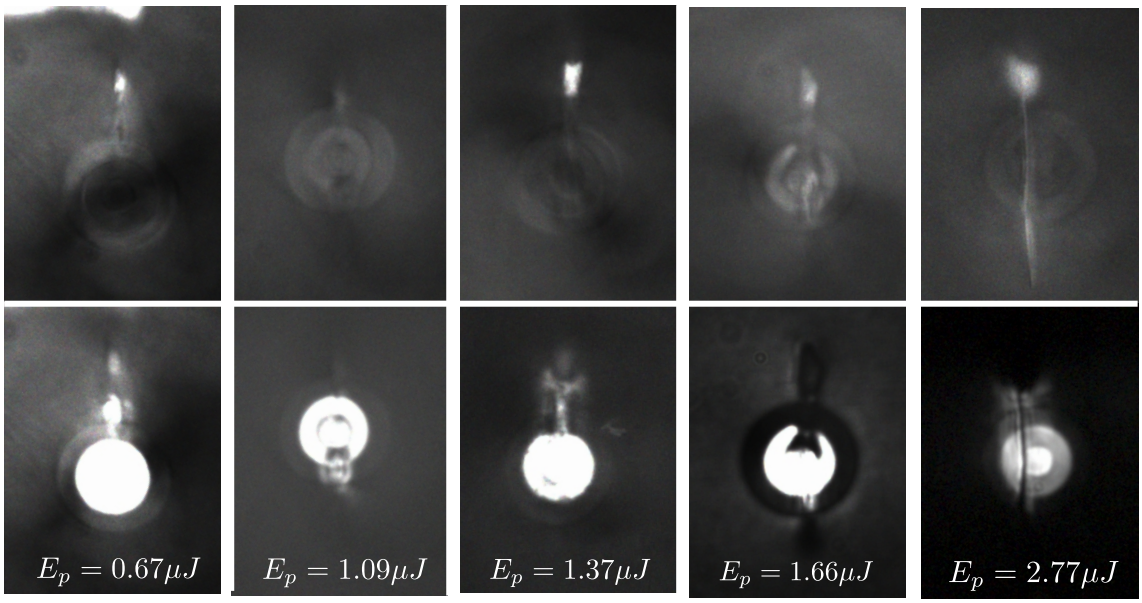

Figure 34: Filament formation produced 30µm above the fiber optic core at ws=0.1mm/s, PRR=120kHz and different pulse energies(except for $E_p = 1.09\mu J$ where focal point is placed above depressed cladding ring). The fibers were illuminated with a white light source to see light distribution. For energies lower than 1.66µJ filament guides some amount of light, implying a positive RIC. Higher energies exhibit no guiding at all, suggesting negative RIC.

performance [141, 69]. In all cases, focal volume has not guided light, thus is acceptable to affirm that for the given NA, geometry, PRR, and writing speed (ws) LIRIC produced at focal volume is negative.

The positive RIC region has been employed to inscribe a waveguide parallel to the fiber core. Focal volume has been placed 30µm below fiber surface at $E_p = 1.09\mu J$ PRR=120KHz and ws=10µm/s. After line elaboration, its characterization was performed with QPm in order to estimate average RICs (Δn) along the written waveguide and to compare it with the fiber core step. QPm images were captured with a 20x NA=0.45 piezo-mounted objective in an Olympus transmission microscope, defocusing the image $\pm 3\mu m$. One focused and two defocused images were computed with commercial software QPm from Iatia vision sciences to recover phase information from the amplitude images. An example of a phase image of the irradiated optical fiber is depicted in Figure 35.a. Both the core and the written waveguide can be distinguished from fiber cladding whose phase is similar to matching liquid. Waveguide has higher phase contrast ($\Delta\phi_{wg} = 2.710rads$) than fiber core ($\Delta\phi_c = 0.397rads$) and similar width as represented in the phase profile in Figure 35.b is achieved by adjusting the imaging depth, a focal volume phase profile as depicted in Figure 35.c, exhibiting negative phase (and therefore refractive index) change ($\Delta\phi_{fvol} = -2.819rads$). Positive phase displayed at the borders of focal volume suggests the presence of surrounding stress as a result of free stress glass expansion (inelastic strain) in the focal volume. Besides, optical retardance (proportional to birefringence) has been measured using de Sénarmont compensator in the same microscope. Measured retardance in focal volume is 110nm, which is too high for being caused just by photo-elastic effect, suggesting nanogratings formation [173].

For further characterization, another sample with the same parameters (the filament touches the core at the beginning of the inscription to couple light to the waveguide) was cleaved, and RNF profilometry was performed. When a light source illuminates the opposing end face, two lightspots are detected: one at the fiber core and another at the filament below the focal volume, at which the laser is focused; this can be noticed in Fig. 35.f. RNF was performed by Sira Optical Fiber Refractive index profiler at core and filament as depicted in Fig. 35.g,f. Core index change was $\Delta n_1 = 4.50(29) \times 10^{-3}$ while filament exhibits an inhomogeneous change varying from 8.9×10^{-3} to 14×10^{-3} with an average value of $\Delta n_2 = 11.00(78) \times 10^{-3}$. This configuration requires focal volume (which has a negative refraction index and hence is unable to guide light) to be placed above the core. As the filament is larger than the focal volume, writing precision requirements in the Z axis are lower than X and Y axes.

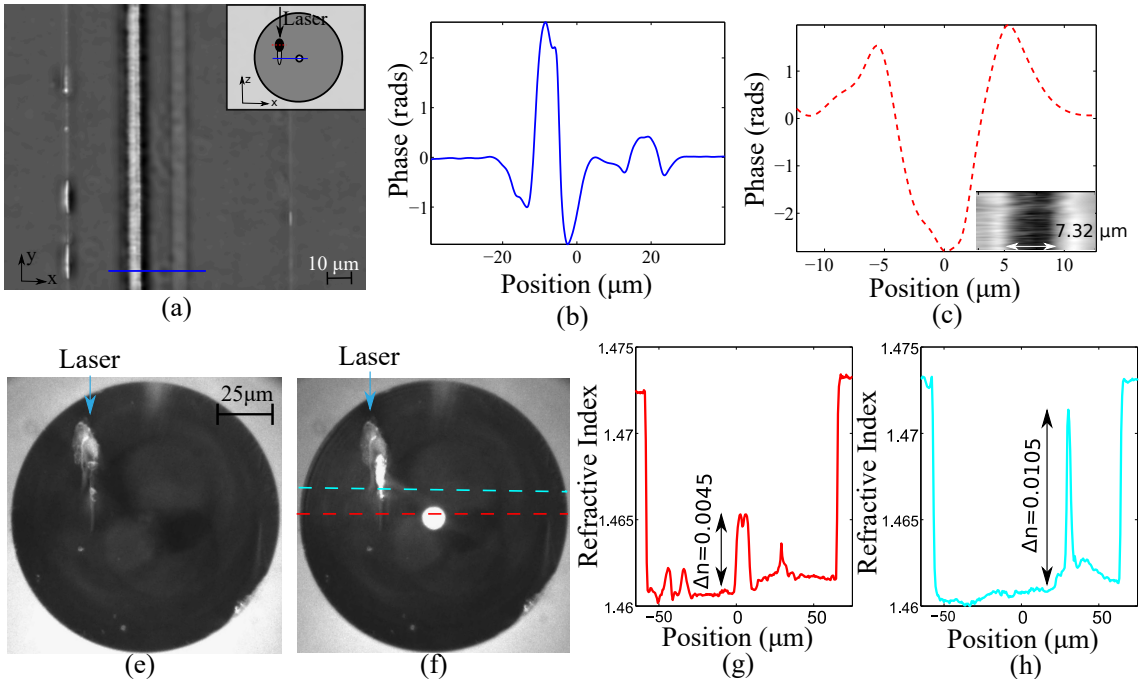

Figure 35: Optical fiber QPm image focused at the fiber core and cross-section diagram (a), phase profile of both core and waveguide (b), phase profile at focal volume with QPm image (c), CCD transversal capture of the inscription (e), the same inscription illuminating its opposing end face by a whitelight source, core (g) and inscription (h) RNF profiles.

5.2.2 MACH-ZEHNDER

The filament based waveguides can be used to manufacture several Optical Fiber Sensors (OFSs). Particularly, a Mach-Zehnder Interferometer (MZI) can be inscribed. In section 2.4.3, in fiber interferometers were briefly discussed, and cladding modes were highlighted to be the most used way to create a second arm with different Optical Path Difference (OPD). Waveguides can be an effective alternative way to cladding modes.

For such purpose, a MZI has been designed and simulated with BPM. The proposed design is depicted in Fig. 36. In this case, the mode splitting is achieved by inscribing a secondary waveguide into the optical fiber. Such inscription begins at the core and

displaces from the fiber axis with an insertion angle $\theta \in [4.3, 8.5]^\circ$ until a certain spacing from the core is achieved. Afterwards, inscription continues parallel to the core and then returns with the same insertion angle. L is the total sensor length, and X represents the waveguide spacing from the core. This design allows a single step inscription, which would imply a great reduction in its manufacturing cost.

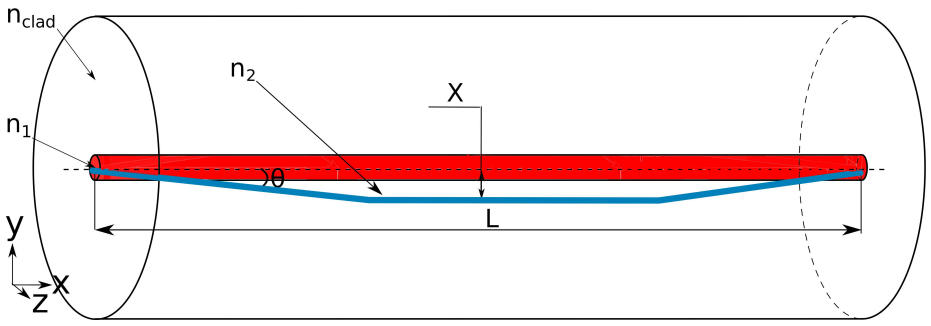

Figure 36: Depiction of the manufactured geometry. Secondary waveguide begins at the core and displaces to the cladding with a slightly angle θ and then goes back to the core with the same angle.

Simulations have been performed with BPM using the parameters depicted in Fig. 37 considering 2D geometry in order to make simple and faster calculations. The RI of the secondary waveguide n_2 was varied between $\Delta n_2 = n_2 - n_{cladd}$=1.001-0.02 to determinate the impact of this parameter on the interferometer performance. It is clear that at least, $\Delta n_2 \approx 10^{-2}$ is required to exhibit an interferometric shape. With the increase of n_2, the coupling efficiency and effective index increase, thus, the sensor exhibits higher finesse and bigger FSR (Eq. 50). The RIC of the filament waveguides address the requirements predicted by simulation.

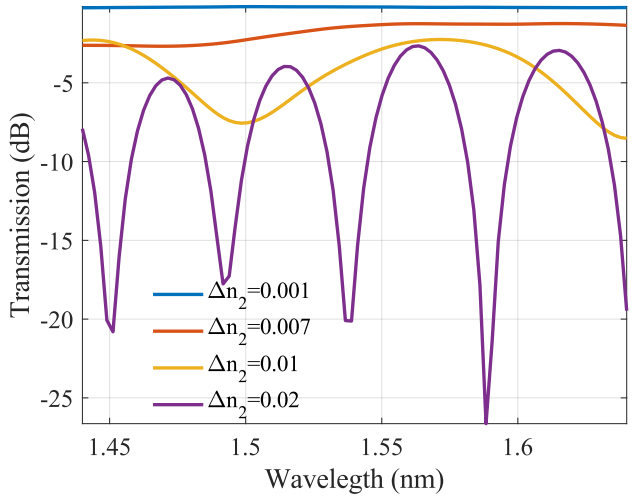

Parameter	Value
n_{clad}	1.4661
Sensor length (L)	3000µm
n_1	1.4706
Insertion angle (θ)	4.3°
cladding width	125µm
Spacing (X)	30µm
core width	8µm
secondary core width	3µm

Figure 37: Simulation results for different RICs of inscribed waveguide ($\Delta n_2 = n_2 - n_{clad}$ for the given parameters).

MZIs were inscribed with same inscription setup, connecting the input of the SMF to an HP Broadband light Source 83437A and the output to an Optical Spectrum Analyzer (OSA) from HP Optical Spectrum Analyzer 86142A. Fig. 38.a shows the cross-section of the optical fiber at the middle of the structure illuminated by a white light source. The focal region at 38µm below the surface can be noticed and also a small filament below guiding light at the depressed cladding ring at 10µm from the center. Images captured by a CCD camera of both sensor start/end focused at 38µm below fiber are depicted in Fig. 38.b,c.

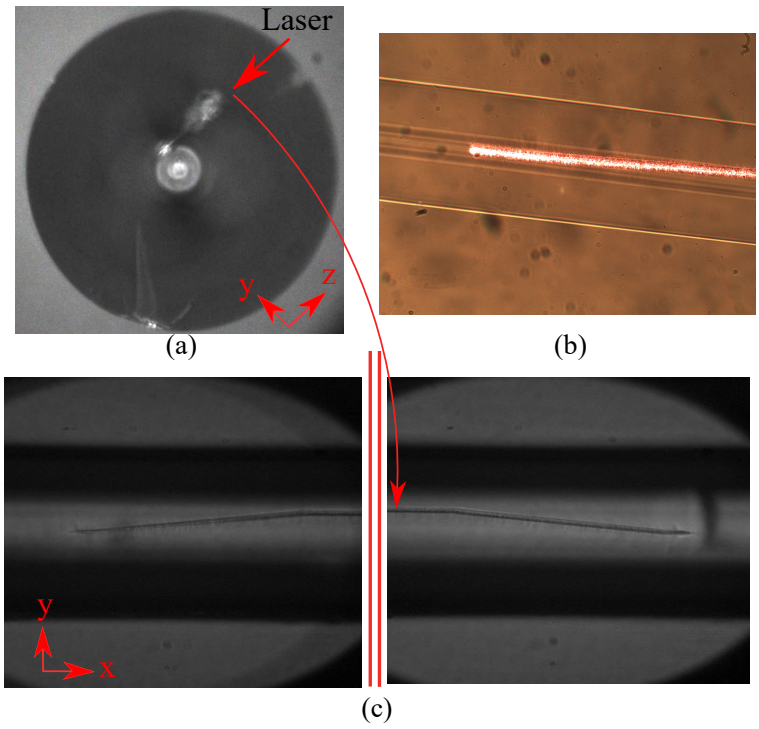

Figure 38: Manufacturing result: Capture of the inscribed waveguide cross section by transmission microscope (a). Transversal image of the optical fiber illuminated by a red laser source and submerged in index matching oil (b). Captures of both start and end of inscribed arm focused at 38µm below fiber surface (c). All the images have been captured by a CCD camera.

Some collected spectra are shown in Fig. 39. The typical decrease of Free Spectral Range (FSR) with sensor length L is appreciated at the top of Fig. 39 (spacing $X = 15\mu m$ and insertion angle $\theta = 8.5°$) while dip sharpness decreases with insertion angle θ as depicted at the bottom of Fig. 39 ($X = 15\mu m$ and $L = 3mm$). For $\theta = 1.7°$, the spectrum was irregular due to undesirable mode coupling caused by core/waveguide proximity over a long distance. This effect turns a higher value of X into a requisite to avoid mode coupling interaction while inscription is being performed.

Several factors play an important role in the measured transmission spectra that are not reflected in simulation results depicted in Fig. 37. For example, the simulation does not take into account the polarization effects induced by several changes produced in the structure. As mentioned in section 4.1.1, asymmetrical waveguides exhibit losses dependent on to polarization state and form birefringence. Let's assume that electrical field in both waveguide is decomposed in $\hat{x}$ and $\hat{y}$ component $E_1 = E_{x1} + E_{y1} \quad E_2 = E_{x2} + E_{y2}$. The total electrical field is then:

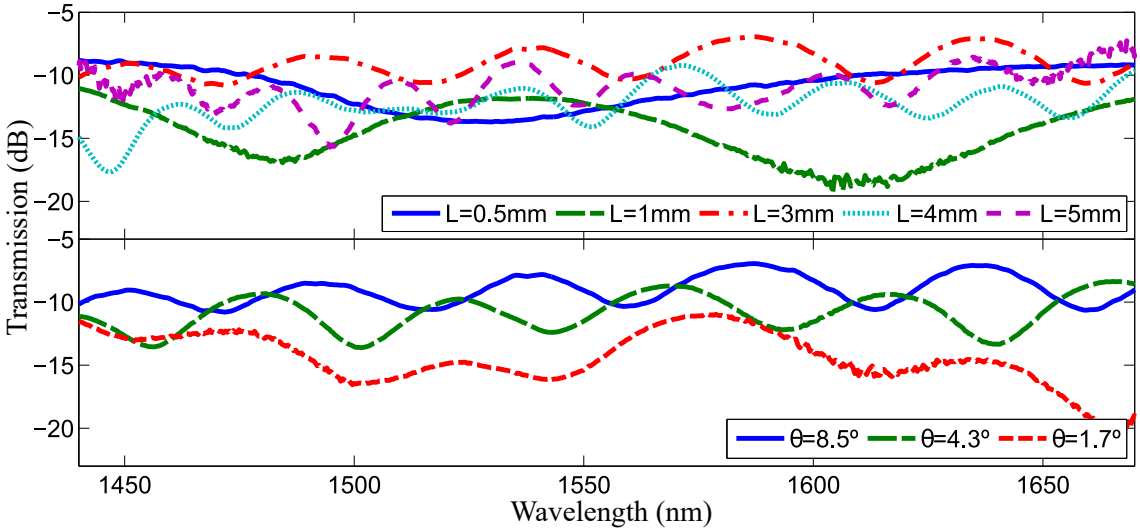

Figure 39: MZI spectra for parameter comparison: Interferometer length L from 0.5mm to 5mm at X=15µm $\theta = 8.5°$ and insertion angle θ from 1.7° to 8.5° at X=15µm & L=3mm.

$$E = (E_{x1}e^{i(k_1 z+\epsilon_{x1})} + E_{x2}e^{i(k_2 z+\epsilon_{x2})})\hat{x} + (E_{y1}e^{i(k_1 z+\epsilon_{y1})} + E_{y2}e^{i(k_2 z+\epsilon_{y2})})\hat{y}. \quad (84)$$

This expanded equation leads to a more complex profile than the one shown in Eq. 45

$$I = I_{x1} + I_{x2} + I_{y1} + I_{y2} + \frac{\sqrt{I_{x1}I_{x2}}}{2}\cos(OPD + \Delta\phi_x) + \frac{\sqrt{I_{y1}I_{y2}}}{2}\cos(OPD + \Delta\phi_y). \quad (85)$$

Where OPD= $k_1 z - k_2 z$ and $\Delta\phi_x = \epsilon_{x1} - \epsilon_{x2}$, $\Delta\phi_y = \epsilon_{y1} - \epsilon_{y2}$. Assuming $I_{x1} \simeq I_{x2} \simeq I_{y1} \simeq I_{y2}$ and making the following variable changes $\bar{OPD} = OPD + \Delta\phi_x$ and $\epsilon = \Delta\phi_y - \Delta\phi_x$, equation 84 can be rewritten as

$$I = 4I + \frac{I}{2}(\cos(\bar{OPD} + \frac{\epsilon}{2})\cos(\frac{\epsilon}{2}). \quad (86)$$

Which exhibits an envelope function; an example of this behavior is shown in Fig. 39 for the MZI with $L = 4\mu m$. This assumption cannot always be verified as generally the coupling/decoupling of the second waveguide is generally different for the two components of the electric field.

Now that a MZI has been designed, manufactured and characterized, the next logical step involves studying its spectral behavior with different parameters. In this way, its viability as a sensor can be evaluated.

5.2.2.1 *As temperature sensor*

The first parameter that can be varied is temperature. As stated in section 2.4.1, high-temperature sensing is of particular interest and highly demanded in a wide variety of sectors. Besides, FBG exhibit a length about 4-8mm while the manufactured MZI can be as low as 0.3mm (exhibiting only one interference dip in the second and third window). This makes desirable a prove of concept of the spectral response of MZI to temperature variations.

For such purpose a length of L=0.3 mm was chosen to perform a temperature characterization by heating the sample with a Carbolite tubular furnace. Starting from 50°C, the temperature was increased in steps of 50°C averaging its spectra over 10 minutes for every temperature up to 650°C. Transmission spectra for temperatures up to 650°C are represented in Fig. 40.a. As temperature increase, the wavelength of the resonance decreases.

For higher temperatures than 650 °C transmission peak shifts below emitted spectra and lose its interferometric shape. The dip wavelength in function of temperature is depicted in Fig. 40.b. The sensitivity increases at higher temperatures suggesting a RI decrease of the inscribed waveguide. This is consistent with the vanishing of type I modifications (the filament refractive index) and of the compressive stress caused by the laser irradiation induced expansion in the focal volume as thermal annealing relieves stress when viscosity decreases.

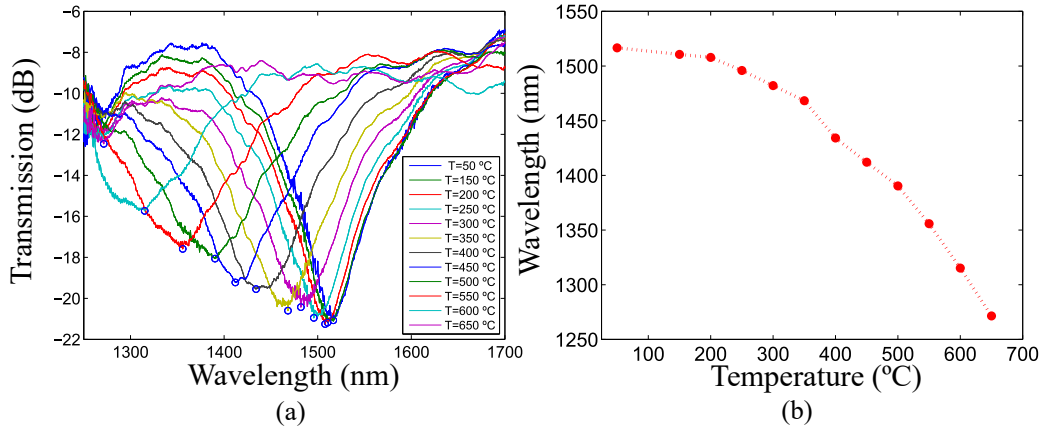

Figure 40: Selecting L=0.3 mm, (a) plots several transmission spectra at different temperatures ranging from 50°C to 650°C while (b) plots its dip wavelength.

5.2.2.2 *As Curvature Sensor*

Once the temperature has been characterized, another interesting parameter to study is curvature. The MZI design makes it suitable for vector bending sensing. The increased index contrast of the waveguide will increase the effective mode index difference, making size reduction possible in comparison to previously reported curvature sensors, that usually exhibit lengths bigger than 10mm [174, 175]. This new design should improve the curvature range, with ease of implementation, while not requiring complex adaptive optics for cylindrical geometry compensation.

Both simulations and experimental measurements have been performed. The model of the fiber bending was carried out in two different ways. One was the actual bend of the fiber in the simulation domain, an the other was the conformal mapping employed in section 4.4.4 represented by Eq. 83, its equivalent form for polar coordinates is [172]

$$n_{bend} \approx n\Big[1 + (r\kappa)\cos(\phi)\Big]. \tag{87}$$

Here, $\kappa = 1/R$ is the curvature, the inverse of bending radius R towards bending axis and r,ϕ the polar coordinates as represented in Fig. 41. When bending occurs at the $+Y$ axis direction (for the design depicted in Fig. 41), the effective secondary waveguide mode

index decreases, reducing Δn from Eq. 87 and hence, the OPD. Likewise an increment in Δn (and thus the OPD) occurs when bending takes place in the opposite direction. Based on this dependence phenomenon, a relation between curvature and λ_{dip} can be established, which will be studied by different simulation and experimental tests.

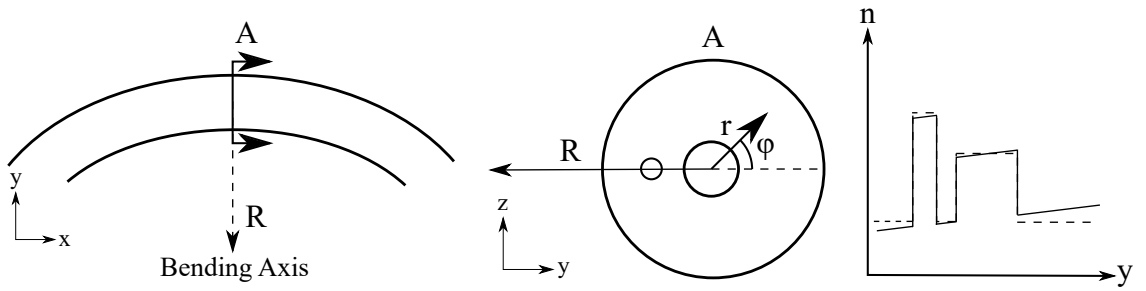

Figure 41: Model for a bending optical fiber with two cores and its effective index profile due to coordinate transformation.

In order to measure the applied curvature, the fiber has been clamped on two xyz platforms separated an initial distance L_f, leaving the sensor in the middle of them as described in Fig. 42(a). One platform remains fixed while the other one is displaced in the X direction. Fiber bending is thus achieved by moving the depicted movable platform in the X axis. Curvature estimation has been achieved using the circumference relation $L_f - x = L_f \operatorname{sinc}\left(\frac{L_f \kappa}{2}\right)$ [174].

As $1/\kappa = R >> L_f$ is assumed, sinc function can be expressed as a power series where only the two first terms are considered $\left(\operatorname{sinc}(x) \approx 1 + \frac{-x^2}{3!}\right)$, giving the easy to handle expression

$$\kappa \approx \sqrt{\frac{24x}{L_f^3}}. \tag{88}$$

Bending direction is also controlled by placing plane YX of the sample perpendicular to the plane YX of design and sandwiching the sensor between two slides, restricting the movements of the sensor and constraining bending to the Y axis only (+Y and -Y (as in Fig. 42.a) direction).

When the sensor is bent, the interference dip wavelength λ_{dip} suffers an increment/decrement with respect to bending direction. Bending towards the -Y direction produces a λ_{dip} increment as depicted in Fig. 42 and decreases when bending is produced at the opposite direction. Also, dip wavelength remains insensitive to Z direction bending. After several measurements with different parameters maximizing X and decreasing θ best sensitivities have been obtained for $\theta = 4.3°$ and X=30μm with a minimum sensor length L=3mm. Sensors with lower L exhibit a sensitivity drop caused by having a relatively large coupling zone. Measurements for the mentioned parameters are depicted in Fig. 43.a. Experimental data exhibit an approximately linear behavior with $R^2 = 0.9934$ and $R^2 = 0.9871$ for +Y and -Y directions respectively. Their linear slopes are -0.1329(41)$(nm \cdot m)^{-1}$ and 0.1054(64)$(nm \cdot m)^{-1}$, which correspond to a sensitivity of 7.52(23)nm/m^{-1} and 9.49(58)nm/m^{-1} for +Y and -Y bending respectively exhibiting a repeatability of 3.45%, obtained by measuring sensitivity 5 times in each direction and

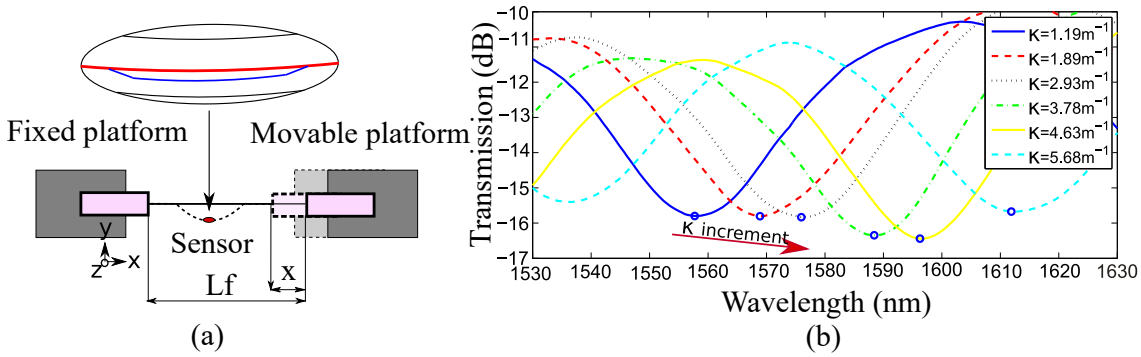

Figure 42: Curvature measurement scheme (a), MZI spectra for different curvatures ranging from $1.19\mathrm{m}^{-1}$ to $5.68\mathrm{m}^{-1}$ towards -Y direction. Sensor parameters: L=3mm, $\theta = 4.3°$ and X=30µm (b).

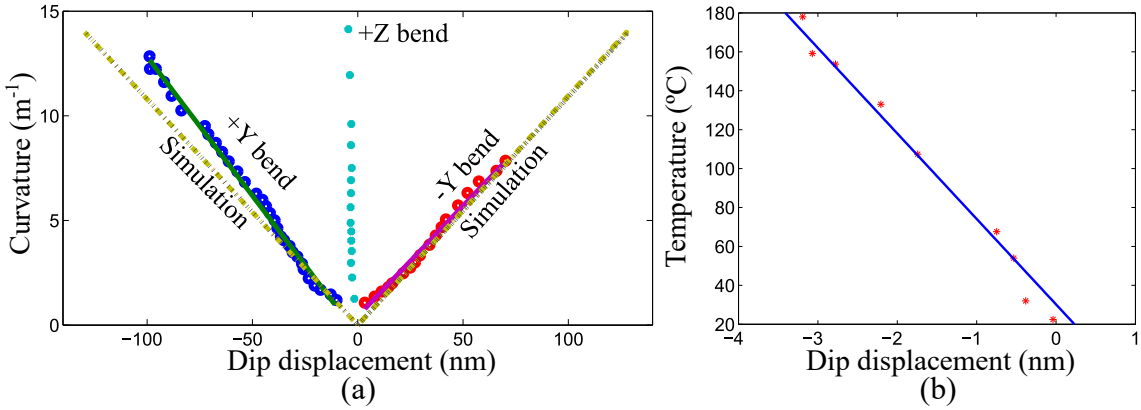

Figure 43: (a) Experimental measures of the dip wavelength displacement with curvature for the three given bending axes (+Y, -Y, +Z) and the simulation results for both conformal mapping and actual bend for the horizontal axes (+Y, -Y); (b) Experimental variation of the dip wavelength displacement with temperature.

selecting the highest deviation from the first measurement. The other bending axis show different responses, improving their sensitivity with the alignment to Y axis. This dependency is deducted from Eq. 41, where maximum index increment/decrement occurs when parallel to that axis bending whereas perpendicular bending produces no overall OPD.

Simulations are also depicted in Fig. 43(a) for the same parameters and measured index difference in the previous section. Both conformal mapping and circular bending simulations are in good agreement with each other having λ_{dip} linear and symmetric dependency with curvature. Experimental data differ 23%(+Y) and 3.8%(-Y) from them. This slightly asymmetry in +Y may be explained as a consequence of waveguide inhomogeneities in refractive index and cross-section caused by stress forces located inside the filament. Irregular cross-section and the RI could induce different modal effective index dependences with curvature for the bending plane. Several simulations introducing sinusoidal perturbations in longitudinal and transversal profiles have been performed, while symmetry and linear dependence have remained unaltered. Besides, the compression or stretching associated with the bending might be perturbed by the inscription itself as it is a source of permanent

strain and elastic stress that could induce a certain deviation from Eq. 87. This in turn, could alter λ_{dip} response with bending axis direction.

From temperature characterization performed in the previous section, there is a strong cross sensitivity expected at high temperatures; however, below 200°C the sensitivity is reasonably low. For such purpose, another temperature study was also performed at lower temperatures. This dependency is depicted in Fig. 43.b where an approximately linear tendency is appreciated in the range 25-180°C where the sensitivity was found to be 0.0228(22)nm/°C. The sensor cross sensitivity is therefore as low as $0.0024(3)m^{-1}/°C$.

5.2.2.3 *Inscribed in tapers*

The proposed structure may be modified to enhance its sensitivity to other parameters. For example, its current design provides resistance to RICs of the external media. However, the same structure inscribed into a taper can result in a RI sensitivity. This is caused by the decoupling properties of tapers and the proximity of waveguide to the external medium. This behavior has been studied through a preliminary simulation. The simulated structure has the shape depicted in Fig. 44.a. Here, MZI has the same length than the taper. The taper transition has been modeled by a quadratic function (with 0.45mm length), and the width of the taper waist W has been set as a free parameter. The RIC of the inscribed waveguide has been set to $\Delta n_2 = 0.013$; the remaining parameters are the same than previous simulation (Fig. 37.b). Here, it is clear that a lower W reduces dip amplitude as a consequence of mode decoupling, exhibiting an inhomogeneous interferometric shape. The background index has been modified from 1.3 to 1.4 to measure the dip displacement produced, and the result is depicted in Fig. 44.c. The dip displacement with RI behaves as a second-order polynomial, implying that sensitivity linearly increases with RI. Sensitivity increases with the decrease of taper waist width, in this way, inscription into taper waist increases RIC sensing performance at the cost of a smoother pattern.

Now, a quick proof of concept was performed by inscribing the MZI structure in a taper waist of $W = 50\mu m$. The fiber taper had 3cm taper waist and 5mm of taper transition. The laser was focused directly at taper surface instead $30\mu m$ bellow with $E_p = 0.9\mu J$. A capture of inscription result is shown in Fig. 44.d. The spectra are depicted in Fig. 44.d immersed in air and water ($n_D = 1.33$). The pattern is extremely inhomogeneous compared with regular MZI; however, the dip loss is higher than the simulated version (about a factor 2) and the dip displacement suffered is about 25nm. This sensitivity is significantly improved in comparison to regular MZI where the spectra do not exhibit observable variation.

5.2.3 SUMMARY

In this section a study of femtosecond laser inscription without adaptive optics has been performed. Typical aberrations due to geometry have been mentioned and experimentally observed. The RIC has been qualitatively studied, obtaining a negative LIRIC at focal volume for all the studied pulse energies[2]. Filament, on the contrary, exhibited RIC at low pulse energies and negative at high energies. This filament has been found to be dependent on incubation, pulse energy and penetration in the optical fiber.

This positive RIC has been used to manufacture waveguides inside the optical fiber. The characterization performed to this waveguides employing both RNF and QPm consistently

2 A more quantitative study carried out with QPm is consistent with the prior study.

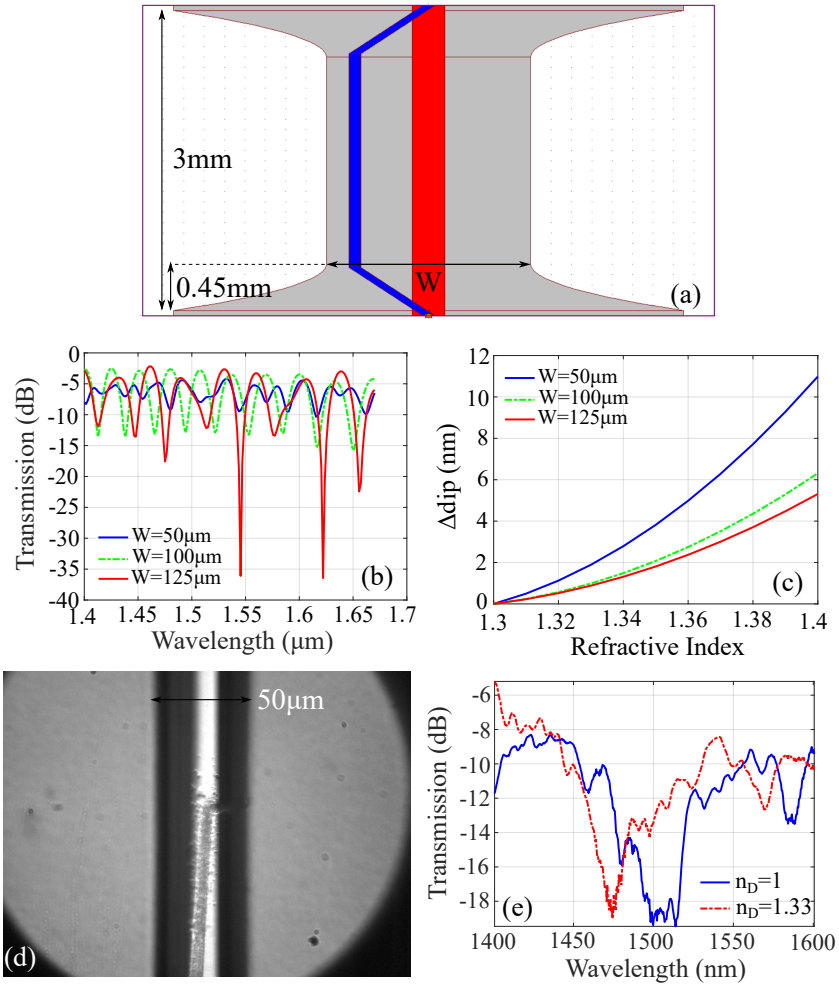

Figure 44: Simulation scheme of the proposed MZI inscribbed in a taper (a), spectra of simulated MZI at three different taper waist width (125, 100, 50μm) (b), the dip displacement with RI for the three widths (c). CCD camera capture of MZI arm focused at fiber surface inscribed in a taper waist ($W = 50\mu m$) (d) and its corresponding spectra inmersed in air and water ($n_D = 1.33$) (e).

exhibits an averaged Refractive Index Change of $\Delta n_{wg} \approx 10^{-2}$. This strong index change waveguides have been used to manufacture a MZI with good index change and resemblance to BPM simulations. This MZI has been characterized as a high temperature sensor and curvature sensor. The bending sensitivity depends on bending axis, exhibiting potential to bending vector sensing with a length lower than conventional bending vector sensors.

In addition, another MZI configuration has been proposed. Inscription in a fiber taper has been proposed to enhance RI sensitivity. Simulations and preliminary studies corroborate this assumption. A deep characterization should be performed to quantitatively study its performance with RIC.

5.3 INSCRIPTION USING ADAPTIVE OPTICS

In the previous section, all the inscriptions in optical fiber were performed by a microscope objective directly focusing on the fiber. With this approach, the geometry of the optical fiber plays an essential role in the inscription result. The pulse propagating through the fiber exhibits a *cylindrical lens* effect that stretches its width in the transversal direction to the optical fiber. Applying the setup explained in section 4.4.1, one can remove this effect and achieve a propagation with aberration independent on direction.

In this section, a comparison between inscription with and without adaptive optics will be performed, characterizing some devices inscribed with adaptive optics in a similar way than the previous section. Results will be employed in grating inscription, both FBGs and RFGs will be inscribed being the later employed in a setup for a fiber cavity laser.

5.3.1 WAVEGUIDE INSCRIPTION

The simple setup proposed by Zhou and Roberts [153, 154] has been applied to the previous writing setup explained in section 5.1. Inscriptions performed in the previous section will be repeated in order to compare obtained results focusing on phase behavior. In this way, several lines have been inscribed at the core of the optical fiber to study the amount of phase change induced by the laser irradiation in the focal volume. The lines were written focusing at the core with PRR=120kHz and ws=0.1mm/s with pulse energies ranging from 0.03 to 2.47 µJ and captures were taken with $\pm 3\mu m$ defocusing to generate a phase image with QPm. The phase results of the main phase change are depicted in Fig. 45.b, here, the inscriptions exhibit a positive phase change as opposed to the inscriptions without adaptive optics where phase change always is negative. Another remarkable feature is the modification threshold, being substantially reduced in comparison to direct exposition. This reduction is mainly attributed to the distort of the focal point, degrading spatial resolution and hence reducing fluence. This is represented in Fig. 45.a where two intensity images of two lines inscribed with same parameters, one with and another without adaptive optics are shown. The line width with adaptive optics is larger than direct exposition as a consequence of lens effect removal and a more compact focal volume.

The amount of phase change with E_p, at low energies, exhibit a smooth increase consistent with type I modification. Phase reaches local maxima at 0.19µJ, and then the inscription slowly decreases phase while increases line width. When the pulse energy reaches 0.67µJ phase increases again as a consequence of inhomogeneous inscription, here both positive and negative phases are observed due to high elastic strain induced on inscription and other causes. The structure experiences an abrupt phase change at energies above 1.37µJ this change becomes constant with higher energies. This behavior reflects the Type III regime where ablation has removed the cladding surface. The measured phase change is the index matching liquid that has slipped through the core.

From the results obtained, the range $0 - 0.5\mu J$ can be used to write both type I gratings and waveguides. Gratings, as opposed to waveguides, cannot be written without adaptive optics unless its period is significantly large implying that Bragg diffraction cannot take place in the studied spectra. In the following section, gratings will be inscribed and characterized.

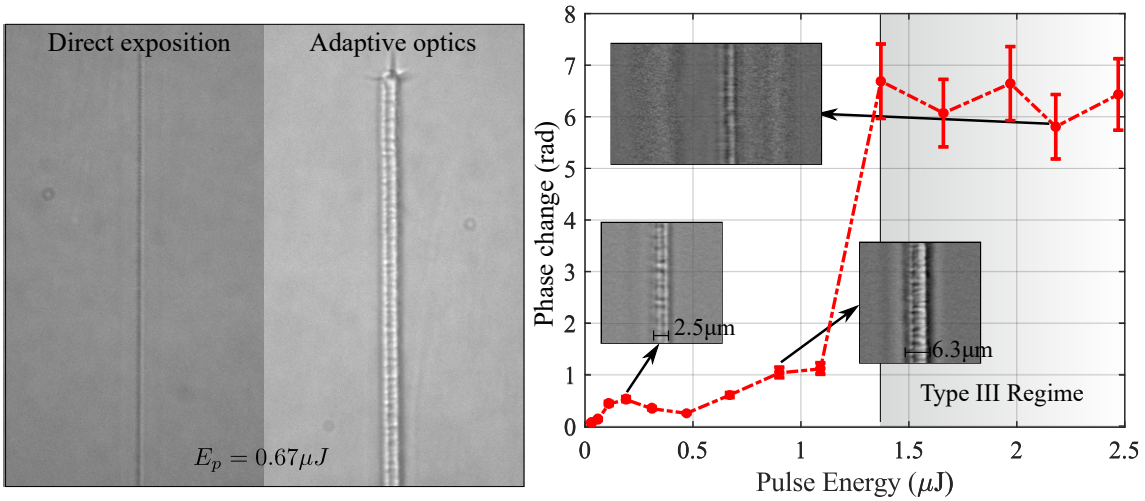

Figure 45: Inscription with and without adaptive optics at $E_p = 0.67\mu J$, 120KHz ws=0.1mm/s (a). Phase change vs pulse energy for 120KHz ws=0.1mm/s inscriptions at fiber core with adaptive optics (b).

5.3.2 GRATINGS

Gratings can be inscribed with fs applying two major approaches, first ones is phase mask, that can produce quasi-sinusoidal patterns; however, they are expensive and the period is fixed for a given wavelength. The other common option is the PbP technique, which allows total control over the period selection at any wavelength but the pattern exhibits a certain amount of noise that leads to several cladding modes. In this section, the PbP technique will be employed to inscribe FBG and RFG; this later will be inscribed in a taper to be used as a random backscattering generator to feedback a fiber cavity laser.

The PbP technique is simply based on the control of PRR in function of writing speed to precisely deliver pulses with a desired spacing between them (the grating period). In this setup, this has been achieved by a pulse picker integrated into the laser employed as explained in section 4.1. The grating period is controlled by

$$\Lambda = ws/\mathrm{PRR}. \tag{89}$$

In this way, gratings with different periods and E_p have been written in the fiber core of an SMF-28. Some remarkable examples are depicted in Fig. 46.a, where the gratings were written with periods 20,5,1,0.5µm for pulse energy $3.94, 0.67, 0.47, 0.19\mu J$ respectively from left to right. The pulse energy determines the width of the modification volume. These must not surpass the period as the volume overlap may distort the pattern. This is clearly seen in the $\Lambda = 0.5\mu m$ grating. The pulse overlap prevented the structure from forming a periodic pattern. For the current setup, periods lower than 1µm are challenging and hard to write. This can be an issue for FBG inscription, where Bragg reflection at the third window is commonly achieved with periods $\approx 0.5\mu m$. However, second harmonic can be used instead (Eq. 39), in this way FBGs can be inscribed. For this purpose, gratings with $\Delta = 1\mu m$ ($E_p = 0.47\mu J$) have been characterized through phase imaging and RNF profilometry.

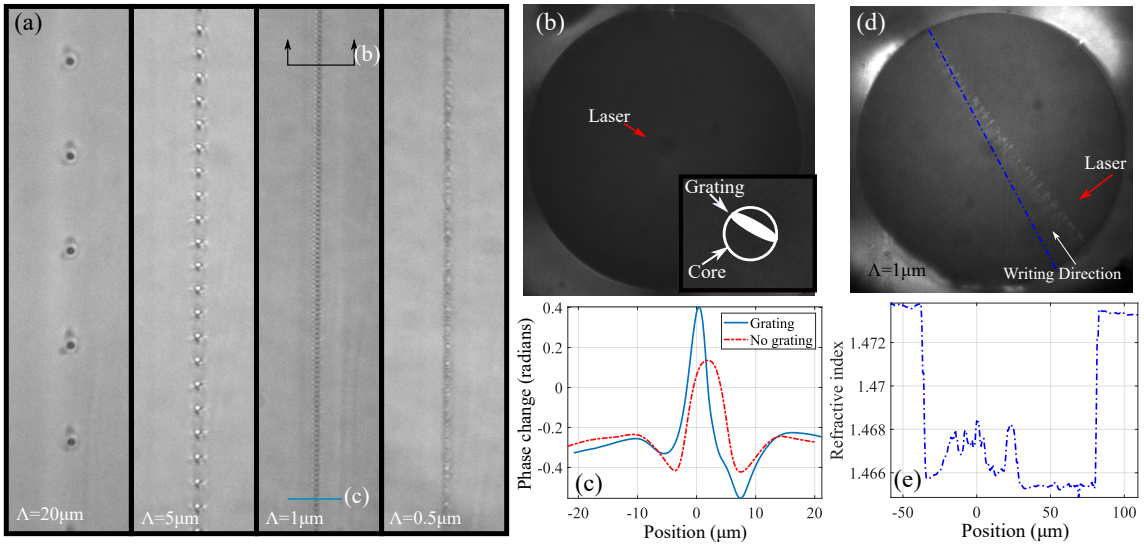

Figure 46: Examples of different grating inscription at $\Lambda = 20, 5, 1, 0.5\mu m$ & $E_P = 3.94, 0.67, 0.47, 0.19\mu J$ from left to right (a). The cleave of grating $\Lambda = 1\mu m$ and $E_P = 0.47\mu J$ (b), its phase profile (c) a longitudinal cleave of the grating (d), the doted blue line represents the RI profile in (e).

In section 4.4.1 the relation between RIC and phase was pointed out in Eq. 80. The inscription width also plays an important role in the RIC calculation from phase change; thus, it must be measured. Cleaving the grating is a simple way to measure the shape of the inscription area. The grating depicted in Fig. 46.a with $\Lambda = 1\mu m$ was cleaved and inspected with the same microscope optics of the setup. The image of the cleaved fiber is depicted in Fig. 46.b, where the inscription is hardly noticed in the core area. A diagram is attached above the image to help representation. Here, the modification area has the same height than the core and few micron widths. The phase change has been measured with QPm with $\pm 3\mu m$ defocussing in a similar way than section 4.4.1. The phase profile is depicted in Fig. 46.c for the studied grating and a pristine fiber. The measured phase change is $\Delta\phi = 0.297$ which gives a RIC of $\Delta n_{550nm} = 0.0032(4)$. This value will be compared with RNF profilometry. The same pattern is then transversally inscribed at the end-face of another fiber. The result is depicted in Fig. 46.d where the grating exhibits a continuous period and is composed of different pulses with an irregular shape. The light coming out of the fiber exhibits a classic diffraction pattern[3] that will be further discussed in the Chapter 6. A RNF profile has been performed in the blue dashed line section; the result is depicted in Fig. 46.e where both core and grating are observed. The RIC of the grating is $\Delta n_{633nm} = 0.0029(2)$ which is consistent with phase measurements.

Now that shape and RIC has been measured. FBGs have been inscribed in the fiber core with the same properties and $\Lambda = 1.06\mu m$. Both reflexion and transmission spectra are depicted in Fig. 47.a, here the reflected second harmonic λ_2 exhibits 14.8 dB gain respect to pristine reflected spectra. Losses in transmission spectra are higher, reaching 33.13 dB. In addition to λ_2, there are several cladding modes as expected from a type I fs FBG. The grating was not symmetrically inscribed in the core cross section, thus, the spectrum exhibits the decoupling to several higher modes that overlap, producing a long region at shorter wavelengths with high losses. These cover modes are sensible to bending in

3 With low order efficiency, this is mainly attributed to the unmodified region of the core.

comparison to λ_2. Not only the second harmonic can be used, but also third and fourth, other techniques such as line by line [176] that requires higher periods. With this in mind, third and fourth harmonic ($\Lambda_3 = 1.59\mu m$ and $\Lambda_4 = 2.12\mu m$ respectively) were inscribed and compared in Fig 47.b with the already inscribed second harmonic. Both exhibit the same ressonant wavelength than λ_2 but with lower losses (10.47 and 4.29 dB respectively), the cladding modes of fourth harmonic exhibit higher losses than its λ_B.

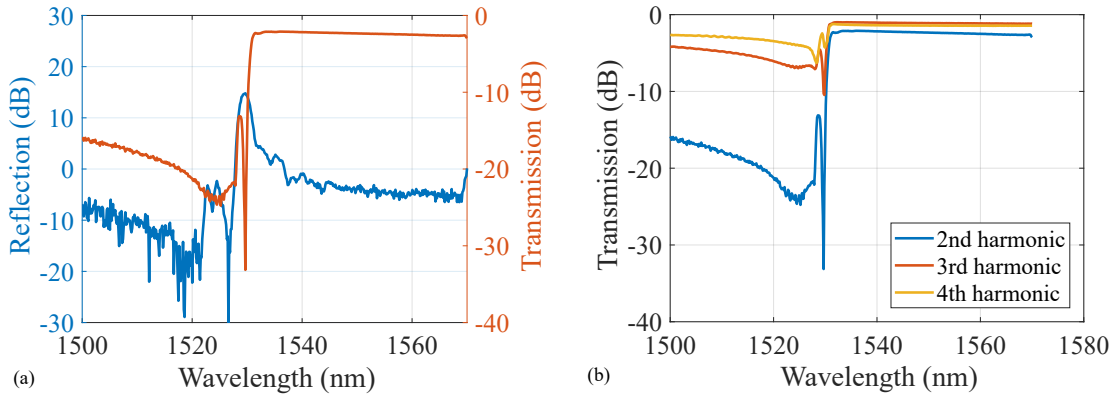

Figure 47: FBG spectra: Reflection and transmission spectra for $\Lambda_2 = 1.06\mu m$ and $E_p = 0.47\mu J$ (a). The transmission spectra of second ($\Lambda_2 = 1.06\mu m$) third ($\Lambda_3 = 1.59\mu m$) and fourth ($\Lambda_4 = 1.06\mu m$) harmonic (b).

5.3.2.1 *Random Fiber Gratings*

Once a proof of concept of FBG inscription has been performed, other schemes are worthy of study. The developed Point-by-Point technique will be employed to inscribe Random Fiber Grating (RFG). In section 2.4.2 RFGs were addressed as multiple interferometers with aleatory relation between each other generating a noise-like interference pattern with common reflexion. Besides, its increment of Rayleigh backscattering when inscribed by fs lasers was also highlighted. This effect may be enhanced by the inscription of these patterns in Tapered Optical Fibers (TOFs), given their increment of Rayleigh scattering. Thus, inscription of a RFG in a TOF can be used as a selective mirror in a single cavity optical fiber laser.

This can be achieved by randomly varying the PRR while writing. In this way, the grating will exhibit a random period between two established limits. This methodology has been employed in a 50µm taper waist of 2cm length with a taper transition of 5mm (Fig. 48.b). PRR was set to produce periods ranging from 1 to 10 µm for $ws = 0.1mm/s$ at $E_p = 0.47\mu J$. The result is depicted in Fig. 48.c where the TOF exhibits arrays of different period pulses. This is caused by the delay produced in the pulse picker controller when a new PRR is set, in this time lapse a small array of reflectors is produced. The manufactured grating exhibits then a quasi-random distribution.

This taper has been placed in the setup explained in Fig. 48.a. The cavity is pumped through a 1480nm laser connected to the cavity through a WDM. This later is connected to 4 meters of Erbium Doped Fiber (EDF). The analyzed EDF was I25 from Fibercore Inc. The cavity ends at a fiber loop mirror, and at the opposing side of the cavity, after the WDM, the inscribed TOF is placed. Fig. 49.a depicts the output spectra of a pristine TOF where the reflected signal produces a spurious lasing. The longitudinal modes compete with each other avoiding an actual lasing. However, when an inscribed TOF is placed, lasing is

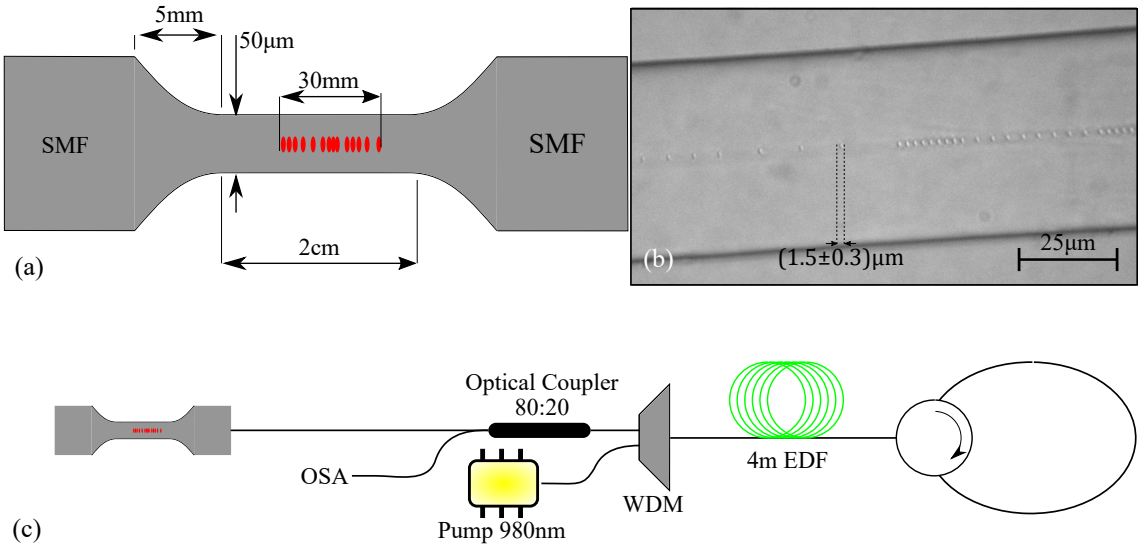

Figure 48: Scheme of the processed TOF (a), a capture of the grating inscribed in the TOF (b) and scheme of the single cavity laser (c).

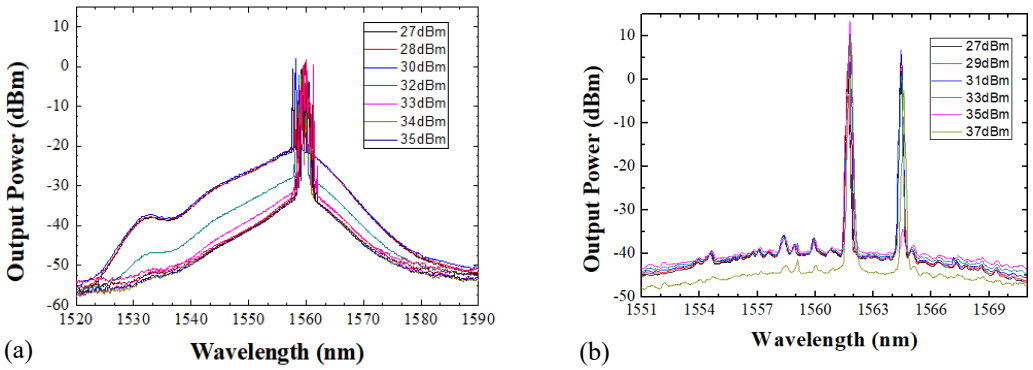

Figure 49: Output power of the setup depicted in Fig. 48 employing a 50µm width TOF without inscription (a). Output power of the setup depicted in Fig. 48 employing a 50µm width inscribed TOF (b),two modes have been achieved (1562 and 1564.5nm) with 10 dBm output power.

achieved thanks to the quasi-random feedback produced by the RFG. Its spectral output is depicted in Fig. 48.b, two modes have been achieved at 1562 and 1564.5nm with 10 dB output power and 15.4dBm of threshold pump power.

5.3.3 SUMMARY

In this section, a simple setup of adaptive optics has been included in the inscription method. This setup avoids problems during focusing that may reduce laser fluence and removes the cylindrical lens effect. The inscribed lines exhibit a smooth, positive RIC at low pulse energies and an inhomogeneous index change at intermediate energies before ablation is achieved. The smooth regime has been used to inscribe gratings using the point by point technique in the fiber, these have been characterized and the produced RIC has been measured independently and consistently by two different methods. After the

characterization steps, a proof of concept of FBG inscription was successfully performed, exhibiting the expected pattern for a type I-fs FBG. Finally, a quasi RFG was inscribed in a TOF and used into a short linear cavity laser exhibiting two different wavelengths at 1562 and 1564.5nm with an output power of 10 dB.

5.4 CONCLUDING REMARKS

In this chapter, a study of fiber inscription has been performed. A typical transversal writing setup has been employed to inscribe different patterns into the optical fiber. For that purpose, characterization of processed structures was performed starting from a qualitative approach to a more quantitative one using both RNF and QPm. In this way, Type II waveguides and Type I gratings were characterized and employed to develop new structures such as waveguide based MZI and quasi RFG inscribed in TOF. Some applications were proposed for these structures exhibiting good performance.

There is still much future work that must be performed. The manufactured Mach-Zehnder Interferometer exhibits a high sensing potential that can be easily enhanced by modifications to the base scheme. The inscribed FBG should be post-processed, and temperature characterized in order to study its high-temperature performance. More improvements to the setup should be addressed to achieve better performance.

6

INSCRIPTION AT END-FIBER

In the previous chapter, the inscription was transversally performed in an intermediate region of the fiber. This region is where the majority of fs laser processing works are focused. However, processing at the fiber end-face also draws attention due to the sensing and beam shaping potential that the previous inscription lacks.

This chapter will address the inscription at the end face of the fiber. The study will start with the most simple element, a diffraction grating at the Single Mode Fiber (SMF) surface. From this simple structure, more complicated ways to inscribe diffractive patterns will be studied with several optical fibers. Some proposed applications will highlight the sensing performance of these structures.

The chapter is composed of five sections. Section one consists of a very brief overview of the inscription setup. In section two diffraction gratings will be inscribed at the fiber surface and few microns below fiber surface. These patterns will also be inscribed in Multi Mode Fibers (MMFs) and Polymer Optical Fibers (POFs). These results will be characterized and compared with simulations and theory. Section three addresses a two-dimensional approach, proposing new configurations employing more complex fibers. The applications of the inscribed structures will be presented in section four. Finally, in section five, some concluding remarks and a few future works will be stated.

6.1 SETUP

The inscription setup is the same as presented in Chapter 5 with the addition of a fiber holder attached to the movable stage. The Fig. 50 depicts the complete setup for the fiber inscription. The laser pulses from a commercial femtosecond Fiber FLCPA[1] were focused through a NA=0.5 objective lens from Mitutoyo converging at the fiber end-face fixed to an HP 8100FB bare fiber adapter placed in a platform attached to a nano-resolution XYZ motor stage from Aerotech. The fiber adapter is illuminated in reflexion by four white light sources placed at the corners.

6.2 DIFFRACTION GRATINGS

Diffraction gratings are one of the most straightforward periodic patterns recorded in photosensitive materials. They are periodic variations in transmittance or phase. When illuminated by an incident planewave, the emerging wavefront exhibits phase or amplitude periodicity. This periodicity, when translated to the frequency domain in the Fraunhofer region, will generate an angular distribution of constructive plane waves. Essentially, light

1 $\lambda = 1030nm$ and $\tau = 370fs$ pulse duration and 120 kHz.

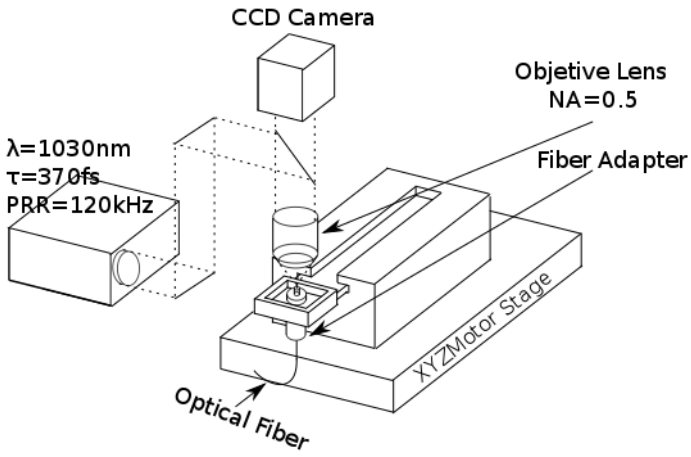

Figure 50: Set-up diagram for end-fiber writing.

emerging from diffraction gratings will exhibit different propagation angles, which are fundamentally dependent on the grating period Λ, the wavelength of incident wave λ and the number of diffraction order m. This distribution can be obtained using the Fraunhofer diffraction equation [138]

$$\Lambda(\sin(\alpha) - \sin(\beta_m)) = m\lambda, \tag{90}$$

where β_m and α are the propagation and incidence angles, respectively.

In this section a proof of concept at the fiber surface of a SMF will be performed. The same pattern will be inscribed below the surface, increasing its mechanic resistance and allowing tilted inscription. The inscription below end-fiber will be performed in MMF as will be discussed later, exhibiting higher diffraction efficiency. Finally, this process will be extended to POFs, where the manufacturing processes and the achieved results will be analyzed.

6.2.1 SURFACE

The writing setup cited in section 6.1 is used to inscribe simple diffractive elements at fiber end-face. The diffraction gratings were inscribed at 0.06mm/s and 310nJ pulse energy. The scheme of the resulting binary phase grating is depicted in Fig. 51.a. The inscription consist of ten rectangular air holes of thickness $d = 2.30(21)$ (Type III) with period $a = 3.95(23)\mu m$. A image of performed inscription captured by a CCD camera is depicted in Fig. 51.b An HP 8168F tunable laser source working at 1550nm illuminates the fiber in order to characterize the output diffraction pattern. A Hamamatsu vidicon camera with FFP optics[2] captures the profile detailed in Fig. 51.c. It exhibits high quality, good symmetry and expected intensity distribution with one visible diffraction order placed at $\beta_1 = 22.23(11)^\circ$ as depicted in Fig. 52.

Following grating Eq. 90 for normal incidence, first order maximum should be placed at $\beta_1 = 23.1(1.4)^\circ$. Being both theoretical and experimental measurements consistent quantitatively verifies that measured FFP follows expected diffractive pattern. The NA has

2 In this setup, the image is formed with a system analogous to the emission angle distribution projected on the screen on the hemisphere which has the luminous point as its center.

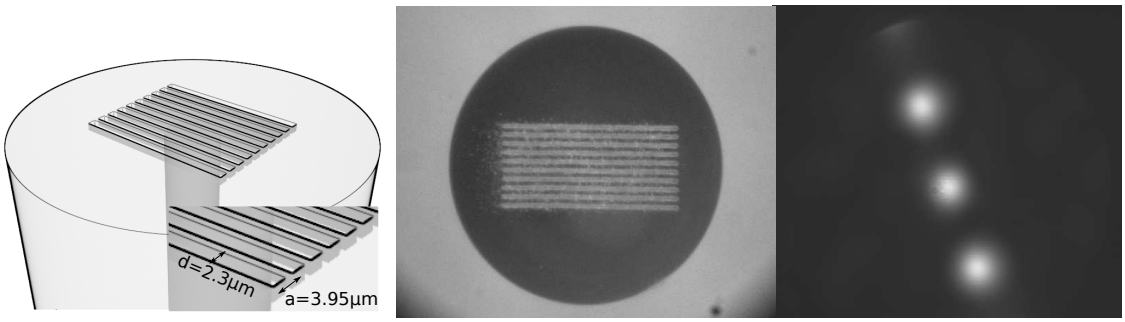

(a) (b) (c)

Figure 51: Scheme of 1-D diffraction grating at fiber end-face with period $\Lambda = 3.95(23)\mu m$ and thickness $d = 2.30(21)\mu m$ (a), CCD image of resulting 1-D diffraction grating inscription (b) and its FFP distribution from a 1550 nm laser source (c).

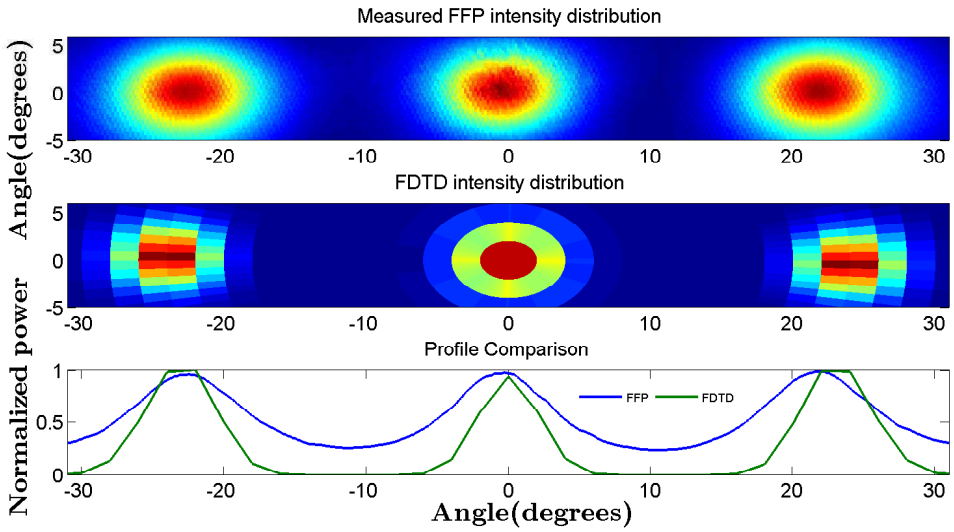

Figure 52: Scheme of 1-D diffraction grating at fiber end-face with period $\Lambda = 3.95(23)\mu m$ and thickness $d = 2.30(21)\mu m$ (a), CCD image of resulting 1-D diffraction grating inscription (b) and its FFP distribution from a 1550 nm laser source (c).

also been characterized at $1/e^2$ of intensity decay, exhibiting a NA=0.169 compared to NA=0.192 of an uninscribed SMF28 which is a decay of 12%[3]. This structure can be easily simulated with FDTD assuming an infinite cladding. The hole depth is set a free parameter to run several simulations in order to fit normalized power. First value to fit was 1.2μm which is a very reasonable value for given pulse energy. Fig. 52 exhibits both FFP and FDTD intensity distribution with their respective linear profile confirming angular position and diffractive efficiency agreement.

3 This is attributed to an effective index reduction of both core and cladding as a consequence of laser ablation. The numerical aperture of step-index fibers depends on the RI of both core and cladding. Assuming they exhibit the same reduction and writing the new effective index as $n_i^{eff} = n_i - n_h$, being n_h the RI reduction, the NA is

$$NA = \sqrt{(n_1^{eff})^2 - (n_2^{eff})^2} = \sqrt{(n_1 - n_h)^2 - (n_1 - n_h)^2} = \sqrt{n_1^2 - n_2^2 - 2 * n_h(n_1 - n_2)}, \quad (91)$$

which is lower than the original NA.

6.2.2 INSCRIPTION IN THE BULK OF OPTICAL FIBERS

When inscription is placed few microns below the fiber end-face surface, the complexity of the structure increases, being harder to characterize. However, its mechanical resistance improves. In the surface inscription, removal of the fiber from the bare fiber adapter may distort the pattern; this makes necessary cleaving the fiber to remove by the other side of the adapter and the fusing the fiber again, which is an added complexity.

In addition to mechanical resistance enhancement, inscription below surface allows tilt writing i.e. the incidence angle α (from Eq. 90) can be controlled[4]. The Fig. 53.a depicts this parameter for a diffraction grating inside the optical fiber. Diffraction grating thickness is assumed to be $d << \Lambda$ in order to consider the problem as a linear system with a linear input consisting in the product of a light distribution function and a transmission/phase function. When $d >> \Lambda$, the diffraction grating can no longer be regarded as a simple aperture function and beam propagation through the diffraction grating must be studied. Inscription with femtosecond lasers exhibits an intrinsic longitude parallel to the laser pulse propagation due to the filamentation process, besides, when fluence reaches a certain threshold highly dependent on laser parameters [73], the index change becomes inhomogeneous, exhibiting both positive and negative index change. These properties, inherent to femtosecond laser processing, prevent the diffraction grating from being regarded as thin. However, there are also other factors that have an influence on the grating modeling besides structure features: the incident wave cannot be considered a plane-wave and propagation until the fiber end-face may not be regarded as free space propagation either. These details make necessary a deeper study of the structure to model these remarkable features adequately. Coupled-wave theory is usually used to calculate these parameters. However, as the emerging mode still must propagate tenths of microns before exiting the optical fiber, the BPM offers a more versatile approach to simulate these structures. After obtaining a more precise model of the inscribed diffraction grating in terms of the refractive index change, this simulation method will be employed to predict the order angle β_m and establish a comparison with Eq. 90 and then possible deviations caused by diffraction order propagation in the optical fiber.

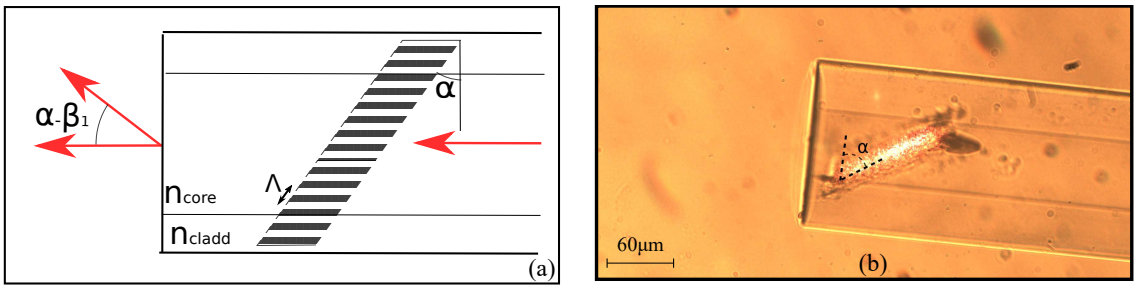

Figure 53: Diagram of tilted diffraction grating inside of the optical fiber (a). Capture of the inscribed diffraction grating by transmission microscope (b). Optical fiber was illuminated by a red laser source and immersed in index matching oil.

4 In the previous inscription, the surface determines the incidence angle, Plastic Optical Fibers (POF) are easy to cleave in any desired way, but standard telecom optical fibers made of glass require a tilt cleave via special processing [177].

After explaining some remarkable features of the possible implemented devices, the manufacturing process is detailed. The pulse energy employed is 0.31μJ focused 60μm below the end-face surface with different tilts from $\alpha = 0°$ to $\alpha = 65°$. Fig. 53.b depicts an example of tilted diffraction grating captured with a transmission microscope for a MMF with core distance $d_c = 62.5\mu m$ and $\alpha = 60°$, where a thickness of $d = 10.2(2.0)\mu m$ has been measured.

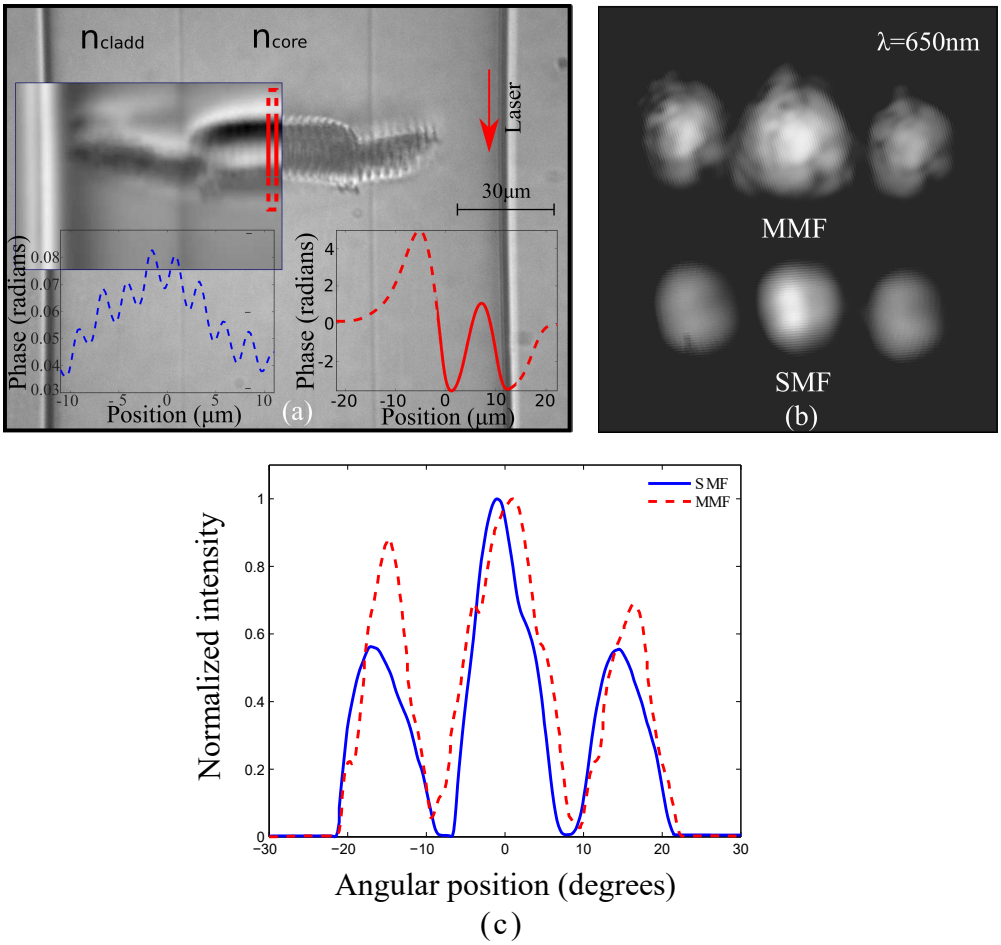

Figure 54: Inscription of 60 μm below end-face, the inserted image corresponds to a QPm image (being black and white colors negative and positive phase respectively). Dashed blue line corresponds to a transversal profile of cross section QPm image (not shown here). Red line correspond the longitudinal phase profile of red section (a). FFP of SMF and MMF for $\alpha = 0$ and $\Lambda = 2.5\mu m$ at $\lambda = 650nm$, MMF exhibit a typical speckle pattern and SMF present a modal overlapping due to a working wavelength below monomode regime (b). Normalized intensity profile of both patterns, MMF diffraction orders exhibit higher intensity(c).

For the particular case $\alpha = 0°$ some structure properties are easily noticed. A phase study will be performed in order to analyze the refractive index change along the inscription. The QPm technique performs the characterization employing $\pm 3\mu m$ defocusing and the same objective than in the manufacturing stage. The in-focus image and the resulting phase image of a typical diffraction grating inscribed in an optical fiber submerged in index matching liquid is depicted in Fig. 54.a. From the intensity image, the shape

difference between core and cladding can be appreciated, being the core grating thicker than the cladding which exhibits a minor tilt. This effect is mainly due to different composition and aberrations caused by a cylindrical shape. Germanium dopants at the core may change both damage threshold and viscosity, resulting in a different inscription shape with different phase changes. On the other hand, when the light focuses inside and near the border, the light cone is not entirely transversally immersed and the focal volume shifts above. This phenomenon explains the slight tilt that noticed in the cladding inscription. A transversal phase profile (Fig. 54.a dashed line) has also been obtained from a cross-section phase image (not shown here). It exhibits a sinusoidal phase variation of very low amplitude due to the high index contrast between the air-fiber interface. The depicted phase image in Fig. 54.a provides a more precise profile. Here, the red section in the phase image indicates the position of the profile below with respect to the image. There are two types of lines in the profile; the solid line represents the focal volume, where the periodic index change is located. The dashed line corresponds to the zones in the vicinity of focal volume, whose refractive index has changed as a consequence of property changes in order to reach the local equilibrium. Two strong negative phase changes ($\Delta\phi = -3.55$) can be noticed within the focal volume, represented as black and gray colors in the phase image (Fig. 54.a). The outer zones (dashed lines) surrounding the grating exhibit different phase changes. These zones are caused by elastic stress of the opposite direction as a result of the accommodation of displaced material from the permanent strain induced at the focal volume to reach local equilibrium. The above positive change exhibits an extreme phase change ($\Delta\phi = 4.95$) despite not being produced at the focal volume. Overall, assuming a homogeneous index change normal to Fig. 54.a in a length equal to the core diameter, the index change can be estimated as $\Delta n = (\Delta\phi\lambda)/(2\pi z)$ giving an averaged $\Delta n_{pos} \approx 7 \times 10^{-3}$ and $\Delta n_{neg} \approx 5 \times 10^{-3}$. The periodic phase variation obtained from the same phase image can be noticed in the focal volume region and being lower than the average phase change, complicating its profile retrieval.

From the data obtained through QPm, the analyzed structure was simulated using a module of the commercial software Rsoft based on BPM. Grating geometry was simplified as two 50 μm consecutive long negative index change slabs generating a step index variation. The primary purpose of the simulations is to study the order behavior with tilt angle α.

After the manufacturing and characterization stages, a performance study has been carried out by capturing the diffraction grating patterns at the Fraunhofer region with the vidicon camera. The commercial software Lepas-11 analyces this later FFP.

The first task is to compare patterns from a SMF and a MMF. Multimode fibers, have been considered more suitable for diffraction grating inscription due to higher NA and core diameter, which allows far more lines inscribed at the core, increasing grating efficiency. Fig. 54.b depicts FFP for both SMF and MMF perpendicular diffraction gratings ($\alpha = 0°$) at $\lambda = 650nm$. MMF orders are wider than SMF thanks to their higher NA, and they display the usual speckle pattern attributed to the interference of many propagation modes [178]. SMF orders also display slightly multimodal behavior as the operating wavelength is below monomode regime ($N_{SMF} \approx 10$ compared to $N_{MMF} \approx 270$). The Intensity profile of Fig. 54.c exhibits higher diffraction efficiency for MMF, confirming prior assumptions.

After analyzing the diffraction efficiency of both tested fibers, the angles of each diffraction order have also been analyzed. The control of order angles is decisive to determine the best device configuration depending on the sensing purpose. In this way, the order

angle β_m has been studied in terms of tilt angle α. Fig. 55.a shows different diffraction order positions in function of tilt angle α for $\lambda = 650nm$ and $\Lambda = 2.5\mu m$. Dashed lines are theoretical values provided by Eq. 90 and solid lines are order three polynomial fit of simulation results employing the structure mentioned above. For lower tilt angles, Eq. 90 and simulations are in good agreement; however, there are deviations with an increase of α for high order numbers. This is caused by the order propagation inside the optical fiber and the assumption in Eq. 90 of plane wave incidence that can explain how -2 and -1 orders disappear sooner in simulations than theoretical restriction.

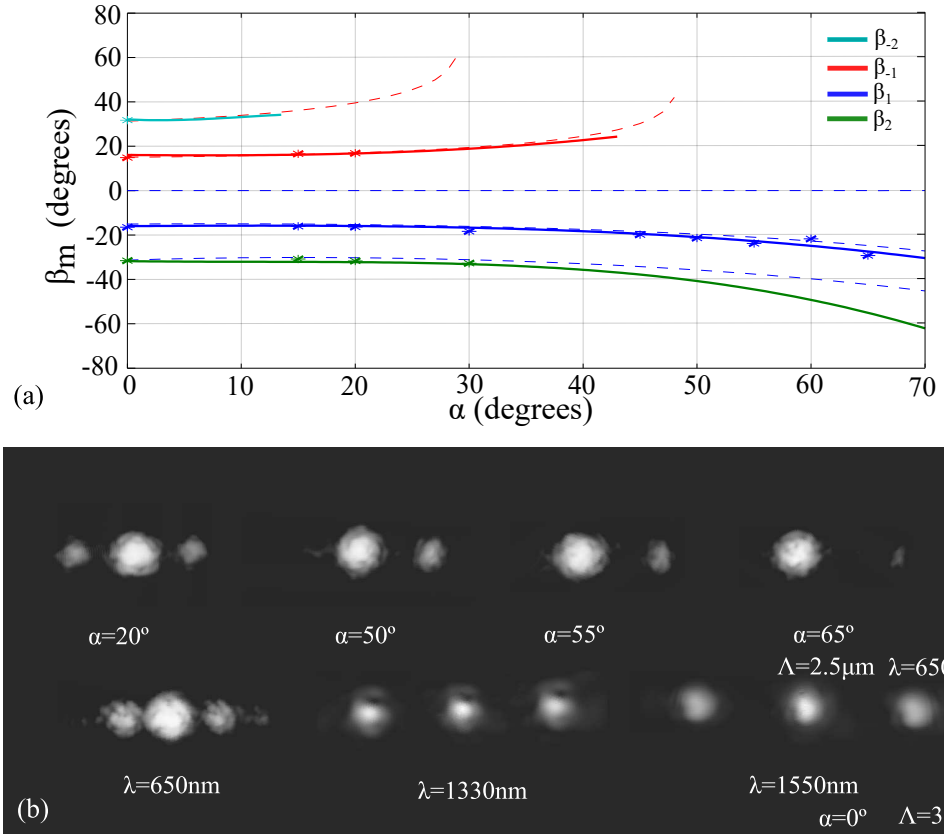

Figure 55: Study of grating angle dependence α with angle order β_m. Dashed lines represent theoretical position following Eq. 90, solid lines represent simulation results while dots represent experimental measurements (a). FFP for different parameters. First line corresponds to $\Lambda = 2.5\mu m$ and $\lambda = 650nm$ gratings with α ranging from 0-65°. Second line corresponds to $\Lambda = 3\mu m$ and $\alpha = 0°$ with wavelengths ranging from 650-1550nm (b).

Dots in Fig. 55.a represent the experimental measurements which exhibit a good agreement with simulations for the 1st order. Simulated data for the 2nd is also computed despite the low diffraction efficiency that makes impossible its measurement for $\alpha > 30°$. Negative orders are filtered sooner for the same reason, disappearing for $\alpha > 20°$. However, there are still order remnants in FFP, as shown on the first line (top) of Fig. 55.b. Only a slight trace of the 1st negative order can be appreciated at $\alpha = 50°$. When the tilt angle increases, the diffraction efficiency of the 1st positive order decreases. Also, the second line (bottom) depicts the FFP of the same diffraction grating at different wavelengths. The angle order linearly increases with wavelength as expected from Eq. 90 the second line its behavior at different wavelengths is shown in the second line of the same figure.

6.2.3 IN POLYMER OPTICAL FIBERS

Polymer Optical Fibers (POFs) based on PMMA have desirable characteristics and optical properties in communications of short distances and industrial applications. In recent years, numerous devices and components have been made based on POF of 1 mm in diameter. Having a diffraction grating in the structure of a POF can allow increasing its applications whether in communications, sensors or as simple, miniaturized devices. The inscription of diffraction gratings in POF exhibit some advantages respect to their silica counterpart. The first advantage is the obvious increase in the amount of diffracted light caused by an increase in both diffraction efficiency[5] and NA. The second advantage is the simplicity required for cleaving the fiber in any desired shape, thus controlling α without the need of inscription below fiber. Finally, POFs, due to its size and material, are more mechanically resistant than conventional fiber and hence, the inscribed diffraction grating can withstand a decent amount of interaction without the ereasing pattern.

In a multimode optical fiber, as in the case of a step-index POF of 1mm diameter, all propagated modes participate in the diffraction phenomenon if the grating is normal to the incident beam ($\alpha = 0°$). This arrangement generates symmetric diffraction orders and a weak angular separation between orders if the period Λ is large ($\Lambda \geqslant 2\mu m$) in the case of visible light. This arrangement of the diffraction grating on fiber has no practical applications in sensors or communications, so it is required to have very few diffraction orders and spatial separation between as large as possible. This can be performed by α control as explained in the previous section. The fiber ends at an angle while reducing the number of modes, consequently reducing the modal dispersion and increasing the number of lines of the diffraction grating by increasing the output surface. In previous works, considering the same type of POF, it was determined that the most convenient angle to have only two diffraction orders for visible light was $\alpha = 55°$ for $\Lambda = 2\mu m$ [138].

In order to manufacture the proposed design, the fiber holder of the inscription setup has been substituted by a PMMA block with a drilled hole at an angle α to place the POF with its end-face perpendicular to objective lens optical axis. Proper illumination of the sample has been achieved by illuminating opposing end-face with a white light source (depicted in Fig. 56.a). The fiber used is a step-index of 1 mm diameter (980/1000 μm), NA = 0.5 and $n_1 = 1.49$. Tilt end-face has been achieved by regular polishing at a desired angle. The diffraction grating has been manufactured by inscribing lines focused at the end-face surface at 0.2mm/s writing speed and 0.11μJ pulse energy perpendicular to the semi-major axis of the end-face ellipse with $\Lambda = 2(0.1)\mu m$. Three diffraction gratings were manufactured with tilts 0°, 30° and 55°. Fig. 56.b depicts an inscription example exhibiting surface periodic modification. Besides, Fig .56.c also shows the polishing result of the three diffraction gratings.

Once manufactured, the intensity distribution at Fraunhofer region of diffraction gratings has been performed by the vidicon camera. Fig. 57 depicts these patterns at $\lambda = 650nm$. For $\alpha = 0°$ diffraction orders exhibit low efficiency, being difficult to resolve from background noise. The result is an elliptical field surrounding "0" order which has the same shape as its raw counterpart. When the tilt is increased up to 30°, diffraction orders are resolved having "-1" order more diffraction efficiency than its symmetrical counterpart

5 The diffraction efficiency depends on the number of grooves in the grating and the diameter of the incident beam section.

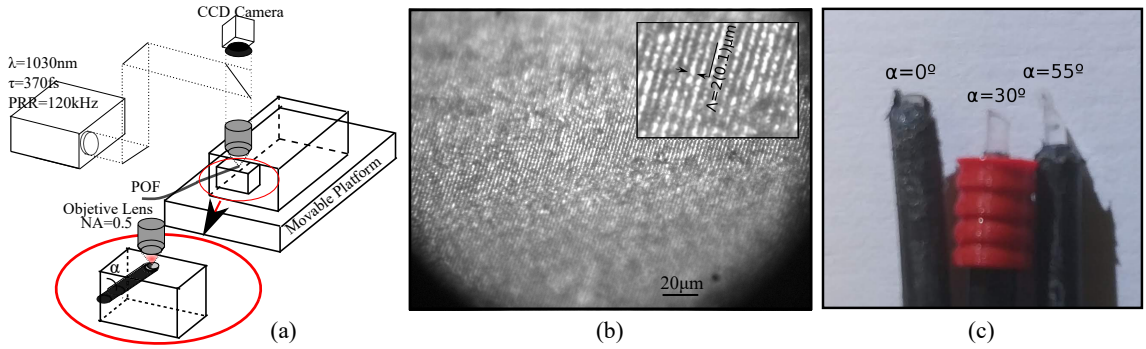

Figure 56: Manufacturing stage. (a) depicts the schemtatic setup for grating inscription while (b) shows a capture of processed end-face with $\Lambda = 2(0.1)\mu m$ and $\alpha = 55°$.

and an angular separation $\Delta\beta = 32(1)°$. This tendency increases at $\alpha = 55°$ where positive orders are not present and exhibit $\Delta\beta = 31(1)°$.

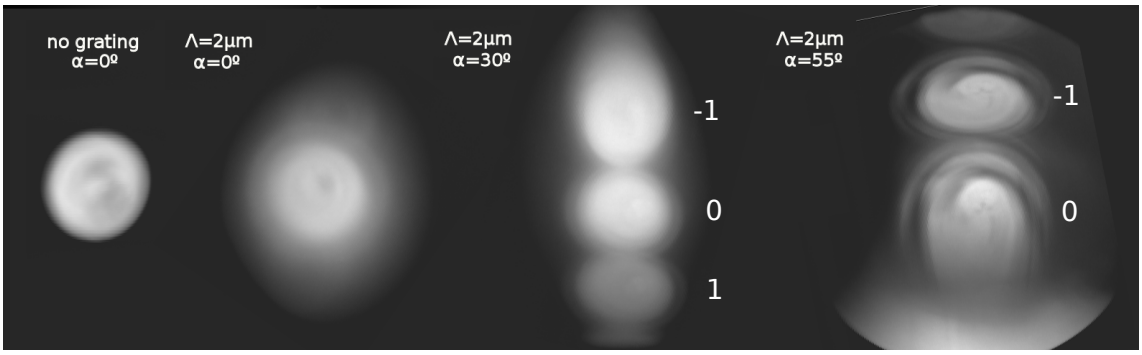

Figure 57: FFP for different diffraction gratings ($\Lambda = 2(0.1)\mu m$) at different tilt angle α. All samples were illuminated by a LED source with $\lambda = 650nm$.

6.3 2D DIFFRACTION GRATINGS

Now that several efforts have been invested in the characterization of 1-D diffraction gratings, in this section, their 2-dimensional counterpart will be introduced as a way to extend their application to several axes. These kinds of structures allow the measurement of new parameters due to the high amount of degrees of freedom in their structural design. Their application as 2D displacement insensitive tilt sensor will illustrate said potential. The study also extends to MCF where its effect on the unperturbed interference pattern will be characterized and also employed for vectorial bending sensing.

In a simple way, the proposed fiber-based structures can be modeled employing mainly two phenomena: diffraction and interference. Apart from the deviations introduced by the manufacturing process, the specific properties of each structure can be explained using a combination of these phenomena. Particularly, the structures based on single core fibers, where only a surface grating is inscribed, are mainly driven by diffraction. On the contrary, when fibers with different cores are employed, both interference and diffraction must be analyzed.

The diffraction grating modeling, as explained in previous sections, can be simplified using an incident plane wave into a screen with a periodic perturbation. In this case, each perturbation will form an individual Fraunhofer pattern with a fixed phase relation respect the others. These phase relations determine positions where constructive interference prevails, and the grating equation can predict them.

The diffraction grating modeling, as explained in previous sections, can be predicted by the grating equation 90. In section 6.2.1, 1-D diffraction gratings were already written at the end-face surface. This writing can be extensible to bidimensional patterns by exploiting the PRR and writing speed of lasers to apply the PbP technique (employed in previous chapter for grating inscription) to diffraction pattern.

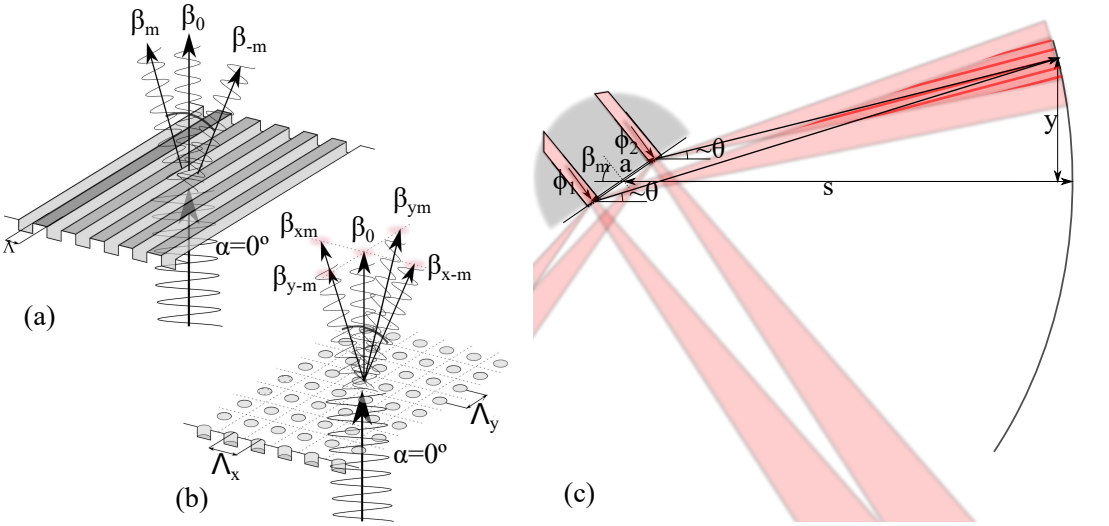

Figure 58: Diagram of 1D diffraction grating (a) and PbP diffraction grating (b). Diagram of interference of two waveguides with a diffraction grating at their exit (c).

Where α is the incidence angle of the incident wave, β_m the angle of m-th diffraction order and Λ the perturbation period which can be a phase, amplitude or both change, when femtosecond laser pulses ablates optical fiber end-face surface, an air gap is created that produces a phase difference that can act as aforementioned perturbation. In this sense, diffraction gratings can be manufactured by inscribing parallel lines with period Λ as depicted in Fig. 58.a where structure periodicity gives one direction where phase relation follows Eq. 90. This procedure can be extensible to bidimensional patterns by exploiting the PRR and writing speed of lasers to apply the PbP technique to diffraction pattern. The result of this method resembles Fig. 58.b, a bidimensional array of holes of period Λ_x and Λ_y resulting in a FFP with diffraction orders in two directions. This pattern is analogous to the inscription of periodic lines in two different directions with periods Λ_x and Λ_y as are complementary patterns following Babinet's principle [179].

The emerging light from the different cores of a MCF illuminated by a light source interfere with each other giving an interference pattern. For an axis with two cores separated by a distance a, the intensity pattern in a planar screen placed at a distance $s >> a$ is represented by

$$I = 4I_0 \cos^2\left(\frac{y a \pi}{s\lambda} + \Delta\phi/2\right), \tag{92}$$

which resembles Young's interference except for the term $\Delta\phi$ that represents core phase difference. This term stems from intrinsic and extrinsic perturbations that alter mode effective index of different cores differently.

When a diffraction grating is inscribed at the end face of a MCF, each inscribed core projects a diffraction pattern that overlaps causing an interference pattern as depicted in Fig. 58.c for a spherical screen and small angles $\theta \approx y/s$. The intensity pattern of the m-th order can be approximated to

$$I \approx 4I_0 \cos^2\left(\frac{a\pi}{\lambda}(\sin\beta_m + \cos\beta_m\theta) + \Delta\phi/2\right). \tag{93}$$

From this equation, fringe maxima are placed at

$$\theta_n = \frac{\lambda(n\pi - \Delta\phi/2)}{\pi a\cos\beta_m} - \tan\beta_m, \tag{94}$$

being n an integer n=1,2,... The fringe period is deduced as $\Lambda_{\beta_m} = \lambda/a\cos\beta_m$. This implies that the fringe period increases with grating angle β_m. The dip shift with phase variation is determined by

$$d\theta_m = -\frac{\lambda}{2\pi a\cos\beta_m}d\Delta\phi = -\frac{\Lambda_{\beta m}}{2\pi}d\Delta\phi. \tag{95}$$

The variation is linear and depends on angle order as well as period, this kind of fringe patterns with the capability of being modulated by phase change can be used in a wide variety of scenarios such as sensing or even Spatial Frequency Domain Imaging (SFDI) [8].

Based on the above explanations, regular lines and PbP lines will be inscribed at the end-face of both SMF and MCF in order to observe their FFP and measure their order disposition and interference behavior. Particularly, ehe SMF is a standard telecom SMF28 of 9 μm core diameter and a MCF model SM-4C1500(8.0/125) with four single mode cores forming a concentric square of vertex $l = 36.25\mu m$ of the company Fibercore Inc.

Lines were inscribed at 120kHz PRR, 0.19μJ pulse energy and 0.1mm/s writing speed. The PbP technique was achieved with the same method than section 5.3.2, delivering 20 pulses per point at the same energy and writing speed than lines.

An example of the manufactured devices is depicted in Fig. 59. Particularly, in Fig. 59.a a continuous line 1-D diffraction grating of $\Lambda = 3\mu m$ written with aforementioned parameters is depicted. In Fig. 59.b, a PbP 2-D grating with periods $\Lambda_x = \Lambda_y = 3\mu m$ is shown. It is quite noteworthy the random offset that point grid exhibits, this is caused by the precision of the translation stage. The two different approaches have been all employed in the MCF by inscribing PbP 2-D gratings in two cores (Fig. 59.c) with periods $\Lambda_x = \Lambda_y = 3\mu m$ and a *circular* grating with a period of $\Lambda_c = 3\mu m$ in the 4 cores (Fig. 59.d). Their FFPs have been analyzed in order to determine their performance as sensing elements. Images were adequately captured at Fraunhofer regime while fibers were illuminated with a 1550nm laser source. Examples of the FFP launched by each configuration (Fig. 59) are depicted in Fig. 60: 1D grating into single-core fiber (a), 2D grating inscribed with PbP technique into single-core fiber (b); 2D gratings inscribed with PbP technique into two cores (c); *circular* grating inscribed into 4 cores.

Overall, all the patterns exhibit good shape even without additional postprocessing techniques. In Fig. 60.a, the one axis diffraction orders of the inscribed 1D grating can be noticed. Particularly, the output angle of first orders $\beta_{\pm 1} \approx 30°$ is consistent with Eq. 90 for a period of $\Lambda = 3\mu m$. The 2D grating inscribed into a single core fiber using the PbP

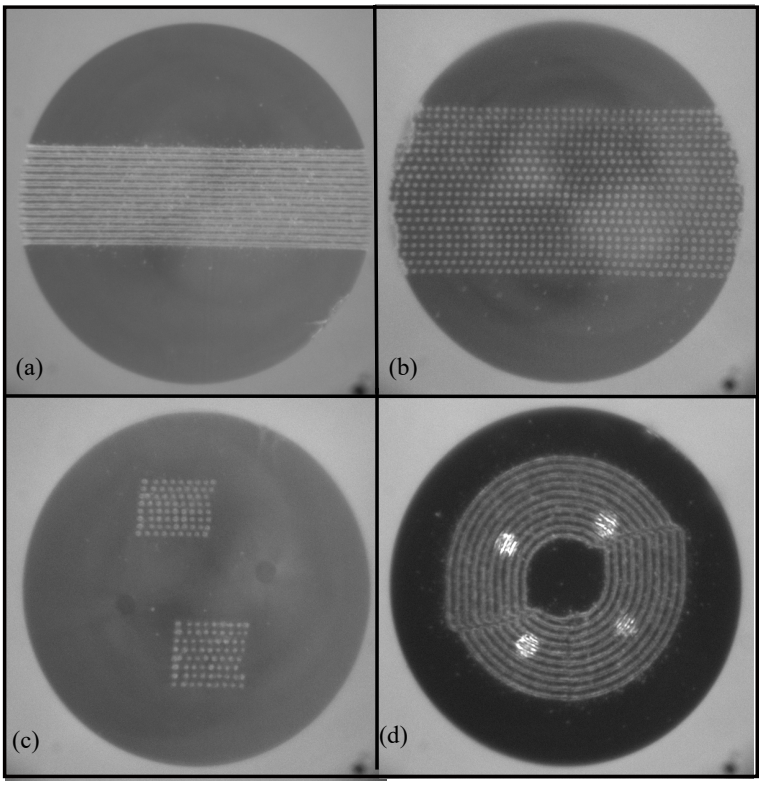

Figure 59: Inscription results for 1D diffraction grating (a), 2D diffraction grating (pbp technique) (b), same technique in 2 cores of multicore fiber (c) and circular grating for the same fiber (d).

technique (Fig. 59.b) exhibits a more complex behavior where one can notice a perfect defined diffraction order at one direction (perpendicular with writing direction) and a more diffused one at the other direction. This diffused diffraction order exhibits two lobes, one brighter than the other. Such behavior is caused by the random distribution of period offset caused during the manufacturing process. The resulting FFP of each point exhibit a small random phase in addition to the fixed phase relation in the direction parallel to the inscription. From the order shape one can notice that the random offset disposes of the point grid in two predominant directions, one perpendicular to writing direction and another with a slight tilt from the previous one, being more predominant the later.

In the multicore fiber, both analog approaches have also been employed; The output pattern of a PbP 2D grating inscribed into two different cores of a MCF (Fig. 60.c); combining the 2D diffraction with the interference of two similar waveguides as expected from Eq. 90 and 93 for zero and first diffraction orders respectively. As inscription has only been performed in two of the four cores, the diffraction orders exhibit a 1 Dimensional interference pattern as opposed to zero order, where the other two remaining cores produce a two-dimensional interference pattern. This also implies that interference patterns of diffraction orders in both directions are essentially the same. This behavior is the opposite than the *circular* grating inscription. Here, the circular geometry allows the simultaneous inscription in each core but reducing interference effect only with opposite cores. The FFP depicted in Fig. 60.d shows that diffraction orders of both directions exhibit perpendicular and independent diffraction patterns.

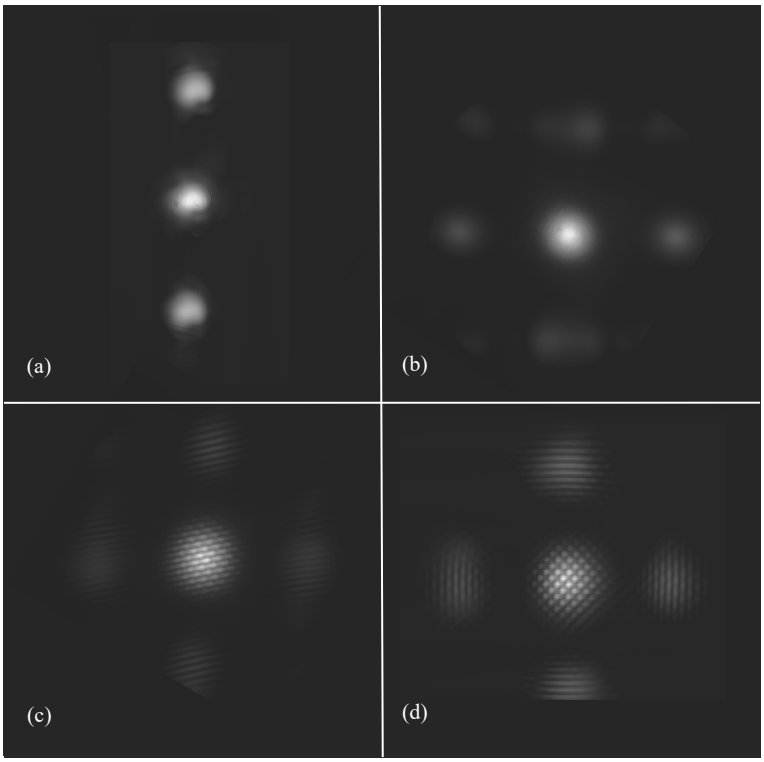

Figure 60: Resulting FFPs of the inscriptions depicted in Fig. 59.

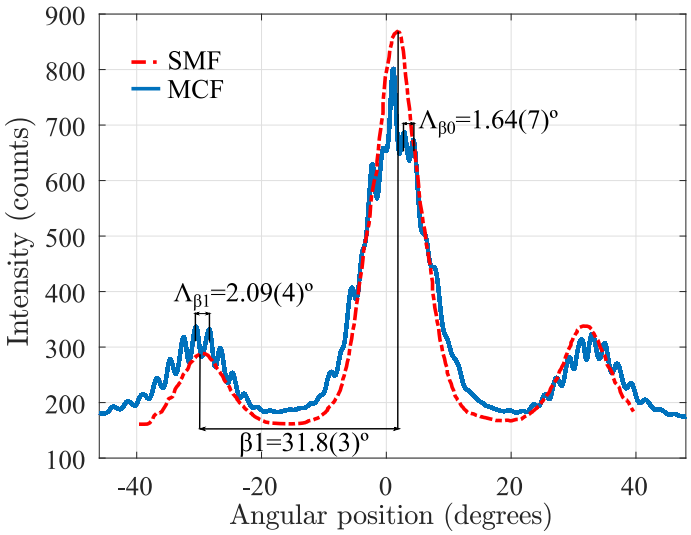

Figure 61: FFP profile of diffraction grating inscribed in both SMF and MCF.

A detailed profile of an axial projection of the FFP launched by the MCF with *circular* grating and SMF with PbP grating is depicted in Fig. 61. The influence of the interference can be noticed into the fringe exhibited by the profile. Measured period $\Lambda_{\beta 0} = 1.64°$ and $\Lambda_{\beta 1} = 2.09°$ for zero and first diffraction order are in good agreement with their theoretical

counterparts $\Lambda_{t\beta 0} = 1.73°$ and $\Lambda_{t\beta 1} = 2.04°$. This fringe pattern can be employed to analyze variations between the different cores of the same MCF (as described in Eq. 95).

Based on the different phenomena that are present on each inscribed device, they can be employed as both extrinsic and intrinsic sensors by analyzing their FFP, being each configuration sensitive to different perturbations.

6.4 APPLICATIONS

Once the diffraction grating has been characterized and knowing order location in function of tilt for several fiber types and patterns, diffraction gratings can be designed for a specific application. In this section, some of the inscribed configurations will be employed for sensing. Particularly, the sensing parameters are temperature, displacement, tilt, and bending. Besides, wavelength demultiplexing will also be proposed.

Both temperature and displacement sensing will employ a tilt MMF given their requirement of only one diffraction order. In contrast, tilt and bending will be measured by a 2D diffraction grating allowing vector measurements. Displacement and tilt are good examples of measurable magnitudes extrinsic to the fiber while temperature and bending are intrinsic to the fiber. These three magnitudes are good examples of the sensing potential that these patterns can offer.

6.4.1 TEMPERATURE

In order to measure temperature, a diffraction grating with $\alpha = 60°$ and $\Lambda = 2.5\mu m$ has been inscribed in a MMF with $d_c = 100\mu m$ and placed into an aluminum base with a peltier plate above, as detailed in Fig. 62.a. The Cooling surface is in contact with a thermal pad from Artic placed above an aluminum base in order to avoid the cooling to interfere with the measurements. The heating surface placed at the top has another thermal pad to couple heat to the fiber end-face as homogeneous as possible. This fiber is protected from the ambient with an isolator material to avoid heat flux that could alter actual grating temperature from measured temperature as possible.

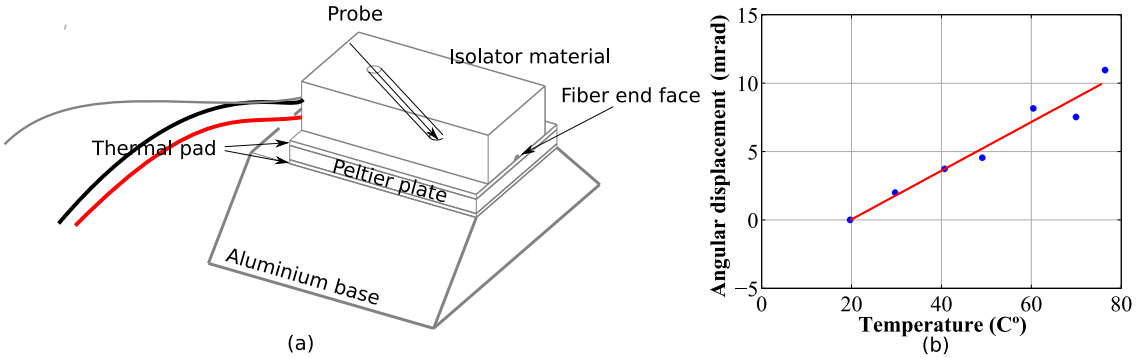

Figure 62: Setup for temperature measurement (a). Experimental results of the first order displacement vs temperature (b).

The isolator has two holes, a small one to introduce a thermistor that measures the temperature and a tiny one that allows the output light from the fiber to reach the screen.

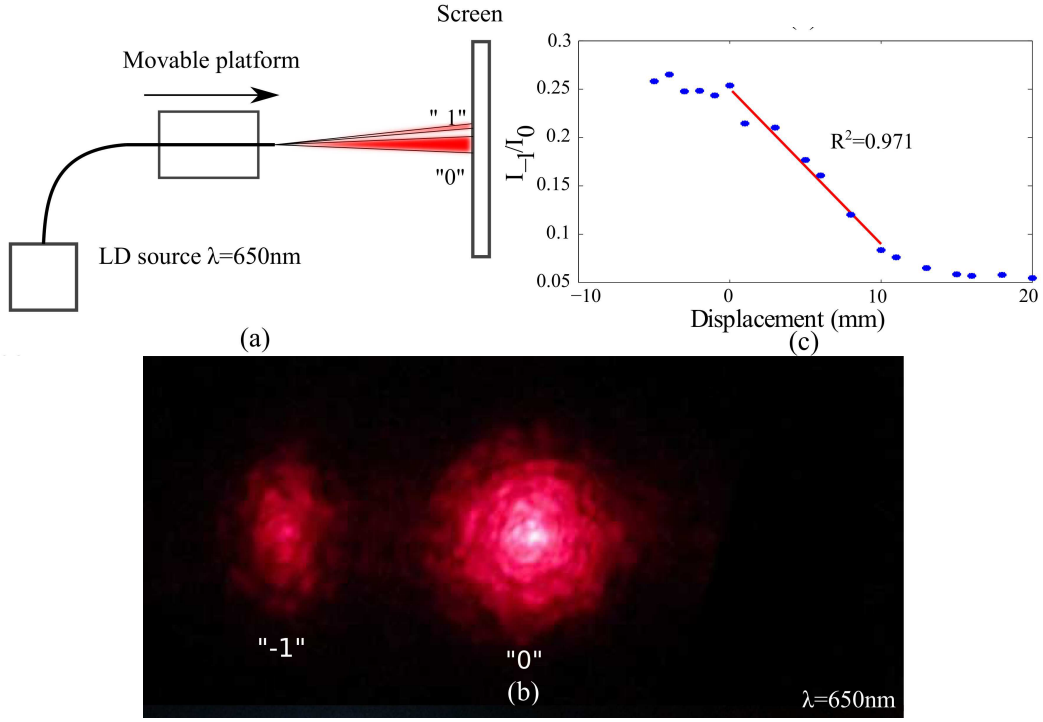

Figure 63: Setup for displacement measuring (a). The diffraction grating is placed into a movable platform illuminated with a LD source ($\lambda = 650nm$), the patter manifests in a screen (b) placed at a known distance and captured by a digital camera. Results are plotted in (c).

A temperature controller connected to the thermistor modulates input voltage of the peltier plate to stabilize temperature.

The aluminum base placed at 3.1cm from a screen and illuminated with the same $\lambda_r = 650nm$ source, generates a diffraction pattern captured with a digital camera. The temperature has been measured in steps of 5°C up to 75°C, the first order position has been recorded in all the cases by making a binary capture and extracting the centroid and calculating its angular displacement. The experimental results are depicted in Fig. 62.b, where angular order separation suffers a linear increment due to a grating compression caused by thermal fiber expansion. Linear dependence is appreciated with an adjusted r squared of 0.9438.

6.4.2 DISPLACEMENT

Applications of intensity sensors, due to the problems of power variations within the source or external disturbances of the optical fiber, it is convenient to have self-referenced measurements. With a diffraction grating, one diffraction order can be used as reference amplitude, thus obtaining a ratio between orders insensitive to intensity fluctuations.

For such purpose, a diffraction grating with $\alpha = 60°$ has been inscribed in a MMF with $d_c = 100\mu m$ and placed into a movable platform at 3.1 cm from a screen. The fiber has been illuminated with $\lambda_r = 650nm$. A digital camera captures the diffraction pattern. Fig. 63.a shows the employed setup and Fig. 63.b depicts the screen pattern. The order intensity has been measured by taking a reference position and setting an adequate threshold for its

corresponding binarized image in order to extract the centroids for both 0th and 1th orders. Two fixed regions of the area captured by the camera have been traced centered in the centroids. These regions behave as individual detectors. Their total count has been used to compute intensity rate I_{-1}/I_0. The result depicted in Fig. 63.c highlights correlation between the displacement and intensity rate , having a linear part from 0 to 10 mm ($R^2 = 0.971$). For 20mm the rate drops to nearly 0 due to the first order almost disappearing for the reference centroid.

6.4.3 TILT

The manufactured 2D surface grating (with $\Lambda_x = \Lambda_y = 2.5\mu m$ in this case) has been employed to measure the tilt angle in both axes, exploiting the 2-dimensional diffraction exhibited by this structure. This pattern may be used for plain surface characterization, providing information about tilt, position, and rotation without interfering with each other. Tilt measurements will be performed by varying the two spherical coordinates angles θ and ϕ as depicted in Fig. 64.

The setup employed to control both angles and locations is depicted in Fig. 64.a, a digital camera is fixed to a rotating screen where the pattern is projected. In this regard, measuring opposing order distance from 0th order and knowing $\beta_{\pm 1}$ allows tilt angle calculation in that axis as detailed in Fig. 64.b, where the following relations

$$d'_{\beta_{\pm 1}} = d_{\beta_{\pm 1}} \cos\varphi \quad z_{\beta_{\pm 1}} = \frac{d'_{\beta_{\pm 1}}}{\tan\beta_{\pm 1}}$$
$$z_{\beta_1} - z_{\beta_{-1}} = \frac{d'_{\beta_1} - d'_{\beta_{-1}}}{\tan\beta_{\pm 1}} = (d_{\beta_1} + d_{\beta_{-1}})\sin\varphi, \tag{96}$$

leads to the equation:

$$\tan\varphi = \frac{d_{\beta_1} - d_{\beta_{-1}}}{(d_{\beta_1} + d_{\beta_{-1}})\tan\beta_{\pm 1}} = \frac{\alpha}{\tan\beta_{\pm 1}}. \tag{97}$$

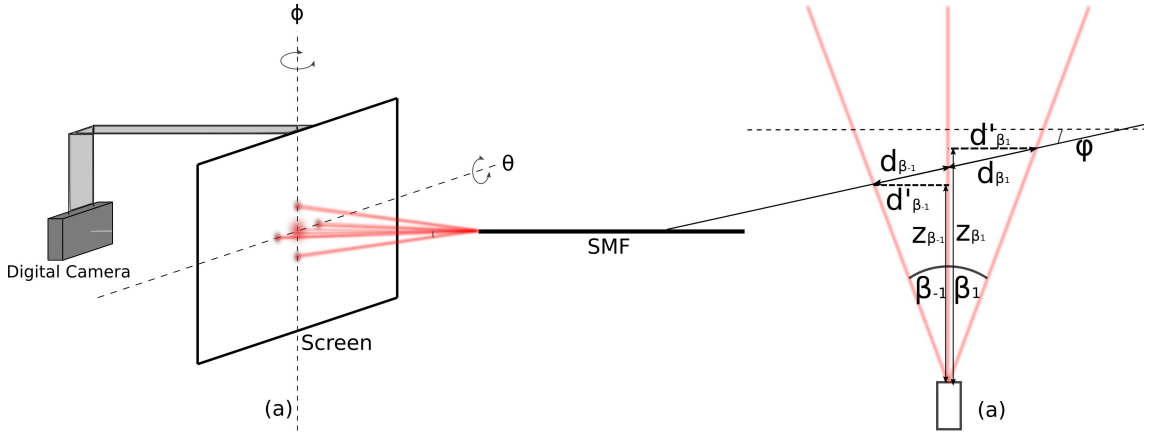

Figure 64: Diagram of tilt measurement setup (a) with a digital camera fixed to a rotating screen for the given angles θ and ϕ. Geometric representation of order displacement when perpendicular tilt applied (b).

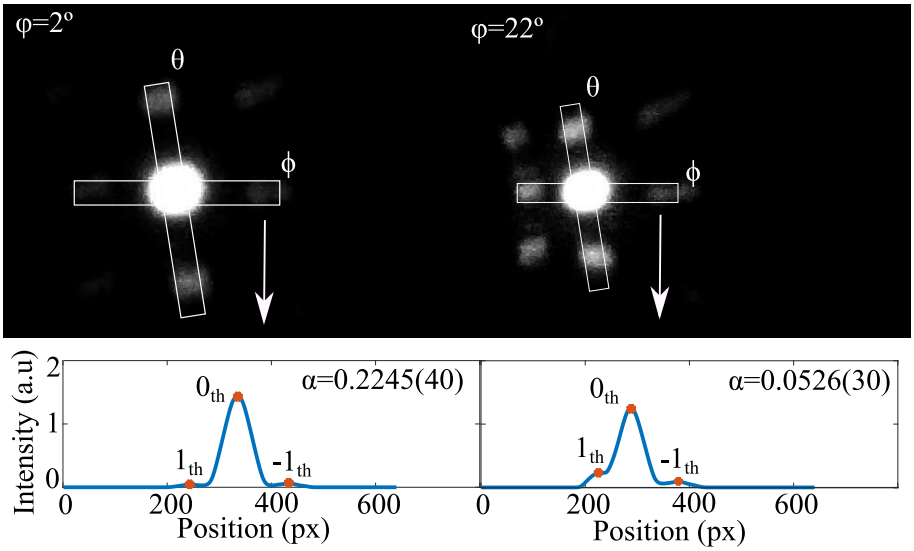

Figure 65: Diffraction pattern for tilts in ϕ angle of $\varphi = 2°$ and $\varphi = 22°$ with their profiles. Order positions are $d_{\beta_1} = 100 \quad d_{\beta_{-1}} = 90$ for $\varphi = 2°$ and $d_{\beta_1} = 90 \quad d_{\beta_{-1}} = 57$ for $\varphi = 22°$.

Here, position has been removed by using the tilt ratio $\alpha = \dfrac{d_{\beta_1} - d_{\beta_{-1}}}{d_{\beta_1} + d_{\beta_{-1}}}$ that relates tilt angle φ and order angle $\beta_{\pm 1}$, resulting in a quantity invariant to plane translations. In this sense, when the studied surface is tilted an angle φ, the order length difference increases or decreases only in function of tilt angle orientation. An example of this length difference is depicted in Fig. 65 where ϕ has been varied giving tilts $\varphi = 2°$ and $\varphi = 22°$ producing order asymmetry in the patterns. They exhibit different order positions ($d_{\beta_1} = 100 \quad d_{\beta_{-1}} = 90$ for $\varphi = 2°$ and $d_{\beta_1} = 90 \quad d_{\beta_{-1}} = 57$ for $\varphi = 2°$) that allow α calculation.

This coefficient has been calculated for several tilts φ by adjusting θ and ϕ. Fig. 66 depicts the tilt ratio (α) vs $\tan\varphi$ curve for θ and ϕ rotations. Both plots exhibit the expected linear behavior with an adjusted r squared and β_1 value of 0.967 and 27.6(2.7)° for

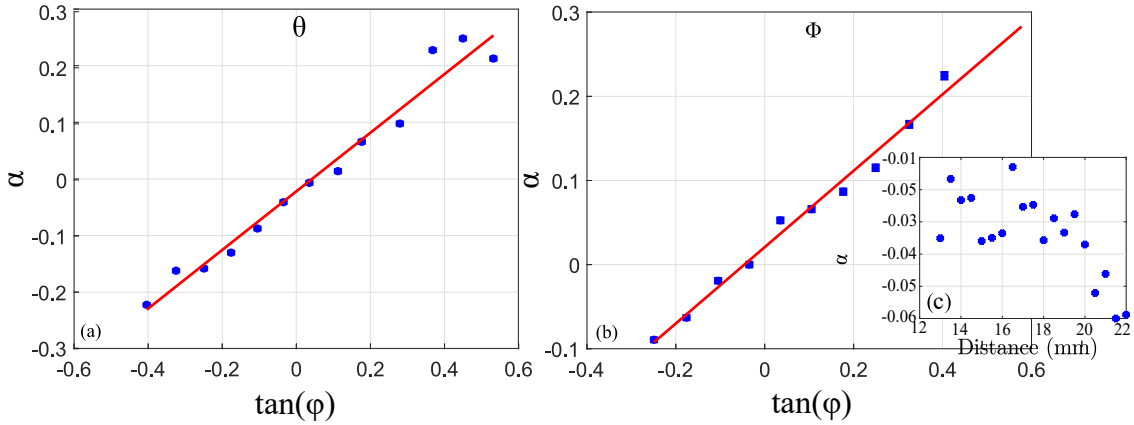

Figure 66: Results from screen rotation in the two spherical coordinates θ (a) and ϕ (b). Both present linear behavior with an adjusted r squared and β_1 value of 0.967, 27.6(2.7)° (a) and 0.983,24.4(2.1)° (b). α measurement for a fixed angle at different distances of the screen. There is a stable noise pattern up to 20mm (c).

θ rotation and 0.983 and 24.4(2.1)° for ϕ rotation. The measured order angle with FFP is consistent with fitted slope, corroborating the performance of two axes of the diffraction pattern and verifying that sensor sensibility is related to $\beta_{\pm 1}$ and therefore the lattice period, being a critical parameter for sensor design. In addition, a proof of concept of sensor behavior with the position has been performed. Despite being theoretically insensitive to displacement variations, the performance of order detection may vary with fiber distance from the screen. The result is depicted in Fig. 66.c, here, the experimental result does not exhibit any expected trend until 20mm; thus they can be understood as noise. For higher distances, result deviates as a consequence of broad and low-intensity diffraction orders. Uncertainty related to noise pattern is $2.1 * 10^{-3}$ rads.

6.4.4 BENDING

MCFs are usually employed for bending sensing through FBG inscription or another point sensing method [180], the proposed sensor measures averaged curvature along the MCF instead of a single point. This feature can be an advantage when the fiber exhibits a major bending and several microcurvatures that could distort the value. In addition, inscribing the transducer structure at fiber-end face instead of bending region does not decrease the fiber mechanical resistance; thus, the dynamic range is longer than other fs inscribed bending sensors.

This sensor employs the dependency of fringe position with phase shift showed in Eq. 94 to measure bending in the entire length of the MCF by measuring the fringe shift as explained in Eq. 95. This is possible thanks to the different effective index change suffered by all the participating fundamental core modes when bending takes place (the sensor is insensitive to uniform index changes such as the ones caused by temperature or strain). The effective index difference through the fiber length generates an OPD in a similar way to an in fiber Mach-Zehnder interferometer where phase variation is defined as

$$d\Delta\phi = \frac{2\pi OPD}{\lambda} = \frac{2\pi d n L}{\lambda}. \tag{98}$$

The effective index change with bending has already been explained in section 4.4.4 and employed in bending sensing in section 5.2.2.2. Here, the same conformal mapping represented in Eq. 87 will be employed for theoretical discussion. This equation applied to a MCF profile suffering bending action parallel to the core axis, as depicted in Fig. 67.a, intuitively shows an effective index decrease to the core mode closer to the bending radio and an index increase to the farthest core mode. Following this approach, a perpendicular bend to core axis does not affect phase difference as both effective indexes suffer the same variation. This principle may be exploited by the studied circular grating structure to achieve vectorial bending sensing. In order to apply bend to the fiber and measure the respective fringe shift, the setup depicted in Fig. 67.b has been developed. Here light was coupled to MCF cores by fusing a multimode fiber with a core diameter of $100\mu m$ illuminated by a light source at $\lambda = 1550nm$. Two points of MCF were fixed (the fiber was tensed in order to prevent any torsion that could lead to cross sensitivity errors) by two platforms at an initial distance before MCF end-face is connected to the vidicom camera. In the first platform rests al the MCF after fusion with MMF and can be displaced by a micrometric screw. When a displacement towards fixed platform reduces L_f a quantity x,

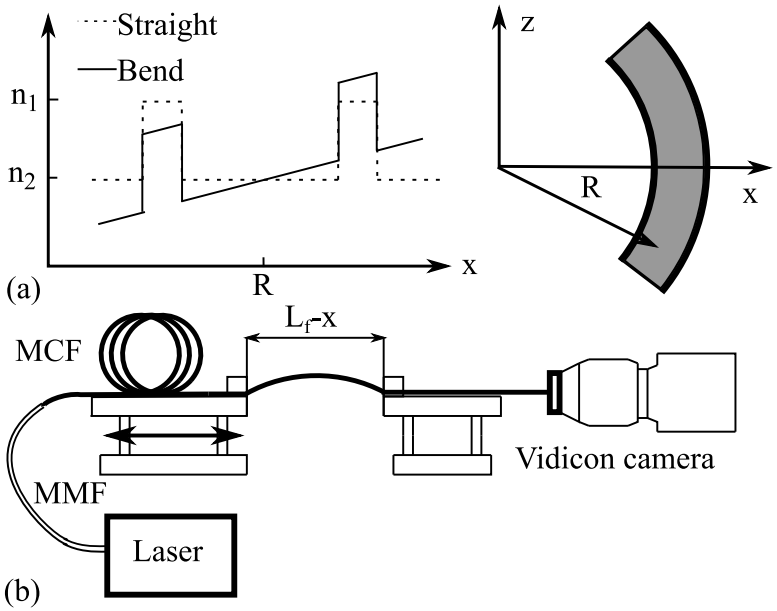

Figure 67: Transformation of bending action into a tilt refractive index (a). Setup diagram for bending measurement: Laser injects light into MMF with 100µm core radius fused to the MCF which is fixed to a movable stage and a fixed stage and the connected to Vidicon camera (b).

the central MCF experiences a buckling that can be approximated to a circular arc thus, the curvature approximates to Eq. 88 employed in section 5.2.2.2.

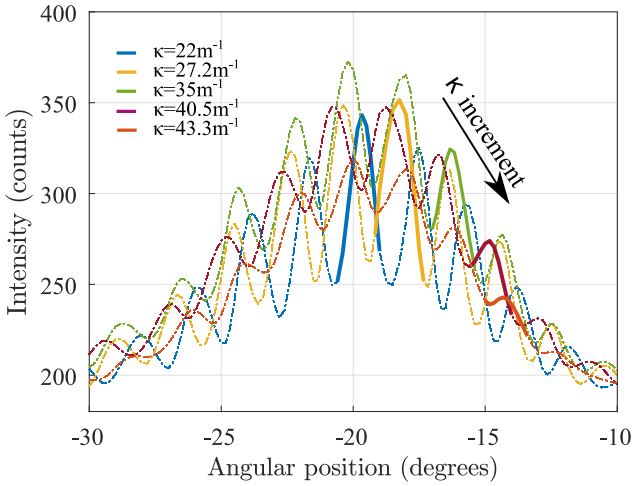

Figure 68: Interference pattern of first diffraction order of Fig. 60.d under bending action. Bending action shifts the fringe pattern as can be appreciated of bold fringe.

Under this simplification, curvature has been varied between 0 and $40m^{-1}$ in two perpendicular directions (U and V) causing a fringe shift in measured FFP as depicted in Fig. 68 where first diffraction order fringe pattern experiences a fringe shift higher than the fringe period. This shift has been measured for the two perpendicular firsts orders (X and Y) and the zero order in its corresponding direction. Fig. 69 exhibits the fringe shift versus curvature for both perpendicular bends and both axis. First, the fringe shift exhibits an

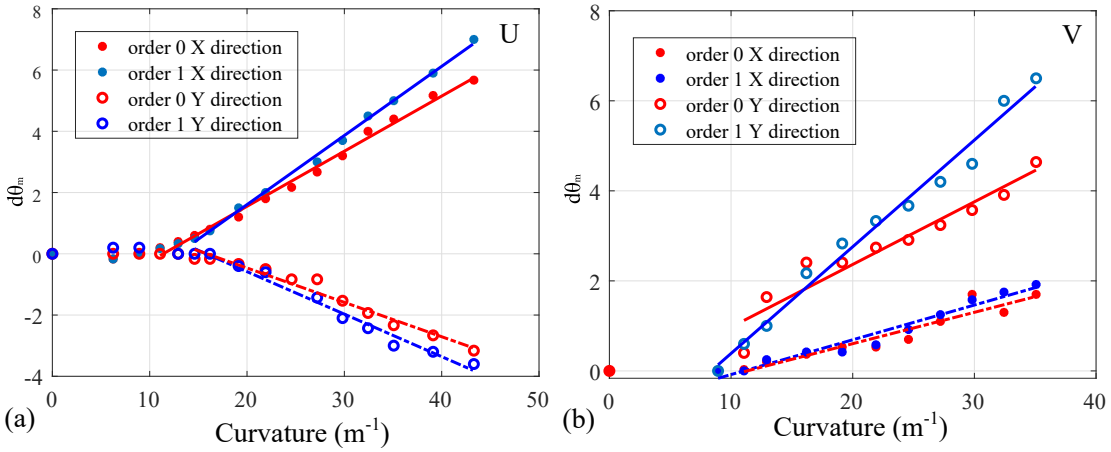

Figure 69: Results of bending action into fringe shift for bending in U direction (a) and V direction (b) for diffraction orders at X and Y direction. Sensitivity of order 0 (no inscription) is lower for all cases.

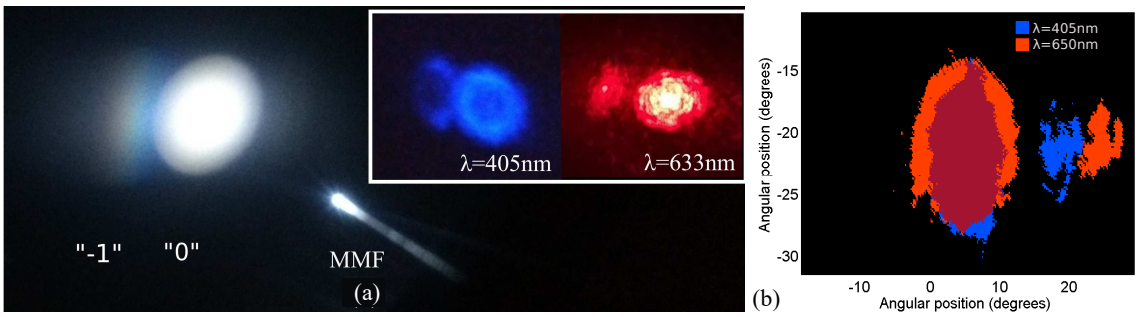

Figure 70: Illumination of same diffraction grating by a white, red and blue light source (a). The FFP of $\lambda_r = 650nm$ and $\lambda_b = 405nm$ overlapped (b).

approximately linear behavior for curvatures higher than $10m^{-1}$. In this linear regime, the two perpendicular bend exhibit opposed slopes of X and Y orders, reconstructing two perpendicular bending vectors.

Core slope is in all cases lower than first order slope; this is caused by the dependence of fringe shift with the period as exhibited in Eq. 95. Sensitivities of U bend for X order are $0.2257 degrees/m^{-1}$ and $0.1911 degrees/m^{-1}$ for the first order and core respectively, where their quotient with their respective theoretical periods gives respectively 0.1107° and 0.1105° showing a remarkable agreement with theory. This also demonstrates a slight sensitivity enhancement with the inscription of the diffraction grating.

6.4.5 DE-MULTIPLEXING

Other practical applications are light decoupling and wavelength demultiplexing. A proof of concept of this later is depicted in Fig. 70.a. First-order chromatic dispersion allows good spatial separation when illuminated by the white light source. This separation is also represented by the plotted red and blue patterns attached to the figure which provides complementary information to Fig. 55.b to describe behavior with wavelength. In

addition, overlapped FFPs of these two wavelengths are depicted in Fig. 63.b showing good spatial resolution.

6.5 CONCLUDING REMARKS

In this chapter, the potential of fs laser processing at the fiber end-face has been shown with one of the simplest patterns that could be inscribed, a diffraction grating. Through the different sections, diffraction gratings have been inscribed in different types of fiber such as SMF or MMF where the later has shown higher diffraction efficiency. The study focused not only at the end-face surface but also below it. The diffraction gratings with the best mechanical resistance were the ones written in POFs followed by the ones written below fiber end-face surface. It has also been shown that more complex fibers such as the MCFs fibers can enhance its intrinsic properties by these simple inscriptions, leading to complex and useful OFSs. The applications of these patterns are varied and through section 6.4, a proof of concept of a good selection os sensing parameters have been performed.

Despite all the work performed, there is still a lot of studies and patterns that can be carried out. For example, diffraction efficiency has not been studied quantitatively, this is in part caused by the lack of a setup for measuring absolute efficiency reliably. Post processing is another improvement that should be studied, chemical etching, for example, could improve the efficiency of the gratings, increasing the sensing response at the same time. There are also several patterns that should be studied, optical vortex, for example, could be inscribed at the fiber en-face which are handy for spatial mode division multiplexing or high-dimensional encoding [181]. Overall, fs laser processing at fiber end-face exhibits a high potential that has not been fully developed yet. However, it also exhibits some limitations like the width of the focal volume that other more expensive techniques such as FIB can overcome. This requires some trade-off decisions when complex patterns such as holograms are being inscribed.

Part III

CONCLUSIONS AND FUTURE LINES

7

SUMMARY AND CONCLUSIONS

In the course of this PhD, attention has been brought toward fs laser processing of optical fibers. The choice of this kind of laser among other processing techniques stems from his excellent trade-off among flexibility, behavior, and cost. The revision of their current state of the art has identified some open challenges. To face them, several main goals were set:

1. **To establish and study characterization and simulation tools.** Characterization is an important step in every processing technique, allowing the quantification of the properties. Simulations are useful for preliminary studies, determining the viability of a certain design or even corroborating some theoretical approaches.

2. **To explore different setups for Type I & Type II inscription.** Effort were focused on the study of various writing configurations to compare their different inscription. Different setups were studied, and their result characterized.

3. **To conceive and design new structures for sensors.** New configurations of optical waveguides or gratings were employed in the manufacture of new sensors.

4. **To explore the potential of the end-face inscription.** Inscriptions at the end-face were thoroughly studied in several scenarios, such as surface and bellow surface inscription. These measurements were also performed through different types of optical fibers.

5. **To apply the inscription at the fiber end-face to design new types of sensors .** The FFP of the end fiber inscription was employed as a transducer. Thus, the fiber end-face or even the entire fiber must be turned into a multiparameter sensor.

In this dissertation, knowledge and techniques considered relevant to face the identified challenges have been included in the preliminary part. Then the results obtained are addressed and summarized in the contributions part for a later discussion and conclusion in this part. Finally, published results both consequence of the works of this thesis and from others in this document are listed in the references part

The properties of fs laser irradiation in fused silica (and other materials) have been verified and employed to design new optical sensors, thus, contributing to the state of art of both fs laser processing and OFSs. These new designs have been possible due to the implementation of several techniques that allowed both characterization of the inscription results and the simulation of the designed structures with the parameters extracted from characterization steps. The techniques reviewed in the course of this work are listed below:

FDTD. This simulation method computes both **E(r,t)** and **H(r,t)** in the entire studied spatial and temporal domain. It is very robust but also requires a huge amount of computational resources. It is adequate for complex structures in a small domain.

BPM. This simulation method computes Helmholtz equation propagating along z direction, it offers reliable results for large but simple structures with low index change and one propagation direction.

RNF PROFILOMETRY. A reliable technique to obtain RI profiles of optical fibers. It can also measure the inscribed waveguides in the optical fiber if cleaved appropriately.

QPM. A image processing technique that turns focused and defocused intensity images into one single phase image.

DE SÉNERMONT COMPENSATOR. A microscope technique that allows retardation measurement (proportional to birefringence)

MICRO RAMAN SPECTROSCOPY. This spectroscopic technique allows the structural study of the matter taking advantage of Raman scattering. Structural changes can indicate several effects such as expansion or stress relieving.

PBP. This is a simple technique to manufacture FBGs through PRR modulation.

These tools have been applied in actual processing situations and showed their relevant contribution. Both QPm and RNF have been used for profiling the RI of the optical fiber showing good agreement. A reliable measurement of the index profile of optical fibers is crucial for the simulation of mode propagation through the optical fiber and. The application of QPm was also extended to fs laser inscriptions. The BAN family and NdY:SrF2 were irradiated, and their phase change and retardance (with de Sénarmont Compensator) were measured. This information provided important hints for posterior waveguide inscription; besides, these parameters are basic for posterior sensor design and simulation. Micro Raman spectroscopy was employed for the study of FBG regeneration in multilayer fibers. This technique revealed several expansion indicators that suggested a change in thermal history as a consequence of the annealing process. Finally, the BPM method was employed in the study of optical loss in a POF refractometer, simulation and experimental results were in good agreement, demonstrating the relevance and utility of this simulation method.

Once the simulation and characterization tools were employed in a context where its usefulness was demonstrated. The rest of the dissertation was mainly driven in two approaches of fs processing optical fibers. The first approach comprehended the in fiber transversal inscription while the second covered the processing of the fiber end-face.

In the in fiber inscription, the effort was focused on two different types of inscriptions. The first one exploited the cylindrical geometry of the fiber to act as a cylindrical lens, comprising focal volume in one axis and producing a loose of focus. This writing method produced a negative LIRIC at focal volume and filamentation above moderate pulse energies. The filament exhibited a high positive RIC at moderate energies. This zone was employed to inscribe waveguides in the fiber which allowed the manufacturing of a new type of MZI based on waveguides. This sensor was temperature and curvature characterized, his degradation at high temperature allowed single-use sensing with high sensitivity. The MZI also exhibited a linear sensitivity (up to $9.49 nm/m^{-1}$) in a remarkable broad region

(0 to $14m^{-1}$) dependent on bending axis. New configurations of this MZI can enhance his properties, inscription in a Tapered Optical Fiber enhanced its sensitivity with RIC as simulations suggested.

The second writing method simply consisted of the immersion of the optical fiber in index matching liquid and sandwiching between a microscope slide and a coverslip. This setup removes the loose of focus and the cylindrical lens effect. The characterization proved a positive RIC at low energies that can be used for grating inscription. The gratings were inscribed employing the PbP technique where the second harmonic was used to inscribe FBGs with 14.8dB reflection gain. RFGs were also inscribed in a TOF exhibiting a quasi-random distribution that was used in a single cavity laser setup, exhibiting two modes (1562nm and 1564.5nm) with 10dBm output power.

With both contributions at MZI and RFG the dissertation changed its focus to the processing of the fiber end-face. This type of inscription which is not so extensively studied as their in fiber counterpart. The inscription of diffraction gratings at fiber end-face was studied, characterizing its behavior at surface, below surface in SMF, MMF and POF. The study extended to bidimensional structures, where PbP and circular diffraction gratings exhibited remarkable results (this later was employed in a MCF). These inscriptions allowed the design of both intrinsic and extrinsic sensor based on these patterns. Extrinsic measurements such as tilt and displacements exhibited linear behavior and interesting sensitivity to power fluctuations. Particularly, tilt sensor exhibited insensitivity to displacement in around 10mm length (the camera position and configuration determine this range). Temperature and bending were the intrinsic measurements that also showed linear sensitivity. The later is measured through a MCF that produces an interferometric FFP with a sensitivity enhanced by the circular diffraction grating.

The study and contributions performed in this PhD offer a solid basis to improve the current state of the art of fs laser inscription in optical fibers and its application to OFS.

The main conclusions extracted from the work of this thesis are:

1. Depressed cladding waveguides can be inscribed in $NdY : SrF_2$.

2. rFBGs can be regarded as an imprinted spatial modulation of the glass fictive temperature $T_f(z)$.

3. The polishing of the transition region in a bent POF produces a loss reduction without altering RI sensitivity (for diameters higher than 1mm). These structures exhibit a solid performance as refractometers.

4. Direct exposition can be employed to manufacture waveguides within optical fibers exploiting the filament region.

5. Waveguides mentioned above can be used for manufacturing a MZI that is sensible to curvature and high temperature. Its length is lower than conventional MZIs employed for vectorial bending sensing.

6. Proposed adaptive optics setup can be employed to inscribe gratings with the PbP technique.

7. A quasi RFG inscribed in a TOF can be used as a selective mirror in a single cavity laser system, exhibiting output powers of 10dBm.

8. Diffraction gratings can be inscribed bellow fiber end-face surface. This structure can be tilted to control the position of order angles.

9. Tilted diffraction gratings can also be inscribed at POF end-face surface.

10. Diffraction gratings inscribed at MCF end-face surface can filter and enhance interference effect produced by different cores.

11. Structures achieved in conclusions 8-10 can be employed for different kinds of sensors, such as displacement, tilt, temperature, and bending.

8

OPEN FUTURE LINES

The primary goal of this PhD has been the characterization of fs laser processing of optical fibers to manufacture OFS. Despite the remarkable effort expected into two fiber processing zones and inscription methods, there is still a lot of room for future lines. The potential of fs laser processing is tremendous, and new advances increase the number of possible applications. This summary will briefly highlight several open works that should be performed.

8.1 SETUP IMPROVEMENTS

The employed writing setup in this PhD employs only the basic features of inscription stages. This is particularly representative of the available results of fs writing without the need for high PRR, multiple NAs, pulse shaping or polarization control. In future works, a setup upgrade could allow better control of the inscription. Some suggested improvements are:

- A better illumination (Koehler Illumination) would improve the sharpness of the QPm acquired images, allowing a more precise characterization of the irradiated area.
- Polarization control can change the properties of the inscribed structures. The orientation of the porous nanolayers changes depending on the polarization direction.
- Improvements on the Pulse Repetition Rate and/or acceleration control could lead to grating inscription with higher degree of randomness.
- The inscription at higher PRR is another interesting field of study. The results in $NdYSrF_2$ suggest a reduction in waveguide loss when employing high PRR, the same approach should be performed in optical fiber for structure inscription.

8.2 FUTURE LINES WITH THE IN FIBER INSCRIPTION

This section addressed the direct continuation of the work performed in chapter 5. Here, type II waveguides were employed in the design of a MZI. This scheme has been used in other works with different NA [182] or employing a hollow core fiber [183]. The employ of this proposed design by other research centers highlight its versatility and potential. Various modifications and characterizations should be performed. For example, adaptive optics could be employed instead the type II waveguides and the sensor could be characterized for strain and torsion. FBG inscription on the sensing arm is another enhancement of the initial design. The FBGs can also be inscribed in other types of fibers such as MMFs

or MCFs. The inscription of waveguides and FBGs in MCFs is of special interest given its curvature sensing potential.

The employed PbP was employed for type I fs FBG inscription. There is an increasing demand for high-temperature resistant FBGs and fs exhibit superior advantages compared to the UV counterpart. In future works, temperature characterization and annealing of this FBGs should be performed to surpass the current limit of total erasure at 1000°C. New regeneration techniques should be studied.

8.3 FUTURE LINES IN THE FIBER END-FACE INSCRIPTION

The main goal of the chapter 6 was the inscription of the diffraction grating in several ways and in seral fibers. The characterization process is far from being completed. This chapter lacks several quantitative values that would help to understand better the behavior of diffraction gratings in optical fibers. Besides, more complex diffractive elements should be studied such as optical vortex, Fresnel lens or binary Airy masks for both new optical devices and intrinsic transduction schemes.

Enhanced properties of structures and devices could be reached by the combination of fs laser inscription with optimized annealing and wet etching post processes.

Part IV

REFERENCES

PUBLICATIONS

CLOSE RELATED TO THE PHD WORK

INTERNATIONAL JOURNALS

1. D. Pallarés-Aldeiturriaga, L. Rodríguez-Cobo, A. Quintela and J. M. López-Higuera, "*Curvature Sensor Based on In-Fiber Mach–Zehnder Interferometer Inscribed With Femtosecond Laser*," in *Journal of Lightwave Technology*, vol. 35, no. 21, pp. 4624-4628, 1 Nov.1, 2017. doi: 10.1109/JLT.2017.2756103

2. D. Pallares-Aldeiturriaga, L. Rodriguez-Cobo, M. Lomer and J. Lopez-Higuera, "*Diffractive elements inscribed at end-fiber surface by femtosecond laser*," in *Journal of Lightwave Technology*. doi: 10.1109/JLT.2019.2909145

3. B. Hari Babu, Chengkun Lyu, Thomas Billotte, D. Pallares-Aldeiturriaga, Bertrand Poumellec, J. M. Lopez-Higuera, Xiao-Tao Hao, and Matthieu Lancry, "*Stress-induced optical waveguides written by an ultrafast laser in Nd3+, Y3+ co-doped SrF2 crystals*," *Appl. Opt.* 58, 984-990 (2019)

4. R. A. Perez-Herrera, D. Pallarés-Aldeiturriaga, A. Júdez, L. Rodriguez Cobo, M. Lopez-Amo and J.M. Lopez-Higuera , "*Optical fiber lasers assisted by micro-drilled optical fiber tapers*," accepted in *Optics Letters*.

INTERNATIONAL CONFERENCES

1. D. Pallarés-Aldeiturriaga, L. Rodriguez-Cobo, A. Quintela, J. M. Lopez-Higuera, "*In-fiber Mach-Zehnder interferometer inscribed with femtosecond laser for high temperature sensing*," Proc. SPIE 10323, *25th International Conference on Optical Fiber Sensors*, 103237B (23 April 2017);

2. M. Lancry, K. Cook, D. Pallarés-Aldeiturriaga, J. M. Lopez-Higuera, B. Poumellec, and J. Canning, "*Raman spectroscopic study of Bragg gratings regeneration*," in *Advanced Photonics 2018 (BGPP, IPR, NP, NOMA, Sensors, Networks, SPPCom, SOF)*, OSA Technical Digest (online) (Optical Society of America, 2018), paper BM2A.4.

3. D. Pallarés-Aldeiturriaga, L. Rodriguez-Cobo, M. Lancry, B. Poumellec, and J. M. Lopez-Higuera, "*Mach-Zehnder interferometer based on femtosecond laser waveguide inscription*," in *Advanced Photonics 2018 (BGPP, IPR, NP, NOMA, Sensors, Networks, SPPCom, SOF)*, OSA Technical Digest (online) (Optical Society of America, 2018), paper JTu2A.4.

4. D. Pallarés-Aldeiturriaga, L. Rodriguez-Cobo, I. Laarossi, and J. M. Lopez-Higuera, "*Displacement Insensitive 2D Tilt Sensor Based on End-Face Diffraction Grating Inscribed*

by Femtosecond Laser," in *26th International Conference on Optical Fiber Sensors*, OSA Technical Digest (Optical Society of America, 2018), paper TuE55.

5. D. Pallares-Aldeiturriaga, L. Rodriguez-Cobo, M. Lomer, and J. M. Lopez-Higuera, "*Tilted End-Fiber Diffraction Grating Inscribed by Femtosecond Laser for Temperature Measurement*," in *26th International Conference on Optical Fiber Sensors*, OSA Technical Digest (Optical Society of America, 2018), paper ThE53.
6. David Pallarés Alediturriaga; Mauro Lomer Barboza; Javier Mateo Gascón; Luis Rodríguez Cobo, "*Micromachining of diffraction grating in PMMA-POF for application in low cost sensors*", in *27th International Conference on Plastic Optical Fibers (POF 2018)*,International Cooperative of Plastic Optical Fiber (ICPOF)

NATIONAL CONFERENCES

1. David Pallarés Aldeiturriaga; Luis Rodríguez Cobo; Rubén Ruiz Lombera; Antonio Quintela Incera; J. M. Lopez-Higuera, *Femtosecond Laser inscription of diffractive element in optical fiber end-face*, in *Optoel 2017 (X Reunión Española de Optoelectrónica)*
2. David Pallarés Aldeiturriaga; Luis Rodríguez Cobo; Ismail Laarossi; José Miguel López Higuera, *Red de difracción inscrita a la salida de fibra óptica por láser de femtosegundo*, in *RNO 2018 (XII Reunión Nacional de Óptica))*,ISBN 978-84-09-03559-5
3. David Pallarés Aldeiturriaga; Luis Rodríguez Cobo; Mauro Lomer Barboza; José Miguel López Higuera, *Wavelength demultiplexor inscribed in optical fiber end-face by femtosecond laser*, in URSI 2018 (XXXIII Simposium Nacional de la Unión Científica Internacional de Radio)

OTHER CONTRIBUTIONS

NATIONAL CONFERENCES

1. Rubén Ruiz Lombera; Ismail Laarossi; Luis Rodriguez Cobo; David Pallarés Aldeiturriaga; Maria Angeles Quintera Incera; Jesús Mirapeix Serrano; José Miguel López Higuera, *Medidas distribuidas a alta temperatura empleando fibra multimodo con cubierta de oro y un sensor BOTDA*, in *Optoel 2017 (X Reunión Española de Optoelectrónica)*
2. Laarosi, I., María Ángeles Quintera Incera, D. Pallarés Aldeiturriaga, J.M López-Higuera (2018 Julio). *Medidas de alta temperatura mediante el sistema RDTS y fibra recubierta con carbono y polimida*. En *XII Reunión Nacional de Óptica*, Universitat Jaume I de Castellón

SUBMITTED CONTRIBUTIONS

INTERNATIONAL JOURNALS

1. D. Pallarés-Aldeiturriaga, L. Rodríguez-Cobo, M. Lomer and J. M. López-Higuera, "*Characterization of tilted End-Fiber Diffraction Grating Inscribed by Femtosecond Laser*," submitted to *Optics & Laser Technology*.

2. M. Lomer, D. Pallarés-Aldeiturriaga, L. Rodríguez-Cobo, J. Arrue and J. M. López-Higuera, "*Fiber optic refractometer for liquids*," submitted to *Sensor & Actuators: A. Physical*

INTERNATIONAL CONFERENCES

1. P. Roldán-Varona, D. Pallarés-Aldeiturriaga, L. Rodríguez-Cobo and J. M. López-Higuera, "*Refected power-based 2D bending sensor using femtosecond laser FBG inscription in multicore fiber*," submitted to *7th European Workshop on Optical Fibre Sensors (EWOFS19)*.

BIBLIOGRAPHY

[1] J Pozo and M Van Den Dobbelsteen. Funding your Photonic Research via Horizon 2020. In *2014 16th International Conference on Transparent Optical Networks (ICTON)*, pages 1–2. IEEE, 2014. (Cited in page 23.)

[2] J.M. Lopez-Higuera, editor. *Handbook of Optical Fibre Sensing Technology*. 2002. (Cited in pages 23 and 50.)

[3] José Miguel López-Higuera, Luis Rodríguez-Cobo, and Adolfo Cobo. Optical Sensors: a comprehensive approach. *Advanced Photonics 2015*, page SeS2B.1, 2015. (Cited in page 23.)

[4] Stephen L. Trokel, R. Srinivasan, and B. A. Bodil Braren. Excimer laser surgery of the cornea. *American Journalof Ophtalmology*, pages 710–715, 1983. (Cited in pages 23 and 33.)

[5] Uri Lindner, Nathan Lawrentschuk, and John Trachtenberg. Focal Laser Ablation for Localized Prostate Cancer. *Journal of Endourology*, 24(5):791–797, 2010. (Cited in page 23.)

[6] Ronald R. Krueger, Yaron S. Rabinowitz, and Perry S. Binder. The 25th Anniversary of Excimer Lasers in Refractive Surgery: Historical Review. *Journal of Refractive Surgery*, 26(10):749–760, 2010. (Cited in page 23.)

[7] Seung Min Yoo and Sang Yup Lee. Optical Biosensors for the Detection of Pathogenic Microorganisms. *Trends in Biotechnology*, 34(1):7–25, 2016. (Cited in page 23.)

[8] David J. Cuccia, Frederic Bevilacqua, Anthony J. Durkin, and Bruce J. Tromberg. Modulated imaging: quantitative analysis and tomography of turbid media in the spatial-frequency domain. *Optics Letters*, 30(11):1354, 2005. (Cited in pages 23 and 119.)

[9] A Ashkin and Life Fellow. Small-Neutral Particle , Atoms , and Molecules. *IEEE Journal of Selected Topics in Quantum Electronics*, 6(6):841–856, 2000. (Cited in page 23.)

[10] John C. Ion. *Laser Processing of Engineering Materials*. Elsevier, 2005. (Cited in page 23.)

[11] Ewen Smith and Geoffrey Dent. *Modern Raman Spectroscopy – A Practical Approach*. Willey, 1 edition, 2005. (Cited in pages 23 and 75.)

[12] P. Hariharan. *Optical Interferometry*. Elsevier, San DIego, 2 edition, 2003. (Cited in page 23.)

[13] John M Senior. *Optical Fiber Communications Principles andPractice*. Pearson Education Limited, 3 edition, 2009. (Cited in pages 23, 34, 53, and 79.)

[14] Feng Pan, Xia Xiao, Yan Xu, and Shiyan Ren. An optical AC voltage sensor based on the transverse Pockels effect. *Sensors*, 11(7):6593–6602, 2011. (Cited in page 23.)

[15] Merritt N. Deeter. Fiber-optic Faraday-effect magnetic-field sensor based on flux concentrators. *Applied Optics*, 35(1):154, 2008. (Cited in page 23.)

[16] Gennady Kaloshin and Igor Lukin. An acousto-optical sensor with high angular resolution. *Sensors*, 12(3):3739–3746, 2012. (Cited in page 23.)

[17] E. Snitzer. Proposed fiber cavities for optical masers. *Journal of Applied Physics*, 32(1):36–39, 1961. (Cited in pages 23 and 48.)

[18] R Osellame, G. Cerullo, and R. Ramponi, editors. *Femtosecond Laser Micromachining; Photonics and Microfluidic Devices in Transparent Materials*, volume 6. Springer, 1980. (Cited in pages 24 and 27.)

[19] Yi Liu, Min Li, Huihui Sun, Yan Li, and Shiliang Qu. Ultrasensitive liquid refractometer based on a Mach-Zehnder micro-cavity in optical fibre fabricated by femtosecond laser-induced water breakdown. *Journal of Modern Optics*, 63(21):2285–2290, 2016. (Cited in page 24.)

[20] Anna K. Dębowska, Marcin Koba, Monika Janik, Wojtek J. Bock, and Mateusz Śmietana. Increased sensitivity of femtosecond laser micro-machined in-fiber Mach-Zehnder interferometer for small-scale refractive index sensing. 9916:99160Q, 2016. (Cited in pages 24 and 56.)

[21] Mohd Kamuri, Zurina Zainal Abidin, Mohd Yaacob, Mohd Hamidon, Nurul Md Yunus, and Suryani Kamarudin. Separation and Detection of Escherichia coli and Saccharomyces cerevisiae Using a Microfluidic Device Integrated with an Optical Fibre. *Biosensors*, 9(1):40, 2019. (Cited in page 24.)

[22] Christian Waltermann, Alexander Doering, Michael Köhring, Martin Angelmahr, and Wolfgang Schade. Cladding waveguide gratings in standard single-mode fiber for 3D shape sensing. *Optics Letters*, 40(13):3109, 2015. (Cited in page 24.)

[23] Debra D. Wawro, Sorin Tibuleac, Robert Magnusson, and Hanli Liu. Optical fiber endface biosensor based on resonances in dielectric waveguide gratings. 3911:86–94, 2000. (Cited in pages 24 and 58.)

[24] Wit Grzesik. *Advanced Machining Processes of Metallic Materials*. Elsevier, 2 edition, 2016. (Cited in page 27.)

[25] Arthur L. Schawlow and Chrales H. Townes. MASERS and MASER Communication System, 1958. (Cited in page 33.)

[26] Jhon. C Ion. *Laser Processing of Engineering Materials*. 2005. (Cited in page 33.)

[27] David Lichtman and Jhon F. Ready. Laser Beam Induced Electron Emission. *Physical Review Letters*, 10(8):342–345, 1963. (Cited in page 33.)

[28] P. A. Hilton. The Early Days of Laser Cutting. In *11th Nordic Conference in Laser Processing of Materials*, volume 3097, pages 10–16, 2007. (Cited in page 33.)

[29] Daniel S Gnanamuthu. Cladding, 1974. (Cited in page 33.)

[30] J Ihlemann, B Wolff, and P Simon. Nanosecond and Femtosecond Excimer Laser Ablation of Fused Silica *. *Applied Physics A: Materials Science and Processing*, 368:363–368, 1992. (Cited in page 33.)

[31] S. Küper and M Stuke. Femtosecond uv Excimer Laser Ablation. *Applied Physics B: Lasers and Optics*, 204:199–204, 1987. (Cited in page 33.)

[32] D Du, X Liu, G Korn, J Squier, G Mourou, D Du, X Liu, G Korn, J Squier, and G Mourou. Laserinduced breakdown by impact ionization in SiO2 with pulse widths from 7 ns to 150 fs Laser-induced from 7 ns to 150 fs by impact ionization in Sio2 with pulse widths. *Applied physics letters*, 64(3071):3071–3073, 1994. (Cited in page 33.)

[33] Tamara Delgado, Daniel Nieto, and María Teresa Flores-Arias. Soda-lime glass microlens arrays fabricated by laser: Comparison between a nanosecond and a femtosecond IR pulsed laser. *Optics and Lasers in Engineering*, 86:29–37, 2016. (Cited in page 34.)

[34] Yun-jiang Rao, Ming Deng, De-wen Duan, Xiao-chen Yang, Tao Zhu, and Guanghua Cheng. Micro Fabry-Perot interferometers in silica fibers machined by femtosecond laser. *Optics Express*, 15(21):14123–14128, 2007. (Cited in pages 34 and 56.)

[35] Shane M. Eaton, Mi Li Ng, Roberto Osellame, and Peter R. Herman. High refractive index contrast in fused silica waveguides by tightly focused, high-repetition rate femtosecond laser. *Journal of Non-Crystalline Solids*, 357(11-13):2387–2391, 2011. (Cited in pages 34 and 45.)

[36] Jing Liu and D. N. Wang. In-fiber beam splitters for construction of in-line Michelson interferometers. *Optics Letters*, 43(17):4304, 2018. (Cited in pages 34 and 56.)

[37] Matthew Lancry, Elise Regnier, and Bertrand Poumellec. Fictive temperature measurements in silica- based optical fibers and its application to Rayleigh loss reduction. In *Optical Fiber, New Developments*, chapter 7, pages 125–160. 2009. (Cited in pages 34 and 40.)

[38] A. Samoilov, D. Berlin, P. Bernasconi, and C. Joyner. Increase optical bandwidth with Epi CVD. *Semiconductor International*, 25(13), 2002. (Cited in page 34.)

[39] Hugh O Pierson. *HANDBOOK OF CHEMICAL VAPOR DEPOSITION (CVD)*. Number Cvd. NOYES PUBLICATIONS, New York. (Cited in page 34.)

[40] A J Ikushima, T Fujiwara, and K Saito. Silica glass : A material for photonics Silica glass : A material for photonics. *Journal of Applied Physics*, 1201(2000), 2012. (Cited in page 34.)

[41] John Ballato, Heike Ebendorff-heidepriem, Jiangbo Zhao, and Laeticia Petit. Glass and Process Development for the Next Generation of Optical Fibers : A Review. *Fibers*, pages 1–26. (Cited in page 34.)

[42] Robert F Pierret. *Advanced Semiconductor Fundamentals*. Pearson Education, New Jersey, 2 edition, 1983. (Cited in page 34.)

[43] T Gietzelt and L Eichhorn. Mechanical Micromachining by Drilling , Milling and Slotting. In *Micromachining Techniques for Fabrication of Micro and Nano Structures*. 2012. (Cited in page 35.)

[44] S Mahendran and Ramasamy Devarajan. MICRO-EDM : OVERVIEW AND RECENT DEVELOPMENTS. In *1st NCMER 2010*, number March, 2016. (Cited in page 35.)

[45] Ricardo Melo André. *Focused ion beam milling of optical fiber microstructures for sensing applications*. PhD thesis, University of Porto, 2017. (Cited in page 35.)

[46] V. Lucarini, J.J. Saarinen, K.-E. Peiponen, and E.M. Vartiainen. *Kramers-Kronig Relations in Optical Materials Research*. 2005. (Cited in page 36.)

[47] B. Poumellec, P. Niay, M. Douay, and J. F. Bayon. The UV-induced refractive index grating in Ge:SiO2 preforms: Additional CW experiments and the macroscopic origin of the change in index. *Journal of Physics D: Applied Physics*, 29(7):1842–1856, 1996. (Cited in pages 37 and 38.)

[48] C. Z. Tan and J. Arndt. The mean polarizability and density of glasses. *Physica B*, 229:217–224, 1997. (Cited in page 37.)

[49] Florian Dürr. *Laser-Induced Stress Changes in Optical Fibers*. PhD thesis, 2005. (Cited in pages 37 and 45.)

[50] F. Kherbouche and B. Poumellec. UV-induced stress field during Bragg grating inscription in optical fibres. *Journal of Optics A: Pure and Applied Optics*, 3(6):429–439, 2001. (Cited in page 38.)

[51] M. Lancry, N. Groothoff, B. Poumellec, and J. Canning. Photo-induced densification in Er3+/Al doped silica preform plates using 193-nm laser light. *Applied Physics B: Lasers and Optics*, 94(4):589–597, 2009. (Cited in page 38.)

[52] N F Borrelli and R A Miller. Determination of the Individual Strain-Optic Coefficients of Glass by an Ultrasonic Technique. *Applied Optics*, 7(5):745–750, 1968. (Cited in page 38.)

[53] Axel Bertholds and Rene Dandliker. Detennination of the Individual Strain-Optic Coefficients in Single-Mode Optical Fibers. *Journal of Lightwave Technology*, 6(8717515):17–20, 2000. (Cited in page 38.)

[54] R. Bruckner. Properties and structure of vitreous silica. I. *Journal of Non-Crystalline Solids*, 5(2):123–175, 1970. (Cited in page 39.)

[55] Lena. Bressel, Dominique.. de Ligny, Camille Sonneville, Valérie. Martinez, Vygantas. Mizeikis, Ričardas. Buividas, and Saulius. Juodkazis. Femtosecond laser induced density changes in GeO2 and SiO2 glasses: fictive temperature effect [Invited]. *Optical Materials Express*, 1(4):605–613, 2011. (Cited in page 40.)

[56] G. Steinmeyer, D. H. Sutter, L. Gallmann, N. Matuschek, and U. Keller. Frontiers in Ultrashort Pulse Generation: Pushing the Limits in Linear and Nonlinear Optics. *Science*, 286(5444):1507–1512, 1999. (Cited in page 40.)

[57] J. Valdmanis and R Fork. Design Considerations for a Femtosecond Pulse Laser Balancing Self Phase Modulation, Group Velocity Dispersion, Saturable Absorption, and Saturable Gain. *JIEEE Journal of Quantum Electronics*, (I), 1986. (Cited in page 40.)

[58] P Balling and J Schou. Femtosecond-laser ablation dynamics of dielectrics : basics and applications for thin films. *Reports on Progress in Physics*, 2013. (Cited in page 41.)

[59] D E Spence, P N Kean, and W Sibbett. 60-fsec pulse generation from a self-mode-locked Ti : sapphire laser. *Optics Letters*, 16(1):42–44, 1991. (Cited in page 41.)

[60] Martin E. Fermann, Almantas Galvanauskas, and Gregg Sucha. *Ultrafast Lasers: Technology and Applications*. CRC Press, 2002. (Cited in page 41.)

[61] Raymond J. Lanzafame, Jean-Claude Diels Rudolph, and Wolfgang. *Ultrashort Laser Pulse Phenomena: Fundamentals, Techniques, and Applications on a Femtosecond Time Scale*, volume 25. 2 edition, 2007. (Cited in page 41.)

[62] Shian Zhou, Lyuba Kuznetsova, Andy Chong, and Frank W Wise. Compensation of nonlinear phase shifts with third-order dispersion in short-pulse fiber amplifiers. *Optics express*, 5335(13):245–252, 2005. (Cited in page 41.)

[63] Lyuba Kuznetsova and Frank W Wise. Scaling of femtosecond Yb-doped fiber amplifiers to tens of microjoule pulse energy via nonlinear chirped pulse amplification. *Optics Letters*, 32(18):2671–2673, 2007. (Cited in page 41.)

[64] Martin E Fermann and Ingmar Hartl. Ultrafast fibre lasers. *Nature Photonics*, 7(November), 2013. (Cited in page 41.)

[65] P. M. Paul, E. S. Toma, P. Breger, G. Mullot, F. Augé, Ph. Balcou, H. G. Muller, and P Agostini. Observation of a Train of Attosecond Pulses from High Harmonic Generation. 292(June):1689–1693, 2001. (Cited in page 41.)

[66] Thomas Gaumnitz, Arohi Jain, Yoann Pertot, Martin Huppert, Inga Jordan, Fernando Ardama-Lamas, and Hans Jakob Wörner. Streaking of 43-attosecond soft-X-ray pulses generated by a passively CEP-stable mid-infrared driver. *Optics express*, 25(22):27506–27518, 2017. (Cited in page 41.)

[67] Johan Mauritsson, Giulio Vampa, and Caterina Vozzi. Emerging attosecond technologies. *Journal of Optics*, 20(110201):4pp, 2018. (Cited in page 42.)

[68] Dezhi Tan, Kaniyarakkal N. Sharafudeen, Yuanzheng Yue, and Jianrong Qiu. Femtosecond laser induced phenomena in transparent solid materials: Fundamentals and applications. *Progress in Materials Science*, 76(September 2015):154–228, 2016. (Cited in page 42.)

[69] Robert R Thomson, Nicholas D Psaila, Henry T Bookey, Derryck T Reid, and Ajoy K Kar. Controlling the Cross-section of Ultrafast Laser Inscribed Optical Waveguides. In *Femtosecond Laser Micromachining*, volume 123, chapter 5. Springer, 2012. (Cited in pages 43, 65, and 92.)

[70] Chris B Schaffer and Eric Mazur. Laser-induced breakdown and damage in bulk transparent materials induced by tightly focused femtosecond laser pulses. *Measurement Science and Technology*, 12:1784–1794, 2001. (Cited in pages 43 and 45.)

[71] E. G. Gamaly and A. V. Rode. Physics of ultra-short laser interaction with matter: From phonon excitation to ultimate transformations. *Progress in Quantum Electronics*, 37(5):215–323, 2013. (Cited in page 44.)

[72] Katherine C. Phillips, Hemi H. Gandhi, Eric Mazur, and S. K. Sundaram. Ultrafast laser processing of materials: a review. *Advances in Optics and Photonics*, 7(4):684, 2015. (Cited in pages 44 and 47.)

[73] B Poumellec, M Lancry, and P G Kazansky. Modification thresholds in femtosecond laser processing of pure silica : review of dependencies on laser parameters [Invited]. 1(4):766–782, 2011. (Cited in pages 44, 45, 64, and 112.)

[74] Sergey Mitryukovskiy. *Coherent Secondary Radiation from Femtosecond Laser Filaments Coherent Secondary Radiation from Femtosecond Laser Filaments*. Physics [physics], Ecole Polytechnique, 2014. (Cited in page 45.)

[75] K. Mishchik, C. D'Amico, P. K. Velpula, C. Mauclair, A. Boukenter, Y. Ouerdane, and R. Stoian. Ultrafast laser induced electronic and structural modifications in bulk fused silica. *Journal of Applied Physics*, 114(13), 2013. (Cited in page 45.)

[76] Lionel Sudrie. *LASER FEMTOSECONDES DANS LA SILICE*. Optique [physics.optics], Université Paris XI Orsay, 2002. (Cited in page 46.)

[77] John Canning, Matthieu Lancry, Kevin Cook, and Bertrand Poumellec. New theory of femtosecond induced changes and nanopore formation. 8351:1–7, 2011. (Cited in pages 46 and 50.)

[78] L Sudrie, M Franco, B Prade, and A Mysyrowicz. Writing of permanent birefringent microlayers in bulk fused silica with femtosecond laser pulses. *Optics Communications*, (December):279–284, 1999. (Cited in page 45.)

[79] Erica Bricchi, Peter G Kazansky, Erica Bricchi, and Peter G Kazansky. Extraordinary stability of anisotropic femtosecond direct-written structures embedded in silica glass Extraordinary stability of anisotropic femtosecond direct-written structures embedded in silica glass. *Applied physics letters*, 111119(2006):0–3, 2013. (Cited in page 45.)

[80] Matthieu Lancry, Bertrand Poumellec, John Canning, Kevin Cook, Jean-claude Poulin, and Francois Brisset. Ultrafast nanoporous silica formation driven by femtosecond laser irradiation. *Laser and Photonics Reviews*, 962(6):953–962, 2013. (Cited in pages 46 and 50.)

[81] Martynas Beresna, Mindaugas Gecevičius, Peter G Kazansky, Thomas Taylor, Alexey V Kavokin, Martynas Beresna, and Mindaugas Gecevic. Exciton mediated self-organization in glass driven by ultrashort light pulses Exciton mediated self-organization in glass driven by ultrashort light pulses. *Applied physics letters*, 053120(2012), 2012. (Cited in page 46.)

[82] V R Bhardwaj, E Simova, P P Rajeev, C Hnatovsky, R S Taylor, D M Rayner, and P B Corkum. Optically Produced Arrays of Planar Nanostructures inside Fused Silica. *Physical Review Letters*, 057404(February):1–4, 2006. (Cited in page 46.)

[83] S. Juodkazis, K. Nishimura, S. Tanaka, H. Misawa, E. G. Gamaly, B. Luther-Davies, L. Hallo, P. Nicolai, and V. T. Tikhonchuk. Laser-induced microexplosion confined in the bulk of a sapphire cystal: Evidence of multimegabar pressures. *Physical Review Letters*, 96(16):1–4, 2006. (Cited in page 47.)

[84] Barada K Nayak, Vikram V Iyengar, and Mool C Gupta. Efficient light trapping in silicon solar cells by ultrafast-laser-induced self-assembled micro / nano structures. *PROGRESS IN PHOTOVOLTAICS: RESEARCH AND APPLICATIONS*, (January):631–639, 2011. (Cited in page 47.)

[85] T Q Jia. Formation of nanogratings on the surface of a ZnSe crystal irradiated by femtosecond laser pulses. *Physical Review B*, pages 1–4, 2005. (Cited in page 47.)

[86] Susanta Kumar Das, Kiran Dasari, and Arkadi Rosenfeld. Extended-area nanostructuring of TiO 2 with femtosecond laser pulses at 400 nm using a line focus. *Nanotechnology*, 2010. (Cited in page 47.)

[87] Michael A Sheehy, Brian R Tull, Cynthia M Friend, and Eric Mazur. Chalcogen doping of silicon via intense femtosecond-laser irradiation. *Materials Science and Engineering B*, 137:289–294, 2007. (Cited in page 47.)

[88] Brian R Tull. *Femtosecond laser ablation of silicon: Nanoparticles, doping and photovoltaics*. PhD thesis, Harvard University, 2007. (Cited in page 47.)

[89] B. Hari Babu, Mengsi Niu, Thomas BIllotte, Pengqing Bi, Fei Zheng, Bertrand Poumellec, Matthieu Lancry, and Xiao-Tao Hao. Femtosecond laser processing induced low loss waveguides in multicomponent glasses. *Optical Materials Express*, 7(10):23958–23964, 2017. (Cited in page 47.)

[90] Sven Passinger, Mohammad S M Saifullah, Carsten Reinhardt, Kavasseri R V Subramanian, Boris N Chichkov, and Mark E Welland. Direct 3D Patterning of TiO 2 Using Femtosecond Laser Pulses **. *Advanced Materials*, pages 1218–1221, 2007. (Cited in page 47.)

[91] S Eliezer, N Eliaz, E Grossman, D Fisher, I Gouzman, Z Henis, S Pecker, Y Horovitz, M Fraenkel, S Maman, and Y Lereah. Synthesis of nanoparticles with femtosecond laser pulses. *Physical Review B*, pages 1–6, 2004. (Cited in page 47.)

[92] X. I. Tong, D. S. Jiang, W. B. Hu, Z. M Liu, and M. Z. Luo. The comparison between CdS thin films grown on Si (111) substrate and quartz substrate by femtosecond pulsed laser deposition. *Applied Physics A: Materials Science and Processing*, 148:143–148, 2006. (Cited in page 47.)

[93] William H. Bragg, William, L. Bragg. The reflexion of x-rays by crystals. *Proceedings of the Royal Society of London*, 88(5):428–438, 1913. (Cited in page 48.)

[94] J. Thomas, C. Voigtländer, R. G. Becker, D. Richter, A. Tünnermann, and S. Nolte. Femtosecond pulse written fiber gratings: A new avenue to integrated fiber technology. *Laser and Photonics Reviews*, 6(6):709–723, 2012. (Cited in pages 50, 51, and 64.)

[95] Turan Erdogan. Fiber Grating Spectra. *Journal of Lightwave Technology*, 15(8):1277–1294, 1997. (Cited in page 50.)

[96] Kenneth O Hill and Gerald Meltz. Fiber Bragg Grating Technology Fundamentals and Overview. 15(8):1263–1276, 1997. (Cited in page 50.)

[97] Zhi-gang Zang and Yu-jun Zhang. Low-switching power (<45 mW) optical bistability based on optical nonlinearity of ytterbium-doped fiber with a fiber Bragg grating pair. (August 2014):37–41, 2011. (Cited in page 50.)

[98] Yun-jiang Rao. In-fibre Bragg grating sensors. 355, 1997. (Cited in page 50.)

[99] M Lancry, B Poumellec, M Beresna, and P G Kazansky. Dependence of the femtosecond laser refractive index change thresholds on the chemical composition of doped-silica glasses. *Optical Materials Express*, 1(4):1784–1794, 2011. (Cited in pages 50 and 51.)

[100] Stephen J Mihailov. Fiber Bragg Grating Sensors for Harsh Environments. *Sensors*, pages 1898–1918, 2012. (Cited in page 51.)

[101] Stephen J Mihailov, Dan Grobnic, Cyril Hnatovsky, Robert B Walker, Ping Lu, David Coulas, and Huimin Ding. Extreme Environment Sensing Using Femtosecond Laser-Inscribed Fiber Bragg Gratings. *Sensors*, (1), 2017. (Cited in page 51.)

[102] S. Mihailov K. Cook, C. Smelser, J. Canning, G. le Garff, M. Lancry. Regenerated Femtosecond Fibre Bragg Gratings. In *Proc.SPIE*, pages 8351 – 8351 – 6, 2012. (Cited in page 51.)

[103] Yuhua Li, Minwei Yang, D N Wang, J Lu, T Sun, and K T V Grattan. Fiber Bragg gratings with enhanced thermal stability by residual stress relaxation. 17(22):19785–19790, 2009. (Cited in page 51.)

[104] John Canning, Somnath Bandyopadhyay, Palas Biswas, Mattias Aslund, Michael Stevenson, and Kevin Cook. Regenerated Fibre Bragg Gratings. In *Frontiers in*

Guided Wave Optics and Optoelectronics, chapter 18. IntechOpen, 2010. (Cited in pages 51, 52, and 82.)

[105] John Canning, Michael Stevenson, Somnath Bandyopadhyay, and Kevin Cook. Extreme Silica Optical Fibre Gratings. *Sensors*, pages 6448–6452, 2008. (Cited in page 51.)

[106] Michael Fokine. Formation of thermally stable chemical composition gratings in optical fibers LOCALLY INCREASED DIFFUSION. 19(8):1759–1765, 2002. (Cited in page 52.)

[107] S Trpkovski, D J Kitcher, G W Baxter, and S F Collins. High-temperature-resistant chemical composition Bragg gratings in Er 3 + -doped optical fiber. 30(6):607–609, 2005. (Cited in page 52.)

[108] John Canning. Fiber Bragg grating sensor for high temperature application. *Opto-Electronics and Communications Conference*, pages 2006–2007, 2008. (Cited in page 52.)

[109] Bowei Zhang and Mojtaba Kahrizi. High-Temperature Resistance Fiber Bragg Grating. 7(4):586–591, 2007. (Cited in page 52.)

[110] Ricardo Feced and Michalis N Zervas. Effects of Random Phase and Amplitude Errors in Optical Fiber Bragg Gratings. *Journal of Lightwave Technology*, 18(1):90–101, 2000. (Cited in page 52.)

[111] Johannes Skaar and Ricardo Faced. Reconstruction of gratings from noisy reflection data. *Journal of the Optical Society of America A*, 19(11):2229–2237, 2002. (Cited in page 52.)

[112] Amir Rosenthal and Moshe Horowitz. Reconstruction of a fiber Bragg grating from noisy reflection data. 22(1):84–92, 2005. (Cited in page 52.)

[113] Stanislav Derevyanko. Design of a flat-top fiber Bragg filter via quasi-random modulation of the refractive index. *Optics Letters*, 33(20):2404–2406, 2008. (Cited in page 52.)

[114] H Ongwei Y In and A Denowo G Badebo. Top-hat random fiber Bragg grating. 40(15):3592–3594, 2015. (Cited in page 52.)

[115] Yanping Xu. *FIBER RANDOM GRATING AND ITS APPLICATIONS*. PhD thesis, University of Ottawa, 2017. (Cited in pages 52 and 53.)

[116] H.C. van de Hulst. *Light Scattering by small particles*. Dover Publications, New York, 1981. (Cited in page 53.)

[117] Liang Zhang, Yanping Xu, Ping Lu, Stephen Mihailov, Liang Chen, and Xiaoyi Bao. Multi-Wavelength Brillouin Random Fiber Laser via Distributed Feedback from a Random Fiber Grating. *Journal of Lightwave Technology*, 36(11):2122–2128, 2018. (Cited in page 53.)

[118] R S Shankland. Michelson's role in the development of relativity. *Applied Optics*, 12(10):2280–2287, 1973. (Cited in page 54.)

[119] B. P. Abbott et Al. Observation of Gravitational Waves from a Binary Black Hole Merger B. *Physical Review Letters*, 116(6):061102, 2016. (Cited in page 54.)

[120] Byeong Ha Lee, Young Ho Kim, Kwan Seob Park, Joo Beom Eom, Myoung Jin Kim, Byung Sup Rho, and Hae Young Choi. Interferometric fiber optic sensors. *Sensors*, 12(3):2467–2486, 2012. (Cited in pages 55, 56, and 57.)

[121] Catarina S. Monteiro, Marta S. Ferreira, Susana O. Silva, Jens Kobelke, Kay Schuster, Jörg Bierlich, and Orlando Frazão. Fiber Fabry-Perot interferometer for curvature sensing. *Photonic Sensors*, 6(4):339–344, 2016. (Cited in page 56.)

[122] Pengfei Li, Haitao Yan, and Haojie Zhang. Highly sensitive liquid level sensor based on an optical fiber Michelson interferometer with core-offset structure. *Optik*, 171(June):781–785, 2018. (Cited in page 56.)

[123] Youfu Geng, Xuejin Li, Xiaoling Tan, Yuanlong Deng, and Yongqin Yu. High-sensitivity Mach-Zehnder interferometric temperature fiber sensor based on a Waist-Enlarged fusion bitaper. *IEEE Sensors Journal*, 11(11):2891–2894, 2011. (Cited in page 56.)

[124] Lili Mao, Ping Lu, Zefeng Lao, and Deming Liu. In-fiber Mach-Zehnder interferometer based on multi-mode fiber and up-taper for curvature sensing. *Optik*, 125(18):5108–5111, 2014. (Cited in page 56.)

[125] Jui-Ming Hsu, Jian-Zhi Chen, and Wen-Hao Zheng. Highly Sensitive Temperature Fiber Sensor Based on Mach-Zehnder Interferometer. *Fiber and Integrated Optics*, 35(5-6):230–238, 2016. (Cited in page 56.)

[126] Jiangtao Zhou, Changrui Liao, Yiping Wang, Guolu Yin, Xiaoyong Zhong, Kaiming Yang, Bing Sun, Guanjun Wang, and Zhengyong Li. Simultaneous measurement of strain and temperature by employing fiber Mach-Zehnder interferometer. *Optics Express*, 22(2):1680, 2014. (Cited in page 56.)

[127] H. Gong, D. N. Wang, B. Xu, K. Ni, H. Liu, and C. L. Zhao. Optical fiber internal-mirror-based fiber in-line Mach-Zehnder interferometer. 9916:99161U, 2016. (Cited in pages 56 and 57.)

[128] Longjiang Zhao, Lan Jiang, Sumei Wang, Hai Xiao, Yongfeng Lu, and Hai Lung Tsai. A high-quality Mach-Zehnder interferometer fiber sensor by femtosecond laser one-step processing. *Sensors*, 11(1):54–61, 2011. (Cited in pages 56 and 57.)

[129] Christian Waltermann, Alexander Doering, Michael Köhring, Martin Angelmahr, and Wolfgang Schade. Cladding waveguide gratings in standard single-mode fiber for 3D shape sensing. *Optics Letters*, 40(13):3109, 2015. (Cited in page 57.)

[130] Chupao Lin, Changrui Liao, Jia Wang, Jun He, Ying Wang, Zhengyong Li, Tianhang Yang, Feng Zhu, Kaiming Yang, Zhe Zhang, and Yiping Wang. Fiber surface Bragg grating waveguide for refractive index measurements. *Optics Letters*, 42(9):1684, 2017. (Cited in page 57.)

[131] Pengfei Wang, Haiyan Zhao, Xianfan Wang, and Gerald Farrell. A Review of Multimode Interference in Tapered Optical Fibers and Related Applications. 2014. (Cited in page 57.)

[132] Timothy A Birks and Youwei W Li. The Shape of Fiber Tapers. *Journal of Lightwave Technology*, 10(4):432–438, 1992. (Cited in page 57.)

[133] T. Zhu, F. Y. Chen, S. H. Huang, and X. Y. Bao. An ultra-narrow linewidth fiber laser based on Rayleigh backscattering in a tapered optical fiber. *Laser Physics Letters*, 10(5), 2013. (Cited in page 57.)

[134] Binqing Wu, Chunliu Zhao, and Juan Kang. Formaldehyde sensor based on zeolite thin film-coated spherical end-face fiber. *ICOCN 2016 - 2016 15th International Conference on Optical Communications and Networks*, pages 15–17, 2017. (Cited in page 57.)

[135] Pengfei Wang, Ming Ding, Lin Bo, Chunying Guan, Yuliya Semenova, Qiang Wu, Gerald Farrell, and Gilberto Brambilla. Fiber-tip high-temperature sensor based on multimode interference. *Optics Letters*, 38(22):4617–4620, 2013. (Cited in page 57.)

[136] Michael R. Hutsel and Thomas K. Gaylord. Inexpensive, efficient optical fiber end-face mirror. *Optics Communications*, 285(17):3608–3611, 2012. (Cited in page 57.)

[137] Xiaobing Li, Minghong Yang, Jixiang Dai, Hongliang Liu, Dan Yin, and Lijie Dong. Optical fiber humidity sensor with PVDF thin film as sensitive element. 7853:78533T, 2010. (Cited in page 57.)

[138] M. Lomer, J. Zubía, J. Arrue, and J. M. López Higuera. Principle of functioning of a self-compensated fibre-optical displacement sensor based on diffraction-grating-ended POF. *Measurement Science and Technology*, 15(8):1474–1478, 2004. (Cited in pages 57, 58, 110, and 116.)

[139] A. Ioannou, M. Polis, A. Lacraz, A. Theodosiou, and K. Kalli. Beam-shaping via femtosecond laser-modified optical fibre end faces. *Proceedings of SPIE*, 9886:98860J, 2016. (Cited in page 58.)

[140] Douglas J Little, Martin Ams, Peter Dekker, Graham D Marshall, Judith M Dawes, and Michael J Withford. Femtosecond laser modification of fused silica : the effect of writing polarization on Si-O ring structure. *Optics Express*, 16(24):20029–20037, 2008. (Cited in page 64.)

[141] Shane M. Eaton, G. Cerullo, and Roberto Osellame. Fundamentals of Femtosecond Laser Modification of Bulk Dielectrics. In *Femtosecond Laser Micromachining*, chapter 1. Springer, 2012. (Cited in pages 65 and 92.)

[142] G Cerullo, R Osellame, S Taccheo, M Marangoni, D Polli, R Ramponi, P Laporta, and S De Silvestri. Femtosecond micromachining of symmetric waveguides at 1 . 5 um by astigmatic beam focusing. *Optics Letters*, 27(21):1938–1940, 2002. (Cited in page 65.)

[143] Martin Ams, G. D. Marshall, D. J. Spence, and M. J. Withford. Slit beam shaping method for femtosecond laser direct-write fabrication of symmetric waveguides in bulk glasses. *Optics Express*, 13(15):5676–5681, 2005. (Cited in page 65.)

[144] Kane S. Yee. Numerical Solution of Initial Boundary Value Problems Involving Maxwell's Equations in Isotropic Media. *IEEE Transactions on Antennas and Propagation*, 14(3):302–307, 1966. (Cited in page 68.)

[145] R Scarmozzino and R.M Orgood. Comparison of finite-difference and Fourier-transform solutions of the parabolic wave equation with emphasis on integrated-optics applications. *journal of optics*, 8(5):724–731, 1991. (Cited in page 69.)

[146] R. Scarmozzino, A. Gopinath, R. Pregla, and S. Helfert. Numerical techniques for modeling guided-wave photonic devices. *IEEE Journal on Selected Topics in Quantum Electronics*, 6(1):150–162, 2000. (Cited in page 69.)

[147] Jesús Hoyo, Rebeca Martinez Vazquez, Belén Sotillo, Toney Teddy Fernandez, Jan Siegel, Roberto Osellame, Javier Solis, Toney Teddy Fernandez, Jan Siegel, and Paloma Fern. Control of waveguide properties by tuning femtosecond laser induced compositional changes Control of waveguide properties by tuning femtosecond laser induced compositional changes. *Applied physics letters*, 131101:0–4, 2014. (Cited in page 70.)

[148] Douglas J Little, Martin Ams, Peter Dekker, Graham D Marshall, Michael J Withford, Douglas J Little, Martin Ams, Peter Dekker, Graham D Marshall, and Michael J Withford. Mechanism of femtosecond-laser induced refractive index change in phosphate glass under a low repetition-rate regime Mechanism of femtosecond-laser induced refractive index change in phosphate glass under a low repetition-rate regime. *Journal of Applied Physics*, 033110(2010):0–5, 2010. (Cited in page 70.)

[149] Douglas J Little, Martin Ams, Simon Gross, Peter Dekker, Christopher T Miese, Alex Fuerbach, and Michael J Withford. Structural changes in BK7 glass upon exposure to femtosecond laser pulses. *Jouernal of Raman Spectroscopy*, 2010(September 2010):715–718, 2010. (Cited in page 70.)

[150] M J Saunders. Optical fiber profiles using the refracted near-field technique: a comparison with other methods. *Applied Optics*, 20(9):1645–1651, 1981. (Cited in page 71.)

[151] C. J. Bellair, C. L. Curl, B. E. Allman, P. J. Harris, A. Roberts, L. M.D. Delbridge, and K. A. Nugent. Quantitative phase amplitude microscopy IV: Imaging thick specimens. *Journal of Microscopy*, 214(1):62–69, 2004. (Cited in page 72.)

[152] A. Barty, K. A. Nugent, D. Paganin, and A. Roberts. Quantitative optical phase microscopy. *Optics Letters*, 23(11):817, 1998. (Cited in page 72.)

[153] Kaiming Zhou, Fangcheng Shen, Guolu Yin, and Lin Zhang. Optical fiber micro-devices made with femtosecond laser. 2016:3–5, 2016. (Cited in pages 76 and 102.)

[154] A. Roberts, E. Ampem-Lassen, A. Barty, K. A. Nugent, G. W. Baxter, N. M. Dragomir, and S. T. Huntington. Refractive-index profiling of optical fibers with axial symmetry by use of quantitative phase microscopy. *Optics Letters*, 27(23):2061, 2002. (Cited in pages 76 and 102.)

[155] Peter Günter and Jean-Pierre Huignard. *Photorefractive Materials and Their Applications 2: Materials*. Springer, 2007. (Cited in page 77.)

[156] J Lamela F Jaque and L Roso D Jaque. Refractive index change mechanisms in femtosecond laser written ceramic Nd : YAG waveguides : micro-spectroscopy experiments and beam propagation calculations. *Applied Physics B: Lasers and Optics*, pages 85–96, 2009. (Cited in page 79.)

[157] A Benayas W F Silva, A Ródenas C Jacinto, J Vázquez De Aldana, Y Tan R R Thomsom, N D Psaila D T Reid, and G A Torchia A K Kar. Ultrafast laser writing of optical waveguides in ceramic Yb : YAG : a study of thermal and non-thermal regimes. pages 301–309, 2011. (Cited in pages 79 and 80.)

[158] Jonas Burghoff, Christian Grebing, Stefan Nolte, and Andreas Tünnermann. Efficient frequency doubling in femtosecond laser-written waveguides in lithium niobate. *Applied physics letters*, 89(8):081108, 2006. (Cited in page 79.)

[159] Amir H Nejadmalayeri and Peter R Herman. Rapid thermal annealing in high repetition rate ultrafast laser waveguide writing in lithium niobate. *Optics Express*, 15(17):2987–2989, 2007. (Cited in pages 79 and 80.)

[160] Yang Tan, Airan Rodenas, Feng Chen, Robert R Thomson, Ajoy K Kar, Daniel Jaque, and Qingming Lu. 70 % slope efficiency from an ultrafast laser- written Nd : GdVO 4 channel waveguide laser. *Optics Express*, 18(24):24994–24999, 2010. (Cited in page 79.)

[161] B Hari Babu and V. V Ravi Kanth Kumar. White light generation in Ce 3 þ – Tb 3 þ – Sm 3 þ codoped oxy fl uoroborate glasses. *Journal of Luminescence*, 154:334–338, 2014. (Cited in page 79.)

[162] Dapeng Jiang, Yao Yu Zhan, Qian Zhang, Fengkai Ma, Liangbi Su, Fei Tang, Xiaobo Qian, and Jun Xu. Nd,Y:CaF2 laser crystal: novel spectra properties and laser performances from controlled local structure. *Royal Society of Chemistry*, (38), 2015. (Cited in page 79.)

[163] Shengzhi Sun, Liangbi Su, Yufeng Yuan, and Zhenrong Sun. Femtosecond laser-inscribed waveguides in Nd 3 + : Y 3 + : SrF 2 crystals. *Chinese Optics Letters*, 11(11):8–11, 2013. (Cited in page 79.)

[164] Xiuli Zhao. Stress-induced birefringence control in optical planar waveguides. *Optics Letters*, 28(7):564–566, 2003. (Cited in page 80.)

[165] Alfredo Pasquarello and Roberto Car. Identification of Raman Defect Lines as Signatures of Ring Structures in Vitreous Silica. *Physical Review Letters*, 80(23):5145–5147, 1998. (Cited in page 81.)

[166] Manon Heili, Bertrand Poumellec, Ekaterina Burov, Cédric Gonnet, Charles Le Losq, Daniel R. Neuville, and Matthieu Lancry. The dependence of Raman defect bands in silica glasses on densification revisited. *Journal of Materials Science*, 51(3):1659–1666, 2016. (Cited in page 81.)

[167] Xavier Bidault, Stéphane Chaussedent, Wilfried Blanc, and Daniel R Neuville. Deformation of silica glass studied by molecular dynamics : Structural origin of the anisotropy and non-Newtonian behavior. *Journal of Non-Crystalline Solids*, 433:38–44, 2016. (Cited in page 81.)

[168] R.A. Gambling, W.A. and Matsumura, H and Sammut. Mode shift at bends in single-mode fibres. *Electronics Letters*, 13:695–697, 1977. (Cited in page 83.)

[169] W. A. Gambling, H. Matsumura, C. M. Ragdale, and R. A. Sammut. Measurement of radiation loss in curved single-mode fibres. *IEE Journal on Microwaves, Optics and Acoustics*, 2:134–140, 1978. (Cited in page 83.)

[170] A. H. Badar and T. S. M. Maclean. Transition and pure bending losses in multimode and single-mode bent optical fibres. *IEE Proceedings J - Optoelectronics*, 138:261–268, 1991. (Cited in page 83.)

[171] Christian Schulze, Adrian Lorenz, Daniel Flamm, Alexander Hartung, Siegmund Schröter, Hartmut Bartelt, and Michael Duparré. Mode resolved bend loss in few-mode optical fibers. *Optics Express*, 21(3):3170, 2013. (Cited in page 84.)

[172] D. Marcuse. Field deformation and loss caused by curvature of optical fibers Dietrich. *Journal of the Optical Society of America A*, 66(4):311–320, 1976. (Cited in pages 84 and 97.)

[173] R Desmarchelier, B Poumellec, F Brisset, S Mazerat, and M Lancry. In the Heart of Femtosecond Laser Induced Nanogratings : From Porous Nanoplanes to Form Birefringence. *World Journal of Nano Science and Engineering*, 5(December):115–125, 2015. (Cited in page 92.)

[174] Shanshan Zhang, Weigang Zhang, Shecheng Gao, Pengcheng Geng, and Xiaolin Xue. Fiber-optic bending vector sensor based on Mach–Zehnder interferometer exploiting lateral-offset and up-taper. *Optics Letters*, 37(21):4480, 2012. (Cited in pages 97 and 98.)

[175] T. Allsop, K. Kalli, K. Zhou, Y. Lai, G. Smith, M. Dubov, D. J. Webb, and I. Bennion. Long period gratings written into a photonic crystal fibre by a femtosecond laser as directional bend sensors. *Optics Communications*, 281(20):5092–5096, 2008. (Cited in page 97.)

[176] Bo Huang and Xuewen Shu. insensitive torsion sensor based on a line-by-line inscribed phase-shifted FBG. *Optics Express*, 24(16):17670–17679, 2016. (Cited in page 105.)

[177] Keiron Boyd, Simon Rees, Nikita Simakov, Jae M. O. Daniel, Robert Swain, Eric Mies, Alexander Hemming, W. Andrew Clarkson, and John Haub. High precision

9.6 um CO2 laser end-face processing of optical fibres. *Optics Express*, 23(11):15065, 2015. (Cited in page 112.)

[178] Luis Rodriguez-Cobo, Mauro Lomer, and Jose Miguel Lopez-Higuera. Fiber Specklegram-Multiplexed Sensor. *Journal of Lightwave Technology*, 33(12):2591–2597, 2015. (Cited in page 114.)

[179] Eugene Hecht. *OPTICS*. Addison Wesley Longman, Inc, 2002. (Cited in page 118.)

[180] M Aoxiang H Ou, K Aiming Y Ang, J H E Un, X X U Izhen, S J U Huai, K Uikui G Uo, and Y Iping W Ang. Two-dimensional vector bending sensor based on seven-core fiber Bragg gratings. *Optics Express*, 26(18):23770–23781, 2018. (Cited in page 126.)

[181] Siyuan Yu Yuanhui Wen, Ioannis Chremmos, Yujie Chen, Jiangbo Zhu, Yanfeng Zhang. A compact mode sorter for demultiplexing vortex light beams. 11048, 2019. (Cited in page 129.)

[182] W. W. Li, W. P. Chen, D. N. Wang, Z. K. Wang, and Ben Xu. Fiber inline Mach–Zehnder interferometer based on femtosecond laser inscribed waveguides. *Optics Letters*, 42(21):4438, 2017. (Cited in page 137.)

[183] Yunfang Zhang, Chupao Lin, Changrui Liao, Kaiming Yang, Zhengyong Li, and Yiping Wang. Femtosecond laser-inscribed fiber interface Mach–Zehnder interferometer for temperature-insensitive refractive index measurement. *Optics Letters*, 43(18):4421, 2018. (Cited in page 137.)